# POSTER SESSION

## BASIC PHYSICS: NUCLEAR DATA AND EXPERIMENTS
## &
## MATERIALS, FUELS AND TARGETS

**P. D'Hondt (SCK•CEN)**

# DESIGN AND CHARACTERISTICS OF THE n_TOF EXPERIMENT AT CERN

**D. Cano-Ott**
*On behalf of the n_TOF collaboration*
CIEMAT
Avda Complutense 22, Madrid Zip: 28040, Spain

## Abstract

The n_TOF is a 180 m long neutron time-of-flight facility being built at CERN [1]. The aim of the experiment is to measure with high accuracy neutron-induced reaction cross-sections in nuclei relevant to ADS and Transmutation, as well as to Astrophysics. The neutrons are produced by spallation in a massive lead target using the 20 GeV/c CERN-PS proton beam. It is foreseen that its operation will start by fall 2000. An overview of the design of installation will be reported, putting special emphasis on those aspects particular to the n_TOF: the excellent energy resolution and the high-energy spectrum of the neutrons.

Most of the samples relevant to ADS and transmutation are radioactive and available only in reduced amounts of high purity. This introduces some constraints to the beam optics that have to be considered. It will be shown how the design of the neutron beam line has been adapted to the sample dimensions, in order to preserve the features of the installation and at the same time allow clean experiments.

Another challenge in the n_TOF design is coming from its geometry. The beam line is located inside a closed tunnel, which has certainly a great impact in the reduction of the background. This becomes of particular importance in the attenuation of high-energy neutrons (up to several GeV), since they can traverse through large amounts of materials producing many secondary particles. It will be illustrated how the design of the collimation system and shielding elements along the beam line guarantees acceptable neutron and gamma backgrounds at the measuring station, providing in this way a clean environment for the detectors.

## 1. Introduction

Among the large number of topics relevant to the design of the n_TOF facility at CERN, a question of primary importance from the experimental point of view is the determination and definition of the characteristics of the installation. The time-of-flight (TOF) measurements require a geometrically well-defined neutron beam at the sample position and the absence of backgrounds. Moreover, the neutron beam has to be adapted to the size of the samples, which is limited by the available amounts of high purity materials, by the target construction procedure and also by their intrinsic radioactivity (in case of unstable isotopes). The neutron beam has to be compatible with the requirements coming from the various proposed experimental techniques. The experimental programme of the n_TOF project covers a wide range of measurements summarised as follows:

- (n,γ) cross-section measurements with $C_6D_6$ detectors (in a first phase) and with a total absorption 4π calorimeter (in the second phase).
- (n,f) cross-section measurements with **P**arallel **P**late **A**valanche **C**hambers (PPAC).
- (n,xn) cross-section measurements with Ge or Si detectors.

Even though many sources of background can be highly suppressed through the time-of-flight tagging, those background events having a time correlation similar to the neutrons may not be rejected and may severely distort the measurements. Such background sources can be classified in two categories: i) neutron reactions at the sample without the proper time-energy relation and ii) signals in the detectors (produced by photons, neutron recoils or other particles) not originating from the reaction under study. In the first case, the background can be highly reduced by designing the optical and shielding elements (beam tube, collimators and walls) of the neutron beam line. The second background species are also reduced in this way, but in addition the number of secondary reactions (of neutrons and charged particles) has to be minimised also at the experimental area and its vicinity. The n_TOF collaboration has dedicated a big effort to the studies needed for the definition of the neutron beam design. Such studies covered a large spectrum of issues that can be summarised as follows:

- Study of the neutronic properties of the spallation target. In particular, production rates, the energy, the time, the spatial and the angular distribution of the neutrons.
- Study and design of the beam optics, i.e. beam tube and collimators.
- Design of the necessary shielding elements, which guarantee clean experimental conditions.

It should be emphasised that all these investigations were made under the scope of providing optimal conditions to the measurements, according to the following directives:

- The neutron beam size should have a radius as small as 2 cm, given the availability of the samples, its intrinsic radioactivity, the overall detection efficiencies and the experimental requirements arising from the capture (both the $C_6D_6$ detectors and the 4π calorimeter), the fission and the (n, xn) measurements. However, further developments are considered in order to adapt the beam characteristics to particular measurements by studying and designing variable size collimators.
- Design the corresponding beam optics (beam tube and collimators) such as to achieve neutron and gamma backgrounds by order of magnitudes lower than the beam flux.
- Define the shielding elements such, as to improve the background attenuation and respect at the same time the conditions imposed by the CERN safety rules, which impose the accessibility and emergency escape paths of the installation.

The realisation of the present design implied complex and time consuming Monte Carlo simulations, in order to achieve quantitative solutions. Several codes based on different models and evaluated cross-section libraries, were used for this purpose (FLUKA [2], MCNPX [3], GEANT3 [4], GEANT4 [5] CAMOT [6] and EAMC [7]) and the results have been cross-checked among them, in order to asses their reliability. In this sense, our studies represent on themselves a benchmark between the most advanced codes available in neutron physics today.

## 2. The spallation source

A detailed description of the properties of the lead spallation target can be found in [8]. This section is devoted only to those characteristics of the target that have an impact to the definition of the neutron beam. The study of the CERN neutron source had, among others, two major goals:

- To evaluate the most relevant properties of the spallation source, such as the flux and its spectral function.
- To parameterise these properties in order to implement them in time efficient, but realistic, Monte Carlo simulations, necessary for most of the studies.

The neutron energies at the n_TOF extend closely up to 20 GeV due to the 20 GeV/c momentum of the PS proton beam. A FLUKA Monte Carlo simulated energy spectrum of the neutrons at the exit of the water moderator of the spallation target, is shown in Figure 1. The 38% of the neutrons emerge with energies below 0.3 eV. The range from 0.3 eV to 20 keV accounts for 23% of all neutrons and evidences almost exact isolethargic behaviour, as a consequence of the moderation in the water. However, a significant fraction 32% of the neutrons have energies between 20 keV and 20 MeV, and a further 7% extends above 20 MeV. Such a hard component, the signature of the spallation reactions, differentiates substantially the neutron energy distribution at the CERN facility from those of alternative neutron production mechanisms used in other neutron TOF facilities.

Figure 1. **Energy distribution (normalised to area unity) of the neutrons at the exit of the Pb target after the water moderator**

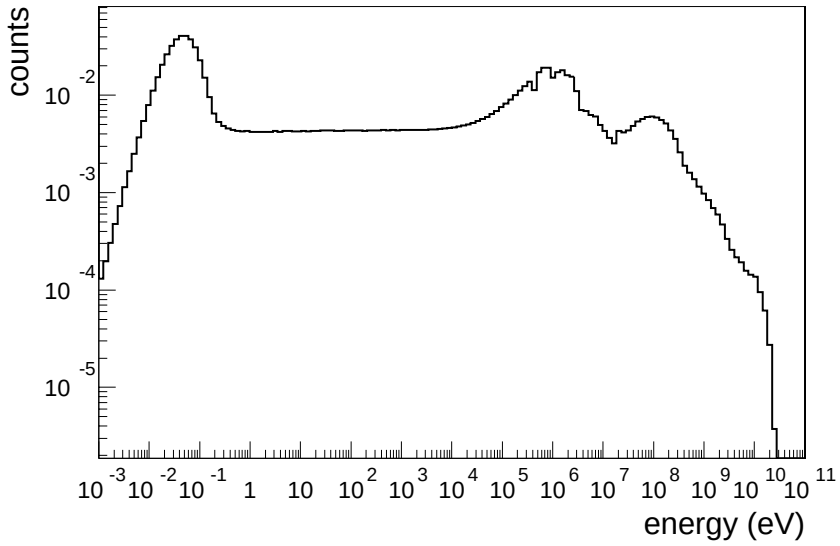

The simulation of the spallation process is excessively time-consuming for high-energy protons. An event generator appears to be necessary in order to perform effectively all calculations [9]. For this purpose, the interactions of the 20 GeV/c protons with the Pb spallation target (80 ×80 × 40 $cm^3$) were simulated by means of FLUKA [2] and EAMC [7]. A very detailed geometry of the target, the surrounding water moderator, the mechanical parts and the shielding was included. The position, energy, time and the direction cosines of the particles emanating entering into the TOF tube were recorded on a data summary tape (DST). We report here on the results obtained for the neutrons, but details about other emerging particles can be found in [8]. By taking the TOF tube as the z axis in a co-ordinate system, the proton beam lies in the y/z plane and enters into the target at x = y = 0 cm and z = -40 cm, forming an angle of $\theta = 10^o$ with respect to the z-axis. Such an incident angle balances the intensity losses in the neutron beam and its contamination due to high-energy charged particles, γ-rays and others. However, it introduces an asymmetry in the spatial distribution of the neutron source along the y-axis. The analysis of the DST provided the one-dimensional probability distributions of the neutron x- and y-positions, p(x) and p(y), the angular distributions of their momenta, p(θ) and p(ϕ), the time, p(t), and the energy, p(E), distributions. It was found that all single-variable distributions were strongly correlated with the neutron energy, and thus, its parameterisation was made as a function of the energy. Some illustrative examples can be found in Figure 2. In the upper left corner, the energy-time relation can be observed. Such relation is the working principle of the TOF measurements, since it links the time of flight with the initial neutron energy.

Figure 2**. Upper left: Time-energy relation of the spallation neutrons. Upper right: x and y projections of the spatial distribution of neutrons with energies between 1 MeV and 10 MeV. Lower left: cos(θ) distribution for neutron energies between 10 keV and 100 keV. Lower right: ϕ distribution for neutron energies between 100 MeV and 1 GeV.**

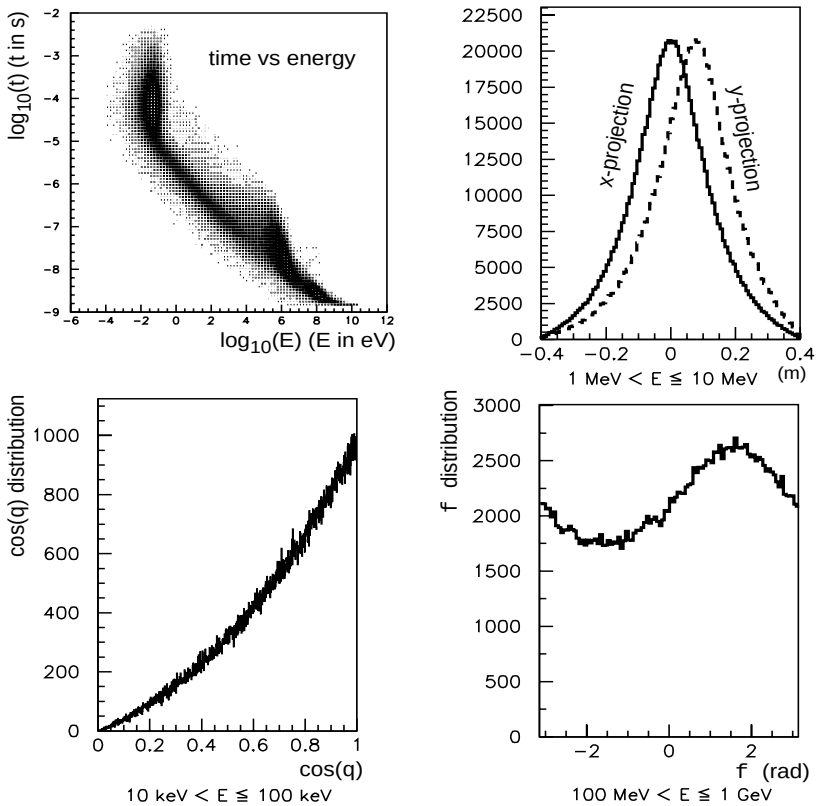

In the upper right corner of Figure 2, the x and y spatial distributions for neutron energies between 1 MeV and 10 MeV are shown. Both distributions are clearly not uniform and present pronounced peaks with similar r.m.s. values. It can also be observed that the centroid of the y-distribution is displaced towards positive values, while the x-distribution remains centred in x = 0. The displacement varies with the neutron energy ranging from 4.1 cm, for energies below 1 eV, to 6.6 cm, for energies between 10 MeV and 100 MeV, and 9.8 cm for energies above 1 GeV. The r.m.s of both distributions presents also energy dependence. For neutron energies below 1 eV, a broad distribution is obtained with a r.m.s of 15.9 cm. The width reduces to 12.9 cm for energies between 1 MeV and 10 MeV and gets its smallest value of 5 cm for energies above 1 GeV.

In the lower left corner, the cos(θ) distribution for energies between 10 keV and 100 keV is shown. It can be observed that the distribution is not uniform and that there is a clear preference of the neutrons to be emitted in the forward direction. The effect is enhanced for highest neutron energies. However, if only small emission angles of the neutrons are considered ($\theta << 1^o$), the overall effect can be treated as a global normalisation between the number of neutrons emitted in all θ directions and the neutrons emitted with cos(θ) values close to 1. The lower right corner of Figure 2 shows the ϕ distribution for neutron energies between 100 MeV and 1 GeV. It can be seen that these neutrons are emitted more likely in the $\phi = 90^o$ direction of the proton beam. The tendency is enhanced for neutrons above 1 GeV, which has the positive consequence of reducing the background produced by them close to the experimental area, situated 185 m downstream. However, the ϕ distributions for neutron energies below 100 MeV present a uniform behaviour. This allowed parameterising the neutron source to first order as the product of the single-variable distributions depending on the energy for the purpose of an *event generator*.

## 3. The beam optics

The optical elements of the installation are the beam pipe and the collimating system. The beam pipe defines the interaction-free transport medium where the neutrons can travel in vacuum up to the experimental area. A telescopic design was adopted for the pipe so that the tube does not intercept the neutrons arriving at the measuring station (185-200 m downstream): i) a first section being 70 m long with 80 cm diameter, ii) a second section being 68.4 m long with 60 cm diameter, and iii) a third section being 61.4 m long with 40 cm diameter. On the other hand, the collimating system is of fundamental importance as a background reduction element (shielding) and for providing a neutron beam of well defined size.

Table 1. **Parameters of the two collimators. The z co-ordinates are referred to the exit face of the Pb target. The samples are assumed to be placed at z = 185 m, where the beam has a spread of 2 cm radius or 4 cm diameter.**

| | **Design of the first collimator** | | | | | |
|---|---|---|---|---|---|---|
| | Material | Internal radius (cm) | External radius (cm) | Initial z coordinate (m) | Final z coordinate (m) | Length (m) |
| **Part 1** | Iron | 5.5 | 25 | 135.54 | 136.54 | 1 |
| **Part 2** | Concrete | 5.5 | 25 | 136.54 | 137.54 | 1 |
| | **Design of the second collimator** | | | | | |
| | Material | Internal radius (cm) | External radius (cm) | Initial z coordinate (m) | Final z coordinate (m) | Length (m) |
| **Part 1** | 5% borated Polyethylene | 0.9 | 20 | 175.35 | 175.85 | 0.5 |
| **Part 2** | Iron | 0.9 | 20 | 175.85 | 177.1 | 1.25 |
| **Part 3** | 5% borated Polyethylene | 0.9 | 20 | 177.1 | 177.85 | 0.75 |

From pure geometrical considerations, it can be realised that a beam of 2-cm radius at 185 m can be prepared if and only if the spallation target has a lateral size of almost 20 cm. This can be achieved by the use of an additional collimator which partially screens the Pb target. It should be pointed out that the spallation target should be considered an object consisting by two parts of the same material. A central cylindrical part of 20 cm radius representing the main part of the Pb spallation source is surrounded by an Pb reflector forming thus together an object of 40 cm radius, the actual TOF target. The advantages of Lead as spallation source and efficient reflector are well established [10]. It has been observed by Monte Carlo simulations that the neutron flux at energies below 1 MeV is increased about 50% due to this Pb reflector. The source screening by the additional collimator reduces the neutron flux, since the complete Pb target is no longer visible from the sample position through both collimators. However, this effect is less significant as naively expected, because the spatial distribution of the emanating neutrons is not uniform, but peaked at the centre of the Pb target. Moreover, the use of two collimators turns out to be the most effective way of reducing the neutron and $\gamma$ background in the experimental area. The screening of the neutron source reduces by one order of magnitude the number of neutrons hitting the second collimator, which represents the strongest source of background observed therein.

The position and inner diameter of the two collimators were optimised [11] by minimising the losses in flux and by leaving the possibility of future upgrades (already under study) open. In particular, the study considered explicitly a first collimator that is also appropriate for producing neutron beams of 8 cm diameter (or even broader). The optimal configuration is described in Table 1. The first stage consists of a 2 metres long collimator (Source Screening Collimator, SSC) at 135.54 m from the Pb target and with an inner aperture of 5.5-cm radius. The second stage is a 2.5-m long collimator (Beam Shaping Collimator, BSC) at 175.35 m from the Pb target and with an inner aperture of 0.9-cm radius. Such a configuration provides a neutron beam of 4-cm diameter at the sample location, 185 m downstream from the Pb target.

Figure 3. **Top view of the area where the BSC is located**

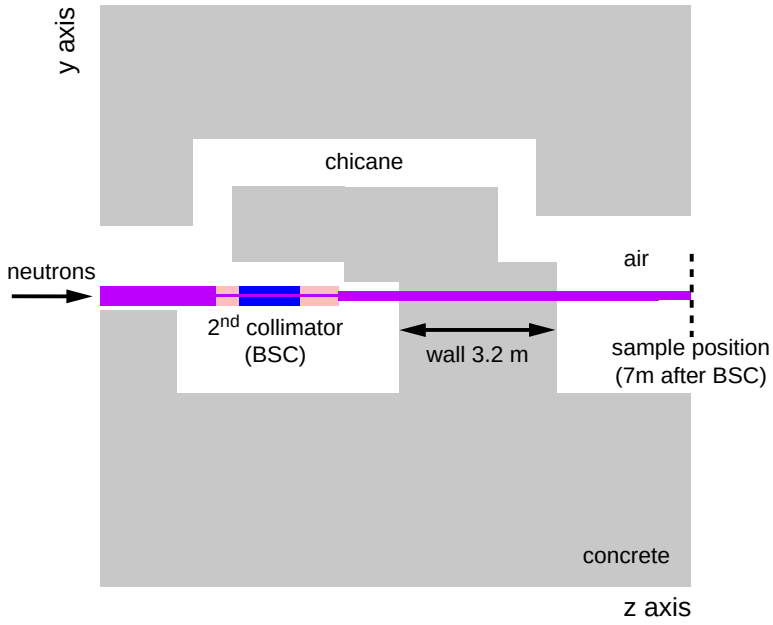


The optimal composition of the collimators was investigated as a separate issue by Monte Carlo simulations [2,3,4]. The best results were achieved when a combined or "sandwich-like" collimator is used [12]. In order to moderate the neutrons with energies below 20 MeV, a 40-50 cm long segment made of an hydrogen-rich compound doped with a neutron absorber (borated polyethylene – $CH_2^B$ – in our case) was found to be very efficient. On the other hand, the neutrons above 20 MeV can not be efficiently stopped in $CH_2^B$. A 1 m long segment of an intermediate Z material (natural iron in our case) was found to be necessary and optimal for moderating, through elastic and inelastic scattering, the high-energy part of the TOF spectrum. For this reason, the SSC consists of a 1 m of iron and a 1 m of concrete cylindrical segments. A much more careful design was made for the BSC, only 5-7 m away from the measuring station, where the lowest background rates are required. Thus, a design based on three segments was adopted. The first part of the BSC, made of 50 cm of $CH_2^B$ moderates and captures most of the neutrons below 20 MeV. The second part, made of 1.25-m iron, moderates and diffuses the high-energy neutrons below 20 MeV. The third part of the BSC, made of 75 cm of $CH_2^B$ moderates and captures the neutrons scattered in the preceding iron segment.

## 4. The shielding elements

Several shielding elements have to be placed outside the TOF tube in order to bring the background at the experimental area to an optimal level. It has been observed by Monte Carlo simulation that it is of crucial importance to avoid high-energy neutrons (above several tens of MeV) reaching the vicinity of the experimental area and produce secondary particles. Thus, the best strategy is to take profit of the geometrical factor, by placing the shielding elements as far away as possible from the measuring station.

Figure 4. **Radial distribution of the neutron beam profile and the neutron background at the sample position. The values correspond to the neutron fluence through concentric cylinders: the first 20 cylinders with radial increments of 1 cm and the last 7 as indicated in the figure.**

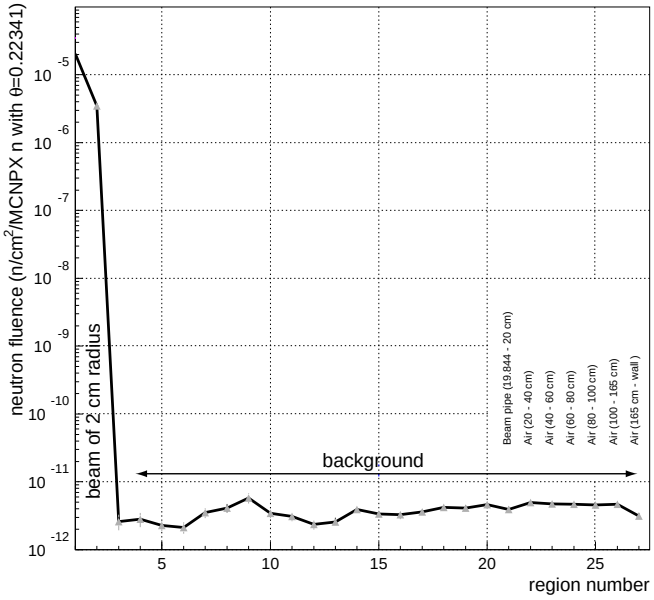


The first important shielding element is the pipe itself. Several tens of metres after the Pb target, the incidence angle of the neutrons hitting the pipe is small and the effective length of material seen by the neutrons is large. In this way, a large fraction of the neutrons are deviated from its initial trajectory and produce background in the upstream half of the tunnel. Due to the telescopic structure of the pipe, the places at the diameter reductions (80 cm to 60 cm and 60 cm to 40 cm) should be reinforced, since the neutrons traverse the pipe almost perpendicularly. At these positions, the pipe was covered after the reduction with 1-m thick external iron cylinders.

The second important shielding element is the first collimator (SSC) starting at 135.54 m. Such a strong scattering centre had to be shielded by a 3 m concrete wall. After the SSC, the neutron beam divergence is small and the neutrons do not hit the pipe before the second collimator (BSC). The 2.5 m long BSC diffuses and moderates very efficiently the whole neutron spectrum. However, it is a strong scattering centre that has to be efficiently shielded by a 3.2-m thick wall, placed 1 m beam-downstream. Figure 3 shows the top view of the area in scale, where the BSC is located, as has been designed for the MCNPX simulations. The 2.5-m long BSC is observed on the left-hand side of the 3.2-m concrete wall. Also visible is the chicane, a necessary escape path in case of emergency. The impact of this shielding opening on the background at the sample position was studied with Monte Carlo simulations.

The neutron beam profile and background at the sample position is shown in Figure 4. All the values correspond to the neutron fluence of concentric cylinders: the first 20 values with radial increments of 1 cm and the last 7 as indicated in the figure. The first two bins correspond to the main neutron beam, which has a radius of 2 cm. The remaining bins correspond to the background level at the different places. It can be seen that the neutron background is on average at the level of $2 \cdot 10^{-12}$ n/cm$^2$ per neutron emitted from the Pb target with a $\theta$ angle smaller than 0.223º. Such a value, when compared to the beam fluence of $2 \cdot 10^{-5}$, leads to a background to signal ratio of $10^{-7}$. This background level is of the same order than the background of scattered neutrons produced at 15 cm from a 10 mg $^{235}$U sample placed in-beam. A similar result was found for the $\gamma$ background produced

by neutron reactions. The level reached at a separation of 7 metres from it is $10^{-7}$ times smaller than the neutron beam shown in level by another by factor of ten. Such a value is comparable to the gammas emitted by a 10 mg $^{235}$U sample. At 15 cm distance, the γ fluence is also seven orders of magnitude below the neutron beam fluence. As a general remark, it should be noticed that applying the necessary time of flight cuts would reduce the background levels shown in this section. In addition, several possibilities of reducing the neutron and γ background in the experimental area were also investigated. From the Monte Carlo simulations with GEANT and MCNPX, it was early observed that covering the walls with some neutron moderator and γ shielding could diminish the background level by another factor of ten.

Figure 5. **Various projections of the beam profile at 5 and 7 metres after the BSC´s for 1 keV neutrons**

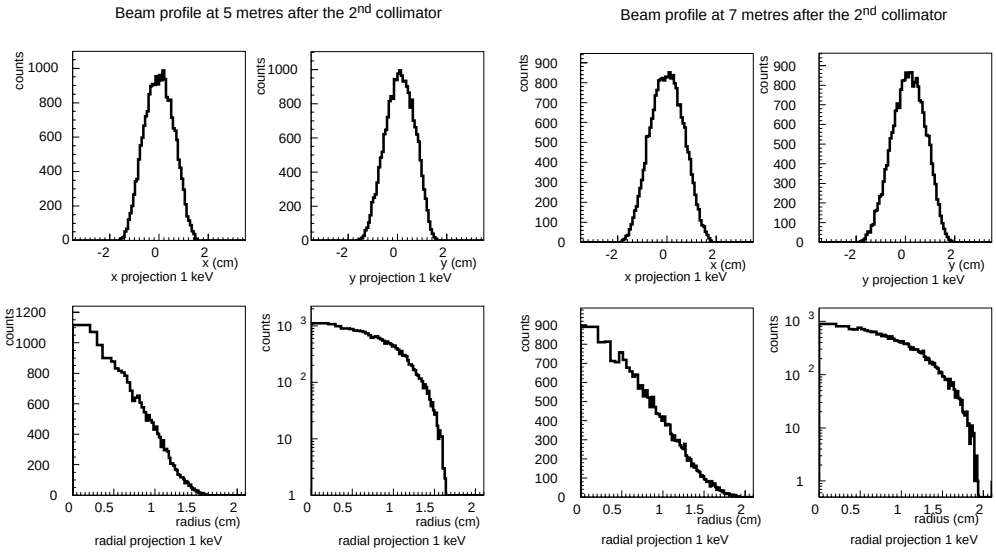


## 5. The beam at the experimental area

The neutron beam at the first phase of the n_TOF operation will have a maximal spread of 2-cm radius. Although the maximal size of the beam does not depend on the neutron energy, due to the energy dependence of the neutron spatial distributions at the exit of the Pb target, the beam profile at the sample position does also depend on the energy. The beam profile has been calculated by the geometric transport through the collimators for different neutron energies. Figure 5 shows various projections of the beam profile for 1 keV neutrons at several positions after the BSC. It can be observed from the radial projection in Figure 5 how the beam spread at 7 m after the BSC's end is inside the desired limit of 2 cm. However, it should be noticed that 5 m after the BSC, the beam spot is smaller and has a diameter of 3.2 cm. Thus, it remains to the particular experiment to decide which beam size has to be adopted.

It has been calculated by Monte Carlo simulations (FLUKA [2]) that for a PS bunch of $7{\cdot}10^{12}$ protons, the fluence in absence of collimators is of $7{\cdot}10^{5}$ n/cm$^2$. With the described collimating system, the fluence amounts to $1.3{\cdot}10^{5}$ n/cm$^2$ per proton bunch, which is smaller by a factor of 5. It should be emphasised that this loss in fluence is sine qua non to the definition of a neutron beam and a TOF facility fulfilling the requirements and providing the clean conditions necessary for experimentation.

## 6. The neutron escape line

The common experimental situation is that most of the neutrons in the beam do not interact with the samples. They continue its path undisturbed until it is finally interrupted by any interposed construction element. Such neutrons are a potentially dangerous source of background, since their interactions with the surrounding materials in the vicinity of measuring station can interfere with the experiments. It is necessary that they continue unperturbed its travelling for a long distance before being scattered. A typical solution adopted at other TOF facilities is to have an experimental area of large dimensions (several tens of metres). There the neutrons can travel (in air or vacuum) a long path before being scattered and finally absorbed. In addition, the background introduced by them can be highly suppressed by the TOF tagging, since the escape path is usually comparable (or larger) in length than the TOF distance.

Figure 6. **Geometry of the neutron escape line as included in the MCNPX simulations**

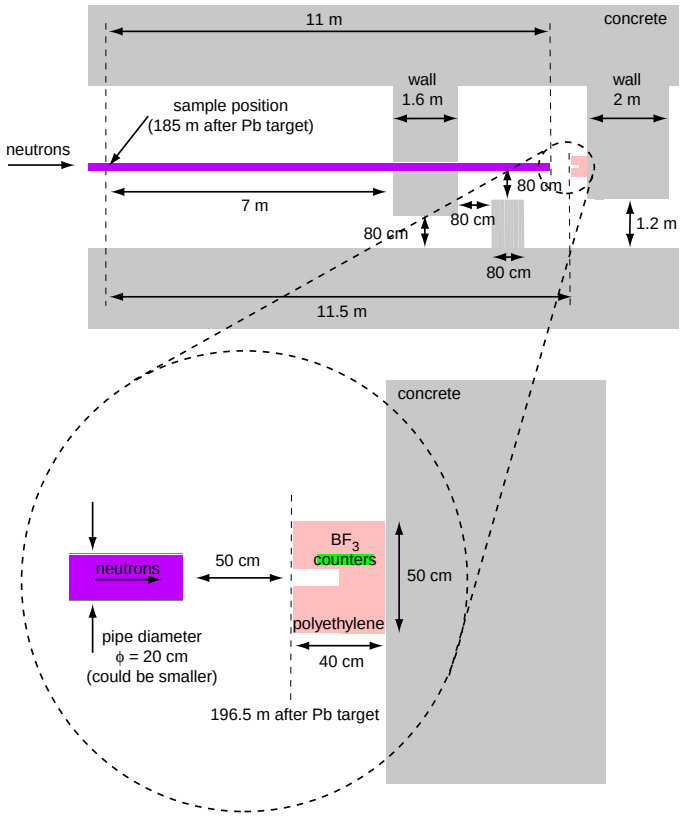


However, the particular situation at the n_TOF makes the mentioned strategies difficult to be applied. First, the facility is located inside a small closed cave, which limits severely the size of the experimental area. Second, the TOF tube hits the ground at 200 m from the Pb target, just 15 m after the measuring station. This situation introduces an unavoidable source of background close to the measuring station. Third, such a distance is much smaller than the 185 m TOF flight path, which affects the suppression capabilities of the time tagging. Fourth, the high-energy component of the neutron energy spectrum. All this considerations make preferably to design a neutron escape line and a beam dump at its end (properly shielded) instead of having the uncontrolled collision of the neutron beam with the floor at 200 m. Additional motivations for the neutron escape line from radio-protection considerations have not been studied.

The geometry of the beam dump proposed and included in the simulations can be seen in Figure 6. At the leftmost part of the figure, the sample position at 185 m from the Pb target is marked by a dashed line. After it, the unperturbed fraction of the neutron beam continues its travelling in vacuum for another 11 m, inside an aluminium pipe. It is worth to mention that the tube considered in our study has a diameter of 20 cm, which is larger than really necessary. As it is shown in Figure 6, the neutron beam has a maximal spread of 8 cm diameter at 200 m, which would allow the use of a smaller pipe diameter. However, in order to make sure about the conclusions, it is preferable to know that the number of neutrons backscattered at the beam dump is even acceptable for a broader tube (larger geometric acceptance).

After the 11 m flight path, the neutrons cross a 1 mm thick tube end cup and enter into air. Several materials for the tube end cup have been studied: 1 mm of Al, 1 mm of natural Fe, 1 mm of carbon fibre and also the ideal case of no end cup (only vacuum). The MCNPX [3] Monte Carlo simulations revealed no influence of the end cup election on the background distribution at the sample position.

After the vacuum pipe and 50 cm of air, the neutrons first enter into a $40 \times 50 \times 50\ cm^3$ polyethylene block followed by a 2 m thick concrete wall. The polyethylene block has two main purposes. First, it preferences the scattering of the neutrons in the forward direction, thus reducing the background in the upstream area. Second, it is the frame for a monitoring detector array based on three $BF_3$ detectors. The 2-m thick concrete wall behind the polyethylene block is in charge of further moderation and absorption of the neutrons. Only the neutrons of highest energies, above several tens of MeV are capable to cross it.

In order to minimise the number of scattered neutrons entering back into the experimental area, a 1.6-m thick concrete wall is interposed in their way. The wall is placed at 7 m from the sample position, as far as possible from the point of view of the neutron and $\gamma$ background. Also visible in Figure 6 is the 80 cm broad opening in the wall, necessary from the point of view of safety. Nevertheless, the opening is covered by an additional 80-cm thick concrete shielding forming a chicane. By keeping the distance of this shielding to the centre of the pipe, also 80 cm, the neutrons can go through the wall opening only after having suffered more than one interaction.

It should be said at this point that the geometry of the tunnel described in Figure 6 is only an approximation to the real one. The curvature of the tunnel and its slope were not included. However, if the distances marked in the figure are kept as they are, the results for the real geometry must be the same or better, since the approximations made were always done by following the tendency of increasing the background at the experimental area. Moreover, the geometry described in Figure 6 allows further improvements, because the dimensions of the present shielding elements are not at its practical limits. For example, there is still space for enlarging them or moving all the shielding elements 2 metres away from the sample position. However, the present configuration provides already satisfactory results.

Figure 7. **Neutron background at the sample position. The values correspond to the neutron fluence through concentric cylinders: the first 20 cylinders with radial increments of 1 cm and the last five as indicated in the figure.**

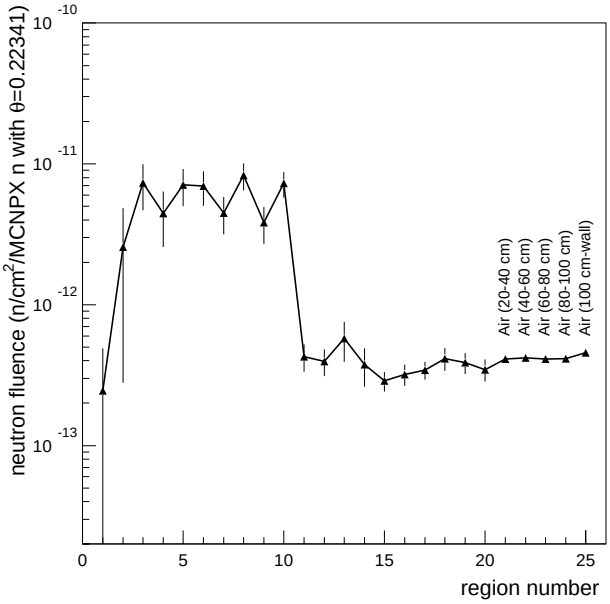


The lower part of Figure 6 is an enlarged view of the beam dump at the end of the neutron escape line. Three commercially available $BF_3$ detectors are embedded on the polyethylene block forming a long counter [13]. The hole of 4-cm radius is only necessary for the $BF_3$ long counter working principle. The main goal of this monitoring set-up is to control possible variations in the gross properties of the neutron beam such as its intensity or its position. Figure 7 shows the radial distribution of the neutron background at the sample position. All the values correspond to the neutron fluence through concentric cylinders: the first 20 values with radial increments of 1 cm and the last five outside the pipe as indicated in the figure. Such a background can be compared directly to the previously shown in Figure 4. Two different components can be observed. The first one corresponds to the initial 10 bins and accounts for the neutrons scattered at the beam dump and travelling back inside the pipe. Such a background can be considered as a negligible contamination of the beam of 1 part in $10^6$ (see Figure 4 to compare with the main beam). A suppression if this background can be achieved by placing a sheet of Cd in front of the polyethylene block. The second component is the neutrons travelling outside the pipe, which arrived at the experimental area either by crossing the tube hole or the opening in the wall. This background is at the same level as the one in Figure 4, that is, seven orders of magnitude below the main neutron beam. The energy distribution of the background at the sample position shows that 95% of the neutrons have energies below 1eV. In order to investigate if such neutrons are coming from the moderation of higher energy neutrons or had initially thermal energies, a Monte Carlo simulation was performed with an energy spectrum starting at 1 eV. The result is that 53% of the thermal neutrons at the sample position are produced by neutrons of energies higher than 1 eV. The other 47% is already originated by neutrons with initial thermal energies. This implies additional background suppression because the neutron energy spectrum at the sample position is affected at energies below 0.1 eV because of gravitation. In fact, gravitation will make that the thermal neutrons emitted from the Pb target fall down along the TOF path of 200 m and do not reach the samples. The Monte Carlo simulations revealed also that at the sample position, the $\gamma$ background due to the beam dump is at least 7 orders of magnitude below the main neutron beam.

## REFERENCES


[1] S. Abramovich *et al*., *Proposal for a Neutron Time of Flight Facility*, CERN/SPSC 99-8, (March 1999).

[2] A. Ferrari and P.R. Sala, *Intermediate and High Energy Models in FLUKA: Improvements, Benchmarks and Applications*, Proc. of Int. Conf. on Nuclear Data for Science and Technology, NDST-97, ICTP, Miramare-Trieste, Italy, May 19-24 (1997).

[3] Laurie S. Waters, Editor, *MCNPX Users Manual*, TPO-E83-G-UG-X-00001, Los Alamos National Laboratory (1999).

[4] GEANT3, *Detector Description and Simulation Tool*, CERN Program Library W5013, Geneva (1994).

[5] GEANT4, http://wwwinfo.cern.ch/asd/geant4/geant4.html.

[6] C. Coceva, M. Magnani, M. Frisoni, A. Mengoni, *CAMOT: a Monte Carlo Transport Code for Simulations of Pulsed Neutron Sources*, Unpublished (2000).

[7] H. Arnould *et al.*, *Neutron-driven Nuclear Transmutation by Adiabatic Resonance Crossing: TARC*. EUR 19117. Project Report of the NST of EURATOM of the EC. ISBN 92-828-7759-0 (1999).

[8] E. Radermacher, Editor, *Neutron TOF Facility (PS 213) – Technical Design Report*, CERN (February 2000).

[9] D. Cano-Ott *et al.*, *First Parameterisation of the Neutron Source at the n_TOF and its Influence on the Collimation System*, DFN/TR-03/II-00.

[10] H. Arnould *et al.*, *Experimental Verification of Neutron Phenomenology in Lead and Transmutation by Adiabatic Resonance Crossing in Accelerator Driven Systems*. Phys. Lett. B 458 (1999) 167.

[11] D. Cano-Ott *et al.*, *Proposal for a Two-step Cylindrical Collimator System for the n_TOF Facility*, DFN/TR-04/II-00.

[12] D. Cano-Ott *et al.*, *Design of a Collimator for the Neutron Time of Flight (TOF) Facility at CERN by Means of FLUKA/MCNP4b Monte Carlo simulation*, DFN/TR-07/II-99.

[13] A.O. Hanson and M.L. McKibben, Phys. Rev. 72, 673 (1947).

# RECENT CAPTURE CROSS-SECTIONS VALIDATION ON $^{232}$TH FROM 0.1 EV TO 40 KEV AND SELF-SHIELDING EFFECT EVALUATION

**L. Perrot, A. Billebaud, R. Brissot, A. Giorni, D. Heuer, J.M. Loiseaux, O. Meplan, J.B. Viano**
Institut des Sciences Nucléaires/CNRS-IN2P3/UJF
51 avenue des Martyrs, 38026 Grenoble, France

## Abstract

Research on ADS, related new fuels and their ability for nuclear waste incineration leads to a revival of interest in nuclear cross-sections of many nuclides in a large energy range. Discrepancies observed between nuclear databases require new measurements in several cases. A complete measurement of such cross-sections including resonance resolution consists in an extensive beam time experiment associated to a long analysis. With a slowing down spectrometer associated to a pulsed neutron source, it is possible to determine a good cross-section profile in an energy range from 0.1 eV to 40 keV by making use of a slowing-down time lead spectrometer associated to a pulsed neutron source. These measurements performed at ISN (Grenoble) with the neutron source GENEPI requires only small quantities of matter (as small as 0.1 g) and about one day of beam by target.

We present cross-section profile measurements and an experimental study of the self-shielding effect. A $CeF_3$ scintillator coupled with a photomultiplier detects gamma rays from neutronic capture in the studied target. The neutron flux is also measured with a $^{233}$U fission detector and a $^{3}$He detector at symmetrical position to the PM in relation to the neutron source. Absolute flux values are given by activation of Au and W foils. The cross-section profiles can then be deduced from the target capture rate and are compared with very detailed MCNP simulations, which reproduce the experimental set-up and provide also capture rates and flux. A good agreement between experimental and simulated profiles for well-known cross-sections like Au for different thicknesses is found in our energy range, and therefore validates the method and the taking into account of self-shielding effects.

The method is then applied to $^{232}$Th, of main interest for new fuel cycle studies, and is complementary to higher energy measurements made by D. Karamanis *et al.* [1] (CENBG). Results obtained for three target thicknesses will be compared with simulations based on different data bases. Special attention will be paid to the region of unresolved resonances (>100eV).

## 1. Introduction

At the dawn of XXI century, energy is a crucial problem to study. By 2050, it is predicted the energy demand will double. In the same time, some greenhouse effect emission scenarios predict approximately the same increase. The nuclear energy contribution in the energy production represents 4.5%. Nuclear utilisation and further development can be one of the possible responses to the increase of energy demand and the greenhouse effect limitation.

However, it is necessary to minimise the radioactive waste production such as actinides and long-lived fission products and this can be obtained by using the $^{232}Th/^{233}U$ fuel cycle, in an accelerator driven system or critical reactors.

But a good prediction for this new way of producing energy is strongly dependent of the material neutronic properties and more particularly the $^{232}Th$ capture cross-section for the fuel.

In the present work, an experimental method is proposed that carries out a validation of available databases. A lead slowing down spectrometer coupled with a neutron pulsed generator allows to measure reaction rates (n,γ) or (n,f) over a wide energy range from 0.1 eV to 40 keV for different thicknesses of material. Experimental data are then compared with precise simulation calculation using ENDF/BVI, JEF2.2 and JENDL3.2 databases.

The gold results for which the capture cross-section is well know, provides a validation of the method for three different thicknesses. Tantalum, indium and thorium data for three thicknesses (for self-shielding effect studies) are presented. The accuracy of the validation method is estimated to be around 5%. From 0.1 eV to 300 eV, it is shown that predictions of reaction rates using the different databases agree between themselves and with the experimental data. From 300 eV up to 40 keV discrepancies between database predictions can be as large as ±20%. The experimental data allow to either indicating the best databases to be used, or the need to measure again the cross-section in a certain energy range. For the $^{232}Th$, experimental capture rate data agrees with the prediction of ENDF/BVI and JEF2.2 bases within 5%.

## 2. The experimental set-up

### *2.1 The neutron source*

This accelerator has been specially designed for neutronic experiments taking place in the nuclear reactor MASURCA located at CEA Cadarache Centre (France). In fact, for these experiments the neutron pulse length must be of the order of the neutron lifetime in a fast reactor. The pulse intensity must be as big as possible.

The GENEPI (GEnérateur de NEutrons Pulsés Intense) produced fast pulses. The pulse duration is typically 1.0 μs. Deuterons are produced by a duoplasmatron source, especially studied for a pulsed use. The frequency can vary from a few Hz up to 5 000 Hz. The deuterons are accelerated at the maximal energy of 250 keV. The maximum peak intensity is 50 mA. The deuterons are focalised through a long five meters tube (glove finger) on a deuterium or tritium target. The nuclear reactions $D(d,n)^3He$ or $T(d,n)^4He$ product neutrons with an energy of respectively 2.67 MeV and 14.0 MeV. This accelerator can produce in the case of a tritium target $5.0\ 10^6$ neutrons/4π per pulse [8].

Figure 1. **The GENEPI accelerator and the slowing down time spectrometer**

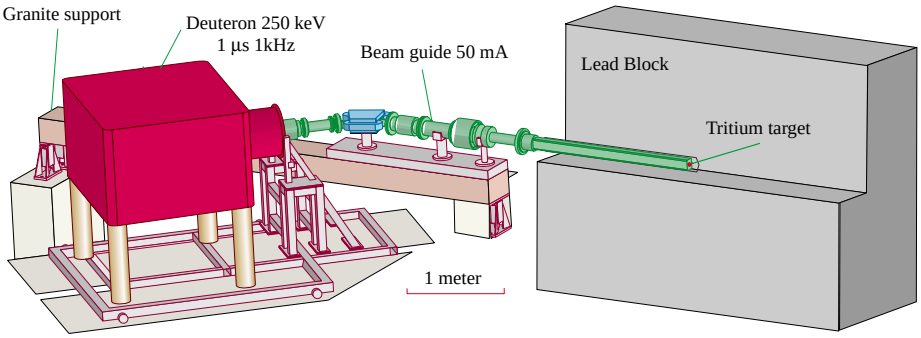


### *2.2 The slowing down time spectrometer*

The slowing down time spectrometer is an assembly of 46.45 tons of lead with a cubic symmetry in a relation to the beam axis GENEPI. The neutron production took place in the centre of the lead block. This block is made up of 8 blocks having the following dimensions: 80 × 80 × 80 $cm^3$. Each block has two channels (10 × 10 $cm^2$ in section) parallel to the beam axis. They are used both for handling of the block and for insertion of detectors. In the last case, the dimensions of the holes are reduced to 5 × 5 $cm^2$. Pure lead (99.99%) was chosen to ensure that impurities have negligible effect on the neutron flux. Impurities of lead are less than 5 ppm, principally silver, bismuth, cadmium, copper, antimony, tellurium. The lead block is shielded with a cadmium foil to capture the neutron escaped from the lead block and backscattered by concrete walls, which can deteriorate the energy-time correlation.

In a slowing-down time lead spectrometer, there is a correlation between the neutron time of flight in the block and its kinetic energy. The scattering mean free path of a neutron in the lead medium, $\lambda_s$ = 2.76 cm, is about constant over the energy range 0.1 eV to a few tens of keV. The relation between the slowing down time and the neutron mean energy can be written in this form [2]:

Figure 2. **The energy-time correlation from MCNP calculation**

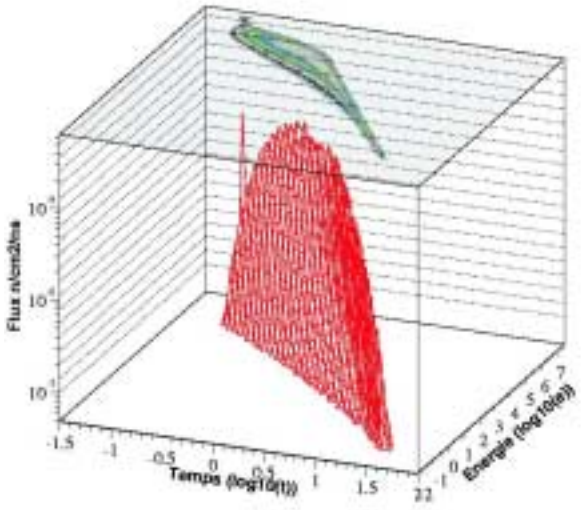


$$\overline{E} = \frac{K}{(t + t_0)^2} \qquad K = 166 \pm 1 keV\mu s^2 \qquad t_0 = 0.5\mu s$$

The K parameter value, function of the neutron masse $m_n$, the scattering mean free path $\lambda_s$ and the medium properties, has been experimentally determined and well understood by MCNP calculation. The quantity $t_0$ can be considered as a time correction owing to the fact that the initial neutron is not created at infinite energy but at energy $E_0$ = 14 MeV and at velocity $v_0$, it suffers inelastic or (n,2n) reactions before being slowed down only by elastic scattering [4].

## *2.3 Detectors*

### *2.3.1 Neutrons source monitoring*

The reaction on the target produces associated charged particles: α in the case of T(d,n)α reaction and protons in the D(d,p)T reaction which occurs about as often as the D(d,n)$^3$He reaction. The charged particle is emitted with a 180° angle with respect to the neutron. For 0° neutrons, the charged particle goes upstream the incident beam, being focused in the glove finger and is bent by the GENEPI magnet. Two silicon detectors are placed side by side in the vacuum of the magnet chamber. They detect both the α and the p associated to the d(d,p)n reaction, as fortunately they have the same magnetic rigidity. One of them is covered with a 10 μm aluminium foil to stop the α particle. We can measure then through α detection the relative source of 14 MeV neutrons and through p detection of 2.5 MeV neutrons due to $D^+$ implantation in the T target.

### *2.3.2 Neutron spectrum normalisation*

The detector used for neutron spectrum normalisation is a classical proportional $^3$He-gas counter belonging to a series of counters developed at ISN Grenoble for fast neutrons spectroscopy in reactor. We detect the p and/or t produced by the reaction $^3$He(n,p)T, Q = 764 keV. It collects energy deposited by the products of the exothermic reaction. The effective zone is a 6 cm long cylinder of 1 cm in radius. The counter is filled up with 70 mbar of $^3$He, 3.3 bars of Argon and 2.5 mbar of $CO_2$ (quencher gas). The detector is described in Figure 3. It is placed at a symmetrical position to the (n,γ) detector in relation to the beam axis.

Figure 3. **Mechanical structure of the $^3$He gas proportional counter detector**

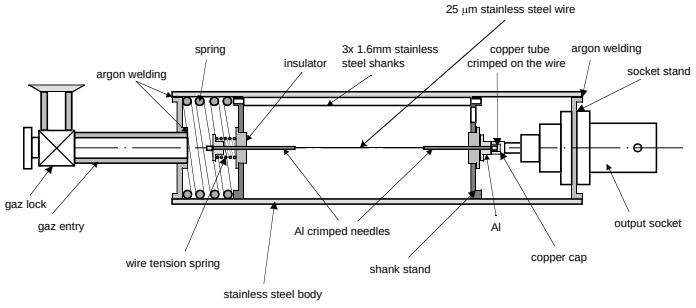

*2.3.3 Neutron flux measurements*

- Absolute calibration

  The integral flux is measured by activation of nickel foils. These foils are put against the GENEPI target. The dimensions of the foils are about 5 mm in radius and 0.5 mm in thickness. Six hours of irradiation with an intensity of 66 μA are enough to reach saturation. Following reactions are used: $^{58}Ni(n,2n)^{57}Ni$ with a threshold 13 MeV, $^{58}Ni(n,np)^{57}Co$ with a threshold 13 MeV. These activated foils are then counted in the low radioactive laboratory at ISN.

- $^{233}U$ fission detector

  The GENEPI neutron pulse, generated at time zero by the reaction $T(d,n)\alpha$ in the lead block centre region, gives at position <r> a neutron flux $\phi(E,t, <r>)$ which is measured with a detection system using the exothermic reaction $^{233}U(n,fission)$. The reaction rate versus time is proportional to the quantity $\phi(E,t, <r>)\sigma(E)$. Assuming that the cross-section $\sigma(E)$ is known, the measurement of the reaction rate gives an experimental access to the quantity $\phi(E,t, <r>)$. The fission fragments produced in the reaction $^{233}U(n,fission)$ (Q = 180MeV) are collected by a silicon detector. The $^{233}U$ target of 200 μg/cm2 is pure electro-deposited $^{233}U$ on a 200 μm thick aluminium foil. This small detection device is enclosed in lead. Two small charge-preamplifier are connected to the detectors inside the steel cylinder [4].

*2.3.4 Capture rate reaction measurement*

A scintillator coupled with a photomultiplier is used for sample (n,γ) reaction rate measurements. The PM is a XP1911 type from Philips [5]. It was chosen for its reduced dimensions ($\phi$ = 19 mm). Teflon has been chosen for the embase material, to avoid hydrogen and subsequent neutron energy degradation. PM gain variation has been minimised by adequate decoupling capacitances. $CeF_3$ scintillator has been chosen for its quick time response time (30 ns) and for its low neutron captures cross-section. The detection system and the sample embedded in a lead box in order to have a good reproducibility of the detection geometry. Every two samples, the background has been systematically measured in order to check the stability of the PM gain. The beam intensity was adjusted to have a low dead time for each sample (0.1 evts/pulse during the first 10 μs). This detector and its lead box are shown in Figure 4.

Figure 4. **Picture of the PM in its lead box**

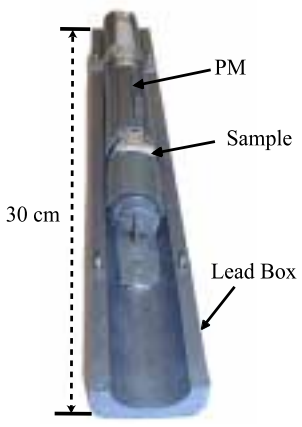

## 3. Experimental results

The detector signals are recorded with a timing module referenced to the neutron source pulse with 100 ns precision. For each detector, time spectra are built giving the number of events as a function of the time of flight of the associated neutron.

### *3.1 Flux measurements*

The $^{233}$U fission rate $\sigma_f\phi(t)$ is obtained with the silicium detector as described above. The $\alpha$ emission due to $^{233}$U disintegration introduces a background in the fission rate time spectrum. Fortunately, the energy deposition of fission products and $\alpha$ particles in the silicium can easily be separated allowing building a pure fission rate time spectrum. Assuming the same efficiency for $\alpha$ and fission products detection and knowing the neutron production (Ni foil activation, 1.7 $10^6$ neutron per pulse), the fission rate $\sigma_{(n,f)}\phi(t)$ could be normalised per source neutron. In Figure 5 the time spectrum exhibits at 300 μs a peak corresponding to the well-known 1.7 eV $^{233}$U fission resonance.

Figure 5. **Timing spectra of the $^{233}$U detector: 200μg/cm$^2$**

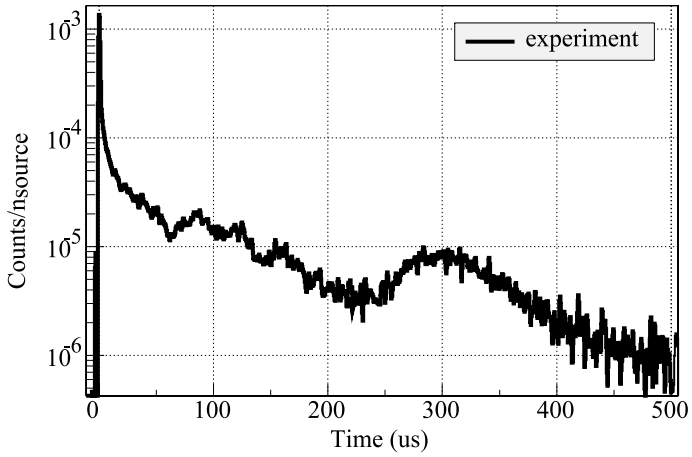


### *3.2 Neutron flux monitoring*

For these measurements we used a $^3$He gas detector. The Figure 6 presents a typical time spectrum obtained with this counter. The (n,p) cross-sections is particularly smooth in the $10^{-4}$ eV to 1.0 MeV energy range and elastic cross-section is negligible under 100 keV. Therefore we have a good assurance that the flux is the same in these two holes, one of them being used afterwards for capture rate measurements. The figure shows the good agreement between two measurements made in symmetrical channels.

Figure 6. **Time spectrum of $^{3}$He gas detector in two measurements holes of lead block**

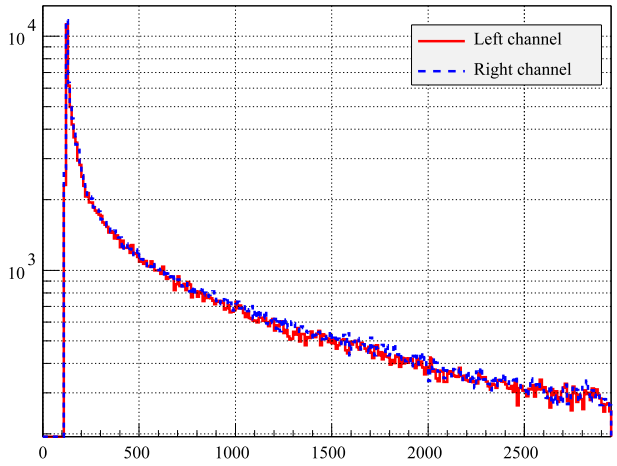


### *3.3 (n,γ) experiments*

#### *3.3.1 Background study*

The photomultiplier with the scintillator and the sample embedded in the lead housing are inserted in a channel of the lead block. This detection system is very sensitive to gamma rays emitted by neutron captures in surrounding materials. Therefore background measurements and a good understanding of its structure are necessary.

The Figure 7 shows a background measurement. The general exponential dependence is due to the decrease of the neutron flux associated with the scattering process in the lead block. Super-imposed structures can be seen which are due to neutron capture resonances in various nuclides. This background has been simulated taking into account all the elements contained in the detection system itself ($CeF_3$ scintillator, PM) and in the lead impurities, with proportions as free parameters. Measured and simulated spectra over a 300 μs time range are showing in Figure 7.

Figure 7: **Experimental (full line) and simulated reconstructed (dotted line) background time spectra with energy of the resonances and identification of associated nuclides**

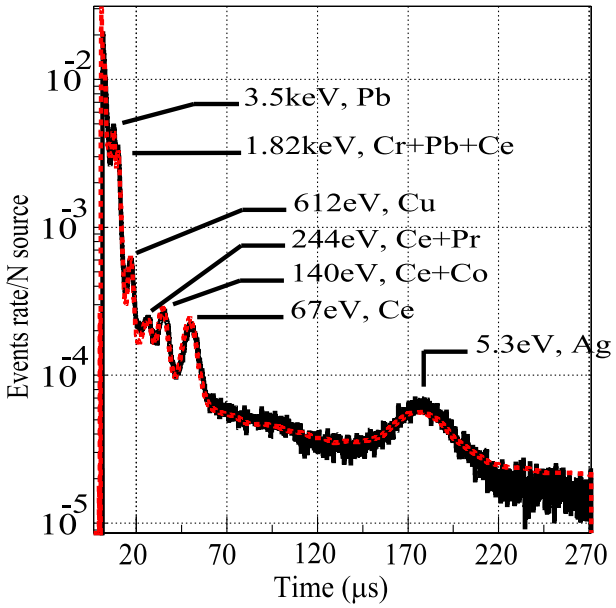


*3.3.2 Results for gold and thorium targets*

Figure 8 shows the normalised reaction rate for thorium and gold. Due to a larger cross-section gold spectrum is less affected by the background. The large structure that appears at 180 µs correspond to the 27 000 barns well-known 4.9 eV resonance. In the case of thorium a high radioactivity level is observed above 140 µs. The peak at 85 µs is due to the 21.8 eV and 23.5 eV unresolved resonances.

Figure 8. **Capture rate for gold (left) and thorium (right)**

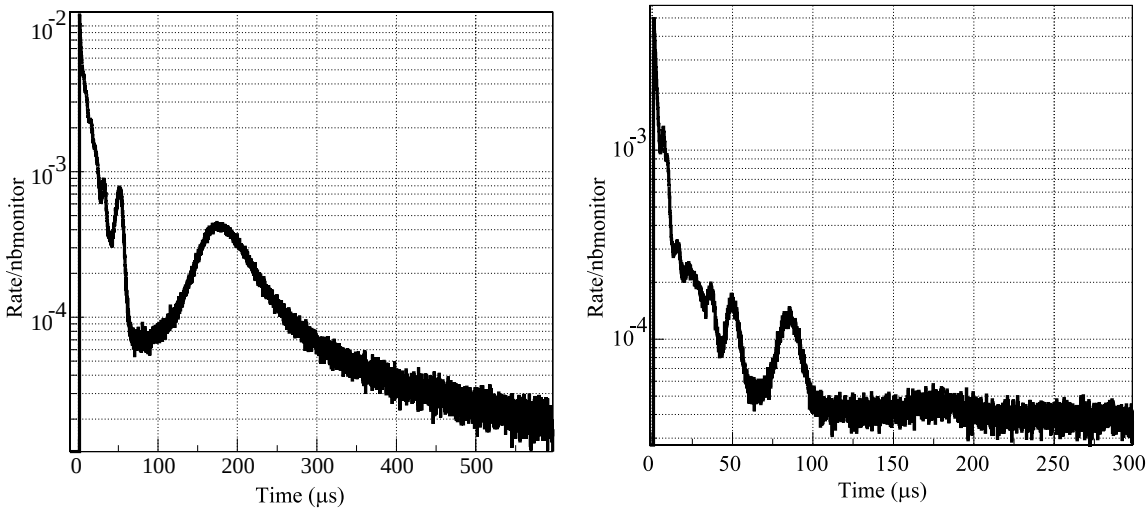

## 4. Analysis

### *4.1 Background subtraction method*

All spectra are normalised by the counting rate of the $^{3}$He reference monitor. Due to the self-shielding effects in the target, the background subtraction cannot be directly made. Thus, we proceed in three steps. Both activation and natural radioactivity induce a constant counting rate over the whole time range. This constant level for background and target can be measured when the neutron flux becomes negligible i.e. for time bigger than 2 ms. The first steps consist in subtracting this level for each spectrum. In a second step, measured background must be corrected as it is higher than its real contribution in the presence of the target, γ-rays due to captures in the surrounding materials being slightly absorbed in the target. This correction is evaluated according to the density and the thickness of the target. The last step consists in taking into account the neutron flux perturbation induced by the target. This correction factor is obtained by the ratio of simulation performed with and without target.

As the last this corrected background is subtracted from the spectrum obtained in the first step. It must be noticed that the two last corrections are second order effects.

### *4.2 Monte Carlo simulation*

We use the MCNP/4B code for simulations [7]. This code allows a very detailed description of the experimental set-up: detectors, generator components, lead block and concrete walls. The reaction rates $\sigma(n,\gamma)\phi(t)$ are calculated in order to be directly compared with experimental data. Three different databases have been used: ENDF/B-VI, JENDL3.2 and JEF2.2.

### *4.3 Simulation and experimental results*

Simulation provides capture rate per source neutron as a function of time. Both the simulated and experimental time spectra are converted into energy spectra, by means of the time-energy correlation described in a previous section. The simulations to experiment ratios are calculated for each energy bin, and are presented in Figures 9 to 12. We present 4 targets results: Au in order to validate the procedure, tantalum, indium and at last, we present the thorium target results of main interest for new fuel cycle studies.

Figure 9. **ENDF/B-VI and JEF2.2 simulation to experiment ratio for 1250 μm, 500 μm and 125 μm Gold samples in the energy range from 0.1 eV to 40 keV. The large grey box around C/E = 1 correspond to an uncertainty of 5%**

**Gold:**

First of all, in order to validate the procedure, we used gold for which capture cross-section is well known. The Figure 9 shows results for 1 250 μm, 500 μm and 125 μm gold targets. A good agreement is found from 0.2 keV to 40 keV with ENDF/B-VI and JEF2.2 capture cross-section databases. However, a noticeable discrepancy is observed between 2 keV to 6 keV, which remains unexplained.

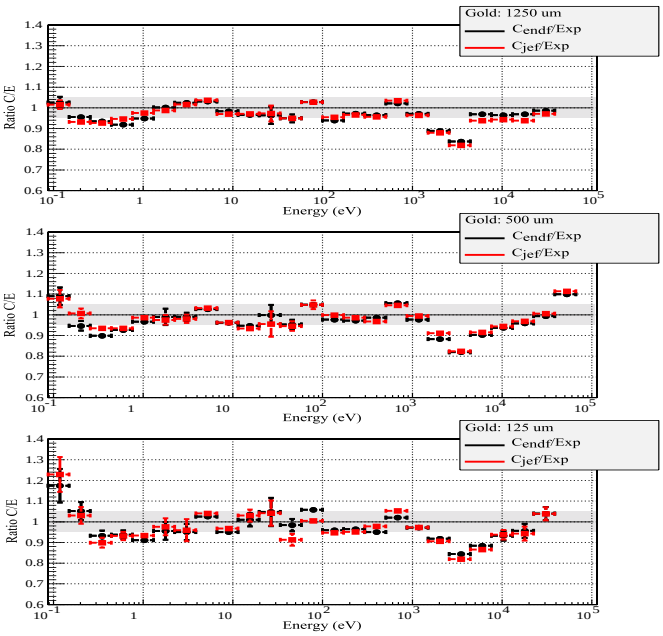


Figure 10. **ENDF/B-VI, JEF2.2 and JENDL3.2 simulation to experiment ratio for 2000 μm, 200 μm and 100 μm Tantalum samples in the energy range from 0.1 eV to 40 keV**

**Tantalum:**

In the case of 2 000 μm, 200 μm and 100 μm tantalum targets, the resolved resonance zone from 1 eV to 200 eV is correctly described. However, a deficit is observed for neutron energies lower than 1 eV for the thickest targets. A good agreement between simulation and experimental results is found with JENDL3.2 database for 300 eV<E <1 keV. In this energy range, ENDF/B-VI or JEF2.2 databases lead to a capture rate which is higher than the experimental one. This overestimation increases with the target thickness (see Figure 10). For 2 keV<E <20 keV a good agreement between experiment and simulation is found for ENDF/B-VI and JEF2.2 databases. In this energy range, the use of JENDL database produces simulated capture rates which are too low when compared to the experimental one.

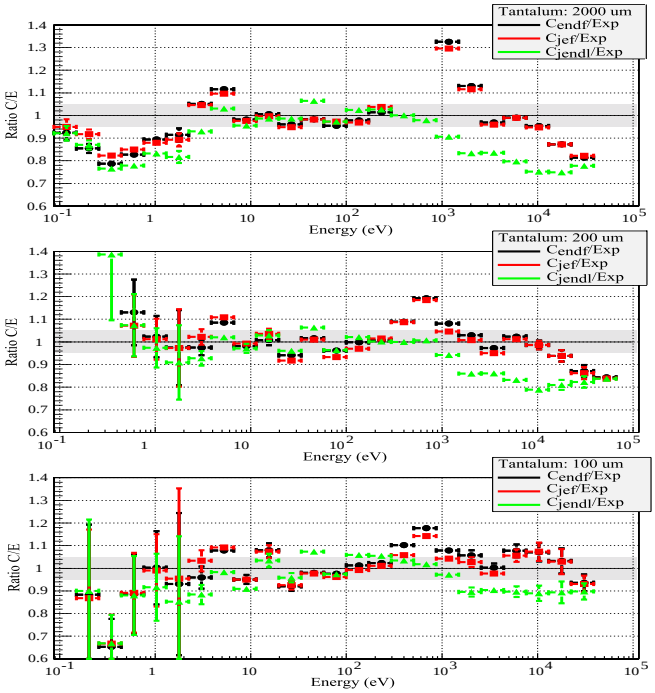

Figure 11. **ENDF/B-VI, JEF2.2 and JENDL3.2 simulation to experiment ratio for 2 000 μm, 500 μm and 300 μm indium samples in the energy range from 0.1 eV to 40 keV**

**Indium:**

In the case of 2 000 μm, 500 μm and 300 μm Indium targets, ENDF/B-VI, JEF2.2 and JENDL3.2 simulation to experiment ratio give a good agreement in the range from 0,1 eV to 1keV (see Figure 11). For 1 keV<E <40 keV, the use of ENDF/B-VI and JENDL2.2 databases leads to a capture rate which is higher than the experimental one for 2 000 μm and 500 μm thickness targets. However, the use of JEF2.2 database leads to a capture rate, which is lower than the experimental one with each target thickness.

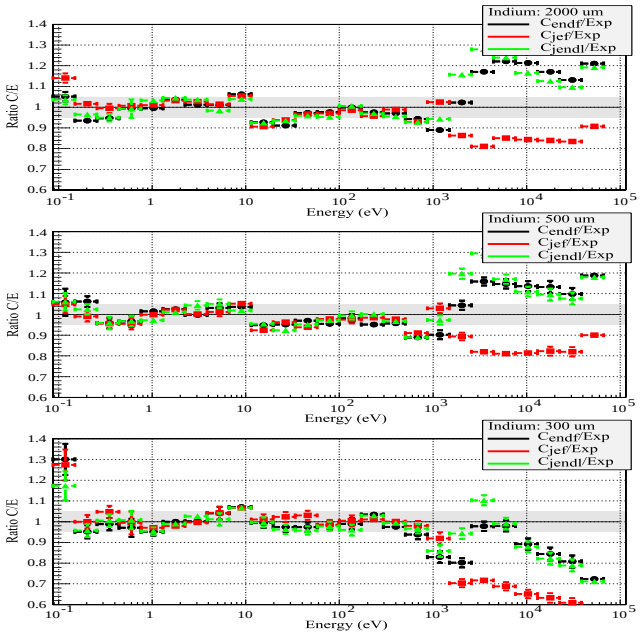


Figure 12. **ENDF/B-VI, JEF2.2 and JENDL3.2 simulation to experiment ratio for 4 000 μm, 1 000 μm and 175 μm thorium samples in the energy range from 0.1 eV to 40 keV**

**Thorium:**

In the case of 4 000 μm, 1 000 μm and 175 μm Thorium targets ENDF/B-VI, JEF2.2 simulation to experiment ratio give a good agreement (better than 5%) in the range from 10 eV to 40 keV (see Figure 12). For $E_n$<10 eV, due to the low thorium capture cross-section and the target radioactivity, the experimental rate is provided with high uncertainties. From 300 eV to 3 keV, the use of JENDL3.2 database leads to a capture rate which is lower than the experimental one with each target thickness. If we compare the results between ENDF/B-VI or JEF2.2 simulation to experiment ratio, in the unresolved resonances zone (upper than 100 eV), it shows the self-shielding effects in target good description by MCNP/4B code, well described for thickness up to 4 000 μm which is of main interest to take into account accurately these effects in reactor fuel rods.

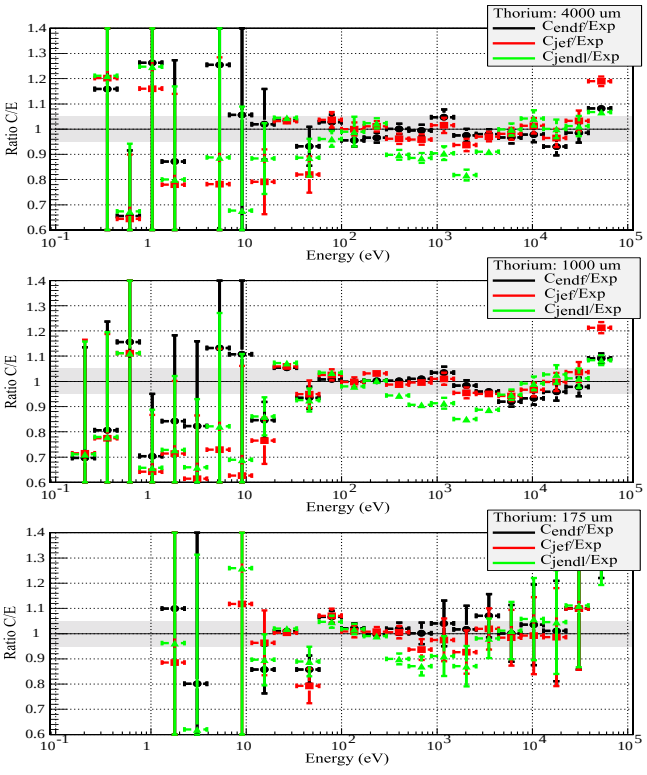

## 5. Conclusion

The neutron capture cross-section profile of various targets (Gold, Tantalum, Indium and Thorium) have been measured with a slowing down lead spectrometer in the neutron energy range from 0.1 eV to 40 keV with a precision of 5%. The experimental results are compared to Monte Carlo simulations (MCNP/4B) code using ENDF/B-VI, JEF2.2 and JENDL3.2 databases. Measurements on the well-know gold nucleus are well reproduced by simulation. The agreement with different targets thickness validates our method, and shows that the self-shielding effect is well taken into account by MCNP. For tantalum and indium targets, a discrepancy between experiment and simulation is observed for neutron energy greater than 300 eV, in the region of the unresolved resonances. For thorium targets, the JENDL3.2 cross-section seems under evaluated by 10% in the energy range from 300 eV to 3 keV.

In conclusion, the lead spectrometer appears to be a very useful tool, allowing quick cross-section validation and transmutation rates evaluation.

## REFERENCES


[1] D.Karamanis *et al., Neutron Radiative Cross-section of $^{232}$Th in the Energy Range from 0.06 to 2 MeV*, Proceedings of the 6th OECD/NEA Information Exchange Meeting on Actinide and Fission Product Partitioning and Transmutation, Madrid, Spain, 11-13 Dec. 2000, OECD Nuclear Energy Agency, Paris, France, (2001).

[2] R.E. Slovacek *et al., $^{238}$U(n,f) Measurements Blow 100 keV. Nuclear Science and Engineering*, 62 (1997) 455.

[4] European Commission, *Neutron Driven Nuclear Transmutation by Adiabatic Resonance Crossing*, TARC, Final Report, Euratom, EUR1911-EN, (1999).

[5] Philips, *Photomultiplier Tubes*, Technical report.

[6] Rene Brun and Fons Rademakers, *ROOT – An Object Oriented Data Analysis Framework*, Proceedings AIHENP'96 Workshop, Lausanne, Sept. 1996, Nucl. Inst. & Meth. in Phys. Res. A 389 (1997) 81. See also: http://root.cern.ch/.

[7] MCNP, *A General Monte Carlo Code for Neutron and Photon Transport*, J.F. Briesmester Ed., LA-12625-M, (1993).

[8] J.L. Belmont, J.M. De Conto, *L'accélérateur "GENEPI", conception, technologie, caractéristiques*, Rapport Interne ISN00.77, July 2000, ISN-CNRS, France.

# DOUBLE DIFFERENTIAL CROSS-SECTION FOR PROTONS EMITTED IN REACTIONS OF 96.5 MeV NEUTRONS ON ENRICHED $^{208}$Pb TARGETS.

**F.R. Lecolley, C. Le Brun, J.F. Lecolley, M. Louvel, N. Marie**
LPC, ISMRa et Université de Caen, CNRS/IN2P3, France

**P. Eudes, F. Haddad, M. Kerveno, T. Kirchner, C. Lebrun**
SUBATECH, Université de Nantes, France

**A. Ataç, J. Blomgren, N. Olsson**
INF, Uppsala University, Sweden

**P.U. Renberg**
TSL, Uppsala University, Sweden

**X. Ledoux, Y. Patin, P. Pras**
DPTA/SPN CEA, Bruyères-le-Châtel, France

**F. Hanappe**
ULB, Brussels, Belgium

**L. Stuttgé**
IreS Strasbourg, France

## Abstract

Transmutation techniques involve high-energy neutrons created by the proton-induced spallation of a heavy target nucleus. The existing nuclear data libraries developed for the present reactors go up to about 20 MeV, which covers all available energies for that application; but with a spallator coupled to a core, neutrons with energies up to 1-2 GeV will be present. Although a majority of the neutrons will have energies below 20 MeV, a small fraction at higher energies has still to be characterised. Above 200 MeV, direct reaction models work reasonably well, while at lower energies nuclear distortion plays a non-trivial role. This makes the 20-200 MeV region the most important for new experimental cross-section data.

Very little high-quality neutron-induced data exist in this energy domain. For (n,xp) reactions, different experimental programmes have been run at Los Alamos [7] and TRIUMF [1] facilities but with limited coverage in particle energy and angle. Better coverage has been obtain by the Louvain-la-Neuve Group up to 70 MeV [9].

Due to this particular lack of data above 70 MeV and in the framework of the European concerted action “Lead for ATD” and the HINDAS project (see J.P. Meulders contribution in these proceedings), in March’99 we performed an experiment in order to measure double differential cross-sections for protons and other light charged particles emitted in reactions of 96.5 MeV neutrons on enriched $^{208}$Pb targets, at the neutron facility of The Svedberg Laboratory (TSL), Uppsala, Sweden [2].

## 1. Experimental set-up

The charged particles (p, d, t, $^3$He and alpha) were detected using the MEDLEY device [4] which allows to measure continuous energy distributions in the forward direction (10°-80°). At larger angles, due to the relatively low intensity of the neutron beam and due to the weak estimated cross-sections, only the low-energy part of the spectra could be measured ($E_p$ < 40 MeV at θ = 160°). In order to improve the counting rate at backward angles and to measure the high-energy part of the proton spectra, we used a multi-target box together with the two arms of SCANDAL [5]. This set-up covered the angular range 10°-140°.

The MEDLEY detector set-up is installed inside a cylindrical scattering chamber of 100 cm diameter. It consists of eight detector telescopes which are mounted inside the vacuum chamber and placed every 20 degrees. They cover scattering angles ranging from 20 up to 160 degrees. In order to obtain a good separation between the different particles (p, d, t, $^3$He and alpha) over a large dynamic range, i.e. from a few MeV alpha particles up to 100 MeV protons, each telescope is composed of three detectors: two silicon surface barrier detectors and one CsI(Tl) crystal. The front detectors ($dE_1$) are either 50 or 60 mm thick, while the second ones ($dE_2$) are 400 or 500 •m. The CsI(Tl) crystal, used as E detectors, are long enough to stop 100 MeV protons. Using the well-known dE1-dE2-E method, we are able to identify with no ambiguities light charged particles.

SCANDAL, SCAttered Nucleon Detection AssembLy, is a CsI hodoscope with auxiliary detectors: drift chambers used to determine the proton trajectory and plastic scintillators used to trigger the acquisition. SCANDAL is designed for protons and neutrons in the 30-130 MeV interval.

While the proton energy threshold is around 10 MeV for MEDLEY, for SCANDAL this threshold is above 30 MeV because particles have to go through different materials before reaching the CsI(Tl) detectors.

## 2. Preliminary results and comparison with theoretical prediction

The Double Differential Cross-Section (DDCS) for protons emitted in reactions of 96.5 MeV neutrons on lead targets are presented in Figure 1.

We observe that in the energy region covered by both set-up there is a good agreement between MEDLEY and SCANDAL measurements despite a small underestimation of high energy proton production with MEDLEY at forward angles. This experimental effect is associated to the relative low thickness of the second detector which induces detection efficiency lower than 100% for the high part of the proton spectrum.

Comparisons with theoretical predictions are shown in Figures 1 and 2. A good agreement is obtained either with the GNASH-CEA [8] or the MINGUS [6] or the CUGNON [3] calculations, but there are still several problems (see Figure 3 for example with a linear y-axis) which are listed below:

- With the MINGUS calculation, the low energy part of the spectra is underestimated at forward angles and overestimated above 60 degrees.
- The GNASH-CEA calculation always underestimates the DDCS at low energies.
- The CUGNON calculation which is based on intra-nuclear cascade and optimised for incident energy above 200 MeV, works reasonably, except at low energies for the evaporative component.

## 3. Conclusion

Double differential cross-section measurements for protons emitted in reactions of 96.5 MeV neutrons on enriched lead targets were performed using the TSL facilities.

Preliminary results were compared with different theoretical calculations: they have reasonable predictions nevertheless they have to be improved in order in particular to reproduce the low energy part of the proton spectra.

This conclusion will be reinforced or cancelled

- By doing the same analysis on lead target for the other light charged particles (d, t, $^{3}$He and alpha) measured with the MEDLEY set-up.
- By studying DDCS with iron target (the dedicated experiment has been performed in May 2000 at TSL) and an uranium one (the experiment is planned in autumn 2001 at TSL).

Figure 1. **Preliminary results of double differential cross-sections for protons emitted in reactions of 96.5 MeV neutrons on enriched $^{208}$Pb**

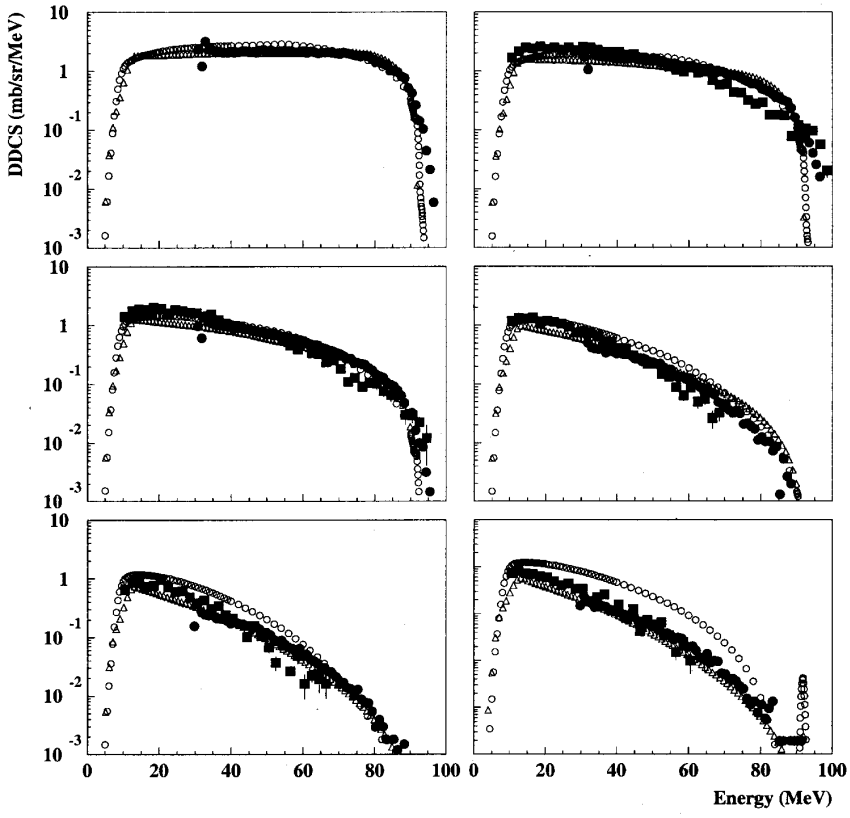


- Experimental Data : SCANDAL (black circle) and MEDLEY (black square).
- Theoretical Prediction : MINGUS (open circle) and GNASH-CEA (open triangle).
- From left to right and top to bottom, angles are ranging from 20 up to 120 degrees with 20 degrees interval.

Figure 2. **Preliminary results of double differential cross-sections for protons emitted in reactions of 96.5 MeV neutrons on enriched $^{208}$Pb**

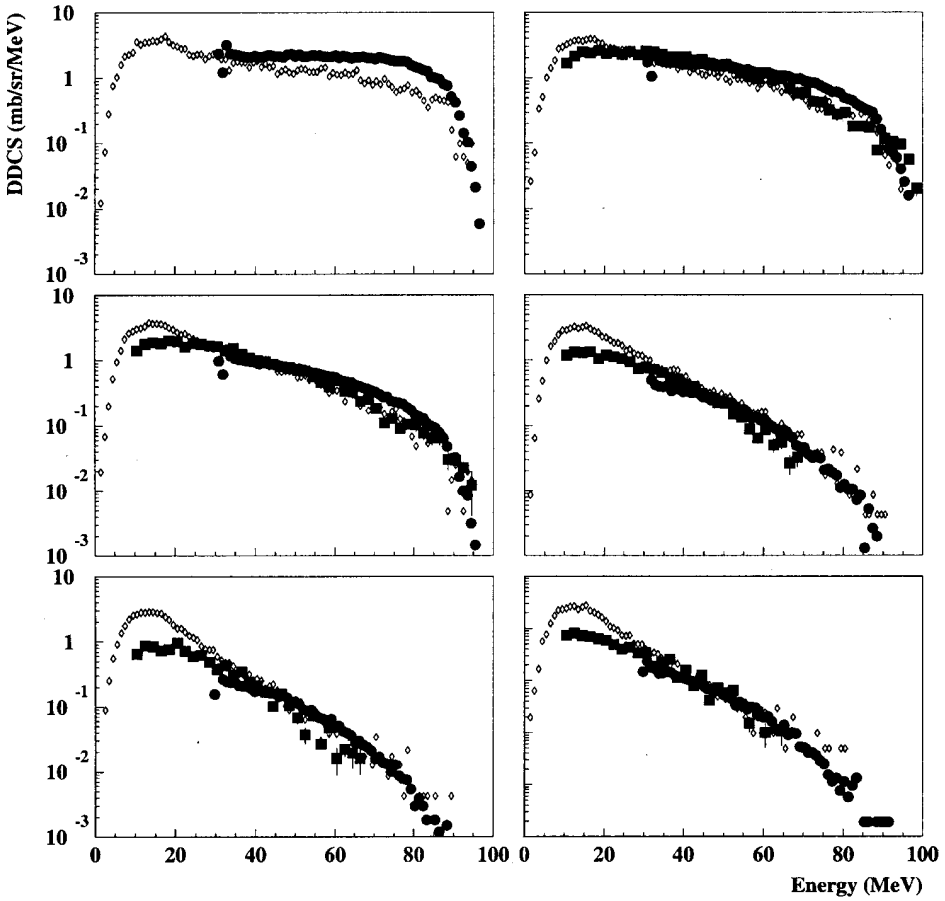


- Same as Figure 1.
- Theoretical Prediction: CUGNON (open star).

Figure 3. **Preliminary results of double differential cross-sections for protons emitted in reactions of 96.5 MeV neutrons on enriched $^{208}$Pb**

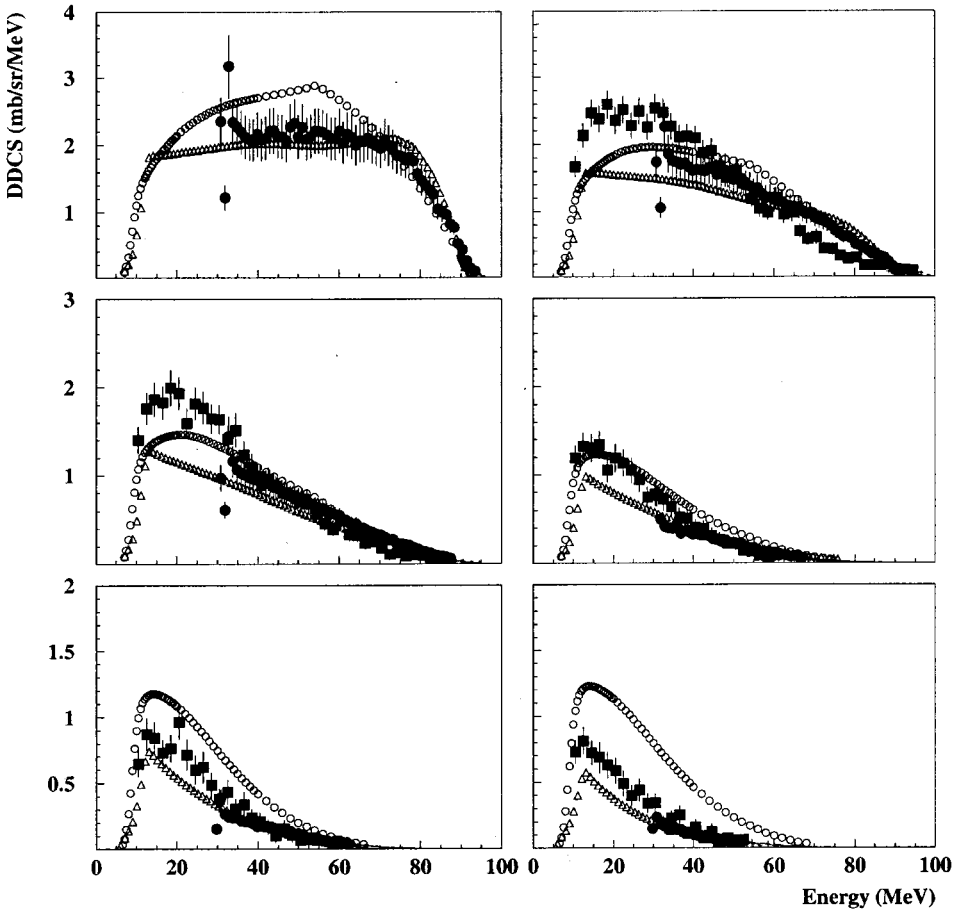


Same as Figure 1 with linear y-axis.

## REFERENCES


[1] Alford W.P. and Spicer B.M., 1998, *Nucleon Charge-exchange Reactions at Intermediate Energy*, Advances in Nuclear Physics 24, 1.

[2] Condé H. *et al.*, 1990, *A Facility for Studies Neutron Induced Reactions in the 50-200 MeV Range*, Nucl. Instr. Meth. A292, 121.

[3] Cugnon J. *et al.*, 1997, *Improved Intranuclear Cascade Model for Nucleon-nucleus Interactions*, Nucl. Phys. A, 620, 475-509.

[4] Dangtip S. *et al.*, 2000, *A Facility for Measurements of Nuclear Cross-sections for Fast Neutron Cancer Therapy*, Nucl. Instr. Meth. Phys. Res, A, 452, 484-504.

[5] Klug J. *et al.*, 2000, *SCANDAL – A Facility For Elastic Neutron Scattering Snakes in. the 50-130 MeV range*, (to be published).

[6] Koning A. *et al.*, 1997, Phys. Rev. C, V56.

[7] Rapaport J. and Sugarbaker E., 1994, *Isovector, Excitations in Nuclei*, Annu. Rev, Nucl. Part. Sci. 44, 109.

[8] Romain P. *et al.*, CEA/DAM, Private Communication.

[9] Slypen I. *et al.*, 1994, *Charged Particles Produced in Fast Neutron Induced Reactions on 12C in the 45-80 MeV Energy Range*, Nucl. Instr. Meth., A337, 431.

# MEASUREMENTS OF PARTICULE EMISSION SPECTRA IN PROTON INDUCED REACTIONS OF INTEREST FOR THE DEVELOPMENT OF ACCELERATOR DRIVEN SYSTEMS

**N. Marie, C. Le Brun, F.R. Lecolley, J.F. Lecolley, F. Lefèbres, M. Louvel, C. Varignon**
LPC de Caen, Université de Caen, IN2P3-CNRS/ISMRA – France

**Ph. Eudes, S. Auduc, F. Haddad, T. Kirchner, C. Lebrun**
SUBATECH, Université de Nantes, IN2P3-CNRS, École des Mines de Nantes, France

**Th. Delbar, A. Ninane**
Institut de Physique Nucléaire, Belgium

**F. Hanappe**
FNRS et Université Libre de Bruxelles, Belgium

**X. Ledoux, Y. Patin, Ph. Pras**
DPTA/SPN, CEA, France

**L. Stuttge**
IreS, IN2P3-CNRS, Strasbourg, France

**Abstract**

In the framework of the concerted action “Lead for ADS” program, we have measured the double differential cross-sections of neutrons produced in reactions induced by a proton beam on a lead target at 62.5 MeV. The experiment was performed on the S-line of the CYCLONE facility in Louvain-la-Neuve. The neutrons were detected using DEMON counters and their energy was derived from the time-of-flight technique.

## 1. Introduction

For many accelerator driven system projects [1,2], lead has been chosen as a representative spallation target material. Therefore, Pb (p, X n), Pb (p, X p), Pb (p, X lcp) double differential cross-sections (DDCS) are required with high priority for the development of simulation codes. These codes are used for feasibility studies and optimisation of such hybrid systems in which complex combinations of nuclear processes are involved. Combined with complementary Pb (n, X n), Pb (n, X p), Pb (n, X lcp) DDCS, these data represent the best test for evaluating the global capabilities of the models. In addition, such data provide important constraints which allow the predictive power of the codes to be improved in the 20-150 MeV energy range.

In this context and in the framework of the Concerted Action "Lead for ADS" programme, we measure the DDCS of neutrons and light charged particles (p, d, t, $^{3}$He, $^{4}$He) produced in reactions induced by a proton beam, impinging on a lead target at 62.5 MeV. In this contribution we present results concerning only the neutrons.

Figure 1. **Simulation with GEANT of the experimental set-up geometry (see text)**

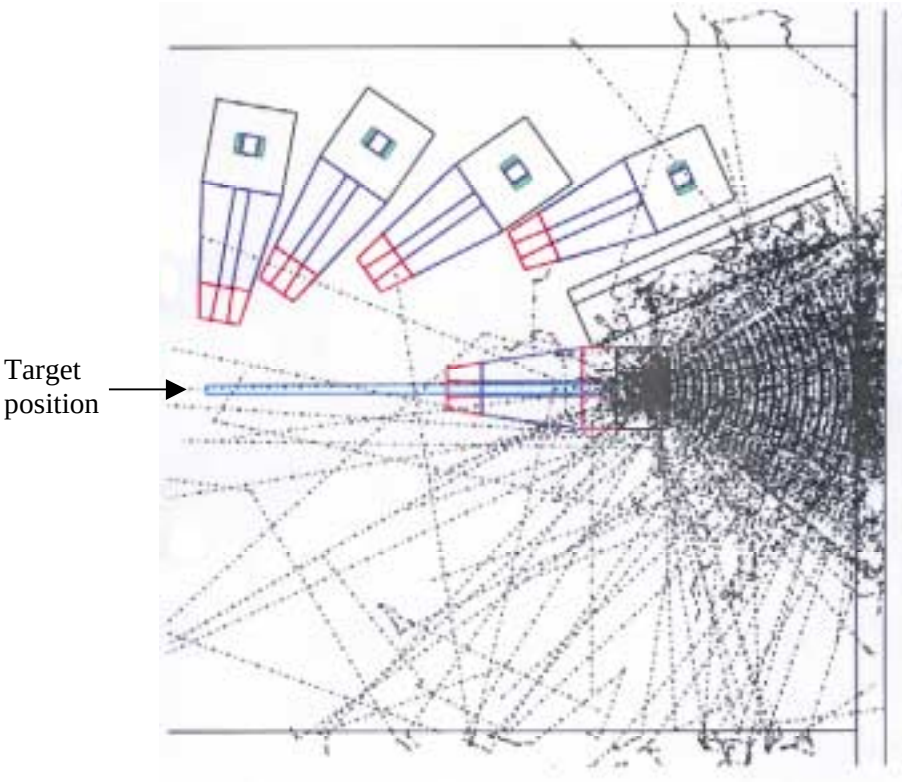

## 2. Experimental set-up

The experiment was performed on the S-line of the CYCLONE facility in Louvain-la-Neuve. The lead target is 10.7 mg/cm$^2$ thick and the neutrons are detected using five DEMON large volume NE213 liquid scintillator counters [3]. The following table gives, for each counter, its angle theta relative to the beam and the distance between the target and its entrance window.

| DEMON counter | theta (°) | d (mm) |
|---|---|---|
| 1 | 120 | 2 960 |
| 2 | 80 | 2 507 |
| 3 | 55 | 3 039 |
| 4 | 35 | 3 887 |
| 5 | 24 | 5 347 |

Each detector is surrounded by a lead cylinder installed inside a "BOMBARDE" barrel filled with paraffin and boron - materials that are efficient shields against background neutrons.

Figure 2. **Compilation of the measured DEMON detector efficiencies (symbols) compared to the predictions of the KSU code (black line)**

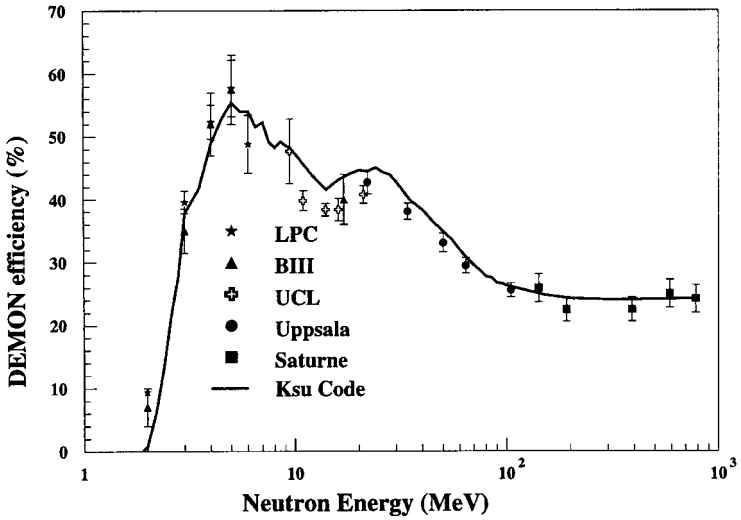


Due to the necessity of shielding the DEMON counters from the very high radiation background resulting from the proton beam dump, a wall made of concrete and paraffin is also built in the experimental area. Taking into account the experiment configuration (various materials and dimensions), the floor-space and the weight of concrete blocks, the wall dimensions is optimised performing GEANT simulations. The final wall geometry divides by a factor of twenty the background of the most exposed DEMON counter to the parasite neutron flux, resulting in a signal-to-noise ratio of 2.1. The Figure 1 illustrates the efficiency of the shielding wall. It presents part of the geometry of the experimental set-up: the faraday cup placed at the end of the beam line and four DEMON counters imbedded in BOMBARDE barrels, and the shielding wall built between the forward DEMON counter and the beam dump. Dashed lines symbolise neutrons escaping from the

beam dump. We observe that the majority of the neutrons emitted in the direction of the counters are stopped by the wall or deviated in their trajectories.

## 3. Data analysis

We discriminate neutrons from gammas by pulse shape analysis of the photomultiplier output. For each neutron, the time-of-flight is derived from the start given by the DEMON counter, and the stop given by the following beam high frequency signal (period = 54 ns). The same procedure is employed for gammas so that the time-of-flight spectra are calibrated with the reference peaks associated to gammas. In order to detect without ambiguity the lowest energy neutrons, nine beam bursts out of ten are suppressed. Neutron energies are derived from their time-of-flight, taking into account the depth at which the particle interacts inside the detector. This depth is estimated using an iterative procedure since it depends on the detection efficiency, which is itself a function of the neutron energy. The DEMON detector efficiency can be found in [4] and it is shown in Figure 2.

During the experiment, attention was paid to alternatively collect data with Pb targets and with blank-targets in order to be able to subtract the background noise. The acquisition dead time is also kept under twenty percent and a correction for this effect is applied to the data. For the cross-section calculation, the number of incident protons is derived from the intensity of the beam measured using the faraday cup. The detector efficiency and solid angle, as well as the orientation of the target are also taken into account in deriving the absolute normalisation factor.

Figure 3. **Double differential cross-section of neutrons produced in reactions induced by a proton beam impinging on a lead target at 62.5 MeV**

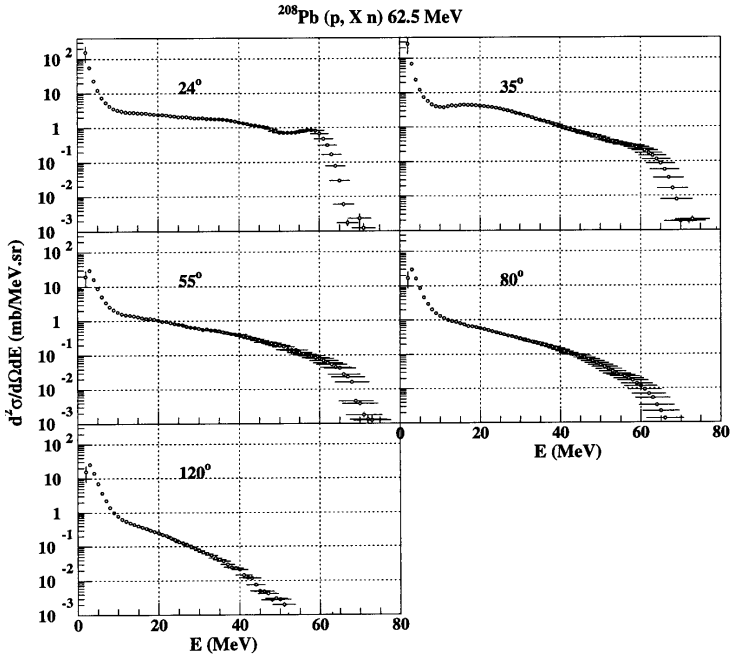

## 4. Results

Figure 3 presents neutron energy spectra obtained at five different angles. The energy uncertainty is derived from the length uncertainty of the time-of-flight path (±1 mm), combined with the uncertainty on the depth at which the neutron interacts inside the scintillator (±1 cm) and the electronic chain resolution. The resulting energy uncertainty increases smoothly with the neutron energy from 0.03 MeV to 4.2 MeV at 62.0 MeV. In order to calculate the cross-section uncertainty, we take into account the detector efficiency uncertainty which is lower than 5.8% over the entire energy range. The contribution of the statistical uncertainty to the relative total uncertainty is estimated to be lower than 2% for energies smaller than 30 MeV, it increases up to 4.4% for an energy value of 60 MeV at a detection angle of 80°, and it reaches a maximum value of 16% at the most backward angle, for the larger energy. Those values result in a total relative uncertainty of the cross-section lower than 5.6% for energies smaller than 30 MeV, it increases up to 6.5% for an energy value of 60 MeV at a detection angle of 80°, and it reaches a maximum value of 17% at the most backward angle and for the larger energy. Due to the logarithmic representation the associated error bars are not visible on the figure.

## 5. Conclusion

We present neutron double differential cross-sections measured at five different angles for the Pb(p, X n) reaction, at 62.5 MeV. These results will contribute to the extension up to 150 MeV of evaluated nuclear data libraries, which are a combination of experimental and calculated data. Such a database is planned to be implemented in different simulation codes which are used for the conception of the future hybrid systems.

## REFERENCES


[1] C.D. Bowman *et al.*, Nucl. Instr. Meth. A320 (1992)336.

[2] C. Rubbia *et al.*, preprint CERN/AT/95-44/ET (1995).

[3] I. Tilquin *et al.*, Nucl. Instr. Meth. A365(1995)446.

[4] C. Varignon, Thèse de Docteur en Physique Nucléaire, soutenance déc. 99.

# INTERMEDIATE ENERGY NEUTRON-INDUCED FISSION CROSS-SECTIONS FOR PROSPECTIVE NEUTRON PRODUCTION TARGET IN ADS

**V.P. Eismont, I.V. Ryzhov, A.N. Smirnov, G.A. Tutin**
V.G. Khlopin Radium Institute, 2oi Murinskiy Prospect 28, Saint-Petersburg 194021, Russia

**H. Condé, N. Olsson, A.V. Prokofiev***
Department of Neutron Research, Angström Laboratory, Uppsala University,
Box 525, S-751 20 Uppsala, Sweden

## Abstract

Up-to-date status is considered of the experimental database on neutron-induced fission cross-sections of tantalum, tungsten, lead, mercury, gold, and bismuth nuclei in the neutron energy range from the fission threshold to 175 MeV. The perspective of creating a more complete database is discussed, including (n,f) cross-sections for separated isotopes of lead and tungsten.

* On leave from V.G. Khlopin Radium Institute, St. Petersburg, Russia.

## 1. Introduction

Intermediate-energy fission data are of interest not only for fundamental physics, but also for applied nuclear research. First of all it is connected with problems of accelerator driven systems (ADS) for power production and transmutation of long-lived radioactive waste (see e.g. [1]). Such elements as Ta, W, Hg, Pb and Bi are either already used as neutron producing target materials or considered as potential candidates. Since fission and spallation reactions at intermediate energies are the main reaction channels of neutron interactions with heavy nuclei, they have the most practical significance, but are poorly investigated. Fission reaction contributes to the generation of the neutron field in the target-blanket assembly, as well as to the production of radionuclides and chemically toxic products in the target. For relatively light nuclei, such as Pb and Bi with fission cross-section of only a few percent of the total reaction cross-section, the residual activity of the fission products with high energy release and, often, long half-lives, is expected to be significant. It is estimated that the contribution of the fission products to the overall residual activity of a lead target irradiated by 1.6-GeV protons may be as much as 10-15% for cooling times of about one year [2]. At present, theoretical description of sub-actinide nuclei fission cannot match the practical needs. For example, the $^{nat}$W(p,f) cross-section predicted by the LAHET code was found to be about 20 times lower than the experimental results [3]. If one bears in mind the insufficient predictive power of available nuclear reaction models, especially with respect to fission, it is possible that the real residual activity may be significantly different.

Intermediate-energy fission data are also of interest for nuclear standards, and particle beam monitoring required for other applications as neutron cancer therapy, shielding of accelerators, cosmic studies, thermonuclear synthesis etc. Furthermore, due to the insensitivity to low energy neutrons, the $^{209}$Bi(n,f) cross-section has been approved by IAEA as a secondary standard for neutron flux determination at intermediate energies [4].

As a response to the outlined needs, V.G. Khlopin Radium Institute and Uppsala University perform a joint program of (n,f) cross-section measurements for sub-actinides in the energy region between 20 and 180 MeV. Earlier, results for the absolute and relative (n,f) cross-sections of $^{238}$U, $^{209}$Bi and $^{208}$Pb have been published [5-7]. In the framework of ISTC project #540 the measurements for $^{208}$Pb and $^{209}$Bi were continued with better experimental conditions, including new measurements on $^{181}$Ta, $^{nat}$W, $^{nat}$Hg, $^{197}$Au and $^{nat}$Pb. The measurements on gold were included because of their methodical and theoretical importance. Preliminary results for the above listed sub-actinides have been published recently [8-11]. In the present work the results of further processing of the data are given and the status of the $^{209}$Bi (n,f) cross-section standard is discussed.

The prospects for creating of more complete database are considered, including (n,f) cross-sections for separated isotopes of lead and tungsten, specifically for $^{208}$Pb and $^{184}$W , which cross-sections are included in the High Priority Request List of nuclear data for the nucleon energy region up to 200 MeV [12]. These data are needed for the development of adequate nuclear fission models, as well as computer codes for ADS. The needs of fission cross-section measurements for the above mentioned nuclides are stressed, not only with neutrons, but also with protons, in the same projectile energy region. Comparison of proton- and neutron-induced fission cross-sections [13], carried out on a common physical basis [14], gives added credence to the experimental database.

## 2. Up-to-date status of the (n,f) cross-sections of sub-actinides

The (n,f) cross-sections of $^{181}$Ta, $^{nat}$W, $^{nat}$Hg, $^{197}$Au, $^{208}$Pb and $^{nat}$Pb published in [9-11] have been obtained with the assumption that the fraction of the total fission events induced by full energy neutrons is equal for the studied nuclides and for the monitor reaction $^{209}$Bi(n,f). In this work we have calculated the fraction of the total fission events induced by full energy neutrons for each reaction under study. For this purpose the TOF spectra of fission events have been simulated using the experimental neutron spectra [15-19] and the given time parameters of the proton beam. The final cross-sections and the fractions of the full energy fission events have been obtained as a result of an iteration procedure with the initial cross-sections taken from [4,9]. The results of the calculations carried out for the $^{209}$Bi(n,f) and $^{nat}$W(n,f) reactions at a peak neutron energy of 96 MeV are shown in Figure 1 together with the neutron spectrum from the $^{7}$Li(p,n) reaction measured by Nakao *et al*. [15] at the similar incident proton energy.

Figure 1. **(a) Neutron spectrum from $^{7}$Li(p,n) reaction at 100 MeV proton energy [15]; (b) and (c) TOF spectra of $^{209}$Bi(n,f) fission events at 12.8 m and 2 m flight distances, correspondingly; (d) TOF spectrum of $^{nat}$W(n,f) fission events at 2 m flight distance. Open dots in (b), (c), and (d) are experimental TOF spectra. Solid curves are calculated TOF spectra. Filled areas under dashed curves are calculated fractions of fissions induced by low energy tail neutrons.**

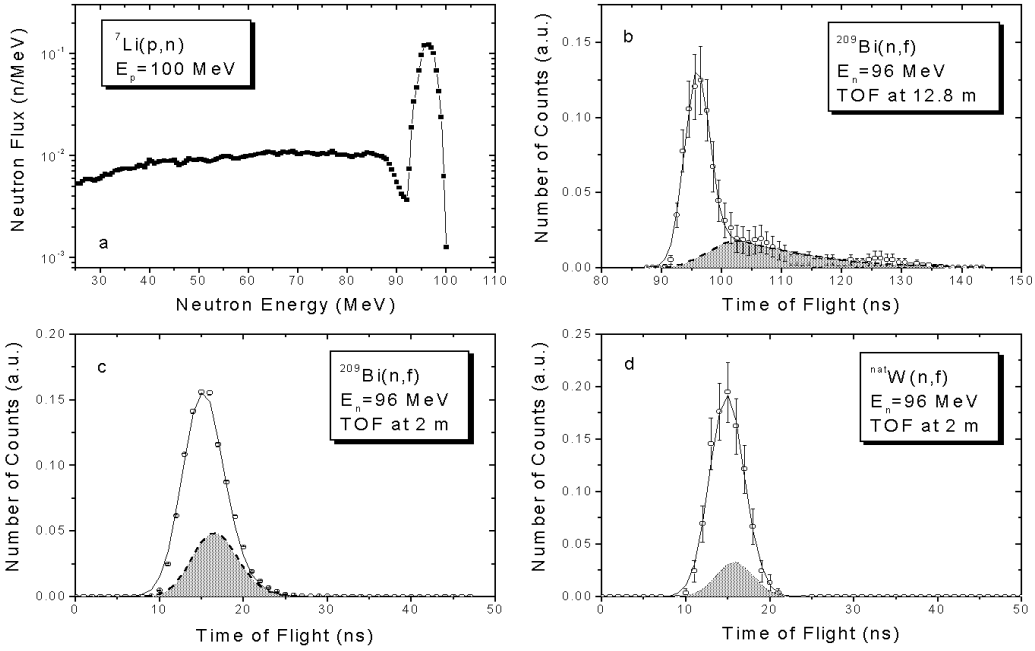


The results for (n,f) cross-section ratios are given in Table 1. The absolute (n,f) cross-sections obtained using the $^{209}$Bi(n,f) cross-section as a standard [4] are shown in Figure 2 together with fits according to Equations 1) and 2) below and our previously reported data for $^{208}$Pb [6].

Table 1. **Relative neutron-induced cross-sections**

| $E_n$ | **(n.f) cross-section ratio** | | | | | |
|---|---|---|---|---|---|---|
| MeV | $^{nat}Pb/^{209}Bi$ | $^{208}Pb/^{209}Bi$ | $^{nat}Hg/^{209}Bi$ | $^{197}Au/^{209}Bi$ | $^{nat}W/^{209}Bi$ | $^{181}Ta/^{209}Bi$ |
| 35 | 0.166 ± 0.079 | <0.051 | – | <0.012 | – | – |
| 45 | 0.191 ± 0.012 | 0.069 ± 0.005 | <0.036 | 0.048 ± 0.013 | – | – |
| 66 | 0.292 ± 0.026 | 0.185 ± 0.017 | 0.127 ± 0.026 | 0.099 ± 0.017 | <0.0017 | – |
| 75 | 0.305 ± 0.026 | 0.205 ± 0.019 | 0.099 ± 0.021 | 0.099 ± 0.010 | 0.0040 ± 0.0007 | 0.0013 ± 0.0004 |
| 94 | 0.379 ± 0.031 | 0.288 ± 0.026 | 0.158 ± 0.017 | 0.139 ± 0.017 | 0.0075 ± 0.0014 | 0.0036 ± 0.0006 |
| 96 | 0.391 ± 0.036 | 0.305 ± 0.028 | – | – | 0.0089 ± 0.0022 | 0.0037 ± 0.0012 |
| 133 | 0.429 ± 0.037 | 0.305 ± 0.029 | 0.199 ± 0.019 | 0.184 ± 0.022 | 0.0134 ± 0.0026 | 0.0071 ± 0.0014 |
| 144 | 0.505 ± 0.045 | 0.418 ± 0.037 | 0.158 ± 0.019 | 0.205 ± 0.025 | 0.0140 ± 0.0025 | 0.0101 ± 0.0017 |
| 160 | 0.422 ± 0.062 | – | – | – | – | – |
| 174 | 0.526 ± 0.042 | 0.412 ± 0.034 | 0.215 ± 0.040 | 0.211 ± 0.020 | 0.0210 ± 0.0027 | 0.0096 ± 0.0013 |

Figure 2 shows also the earlier data of other authors [20-22]. In order to make a comparison for available absolute $^{197}Au$ and $^{nat}Pb(n,f)$ cross-sections, the $^{nat}Pb/^{235}U$ and $^{197}Au/^{235}U$ ratios measured at LANSCE [20] were multiplied by the standard $^{235}U(n,f)$ cross-section [4]. Early measurements of Reut *et al.*, Goldanskiy *et al.*, and Dzhelepov *et al.*, [21] were made using neutrons from the Cu(d,n) reaction. Neutrons produced by that reaction have a broader spectrum, as indicated by the horizontal error bars in Figure 2. Nevertheless, there is a qualitative agreement between those and more recent data. Vorotnikov [22] performed unique studies of (n,f) cross-sections for sub-actinides in the vicinity of the fission barrier (about 20-25 MeV) using a deuterium-tritium neutron source and solid state nuclear track detectors for the fission fragment detection.

Figure 2. **The $^{181}$Ta(n,f), $^{nat}$W(n,f), $^{nat}$Hg(n,f), $^{197}$Au(n,f), $^{208}$Pb(n,f) and $^{nat}$Pb(n,f) cross-sections. Solid and dashed curves are the fits made with the use the formulae 1, 2 (see the text below)**

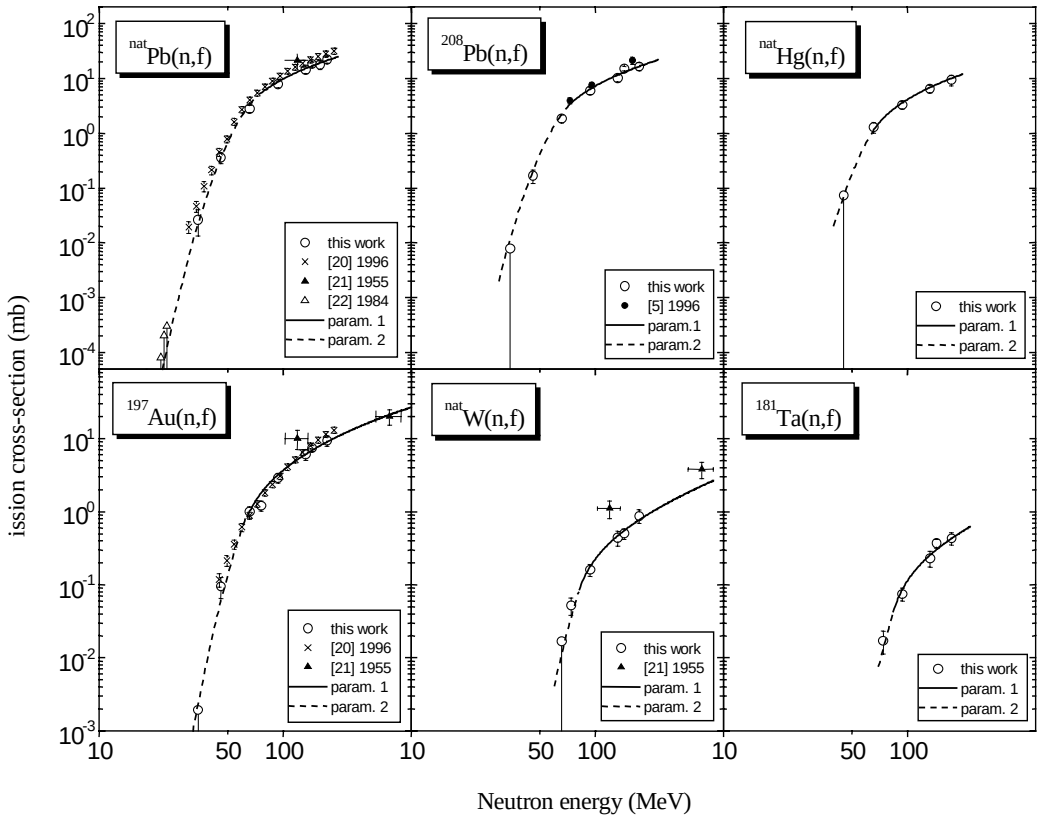


The available experimental data on the $^{nat}$Pb(n,f) and $^{197}$Au(n,f) cross-sections [20] and the data of the present work are in qualitative agreement. There are, however, systematic discrepancies between these data sets in the neutron energy regions below about 50 MeV and above about 100 MeV for $^{197}$Au(n,f) and practically in the whole energy region for $^{nat}$Pb(n,f). This fact, together with the comparison for $^{197}$Au/$^{209}$Bi and $^{nat}$Pb/$^{209}$Bi cross-section ratios performed in [10], leads to a suggestion that some background may not have been taken fully into account in the LANSCE measurements of the $^{nat}$Pb(n,f) and $^{197}$Au(n,f) cross-sections. The low-energy $^{nat}$Pb(n,f) data of the present work are compatible with the upper limits of the cross-section obtained by Vorotnikov [22]. The old data of Reut *et al.*, Goldanskiy *et al.*, and Dzhelepov *et al.*, [21] for $^{nat}$Pb(n,f), $^{197}$Au(n,f), and $^{nat}$W(n,f) cross-sections at a neutron energy of 120 MeV are considerably (two-three times) higher than our data in the same energy region.

The fits in Figure 2 were made using the same formulae that have been used for parameterization of the $^{209}$Bi(n,f) cross-section [4]:

$$\sigma_{nf} = p_{11} \cdot (1 - \exp(p_{12} \cdot (E_n - p_{13}))) \tag{1}$$

above about 70 MeV [23], and

$$\sigma_{nf} = \exp(p_{21} + p_{22} \cdot \ln E_n + p_{23} \cdot \ln^2 E_n) \tag{2}$$

below about 70 MeV [24] , where $\sigma_{nf}$ is the (n,f) fission cross-section (mb), $E_n$ is the neutron energy (MeV) and $p_{ij}$ are variable parameters. The parameters $p_{ii}$ as functions of the parameter $Z^2/A$ of the compound nuclei are available upon request.

Taking into account the uncertainties coming from the experimental technique and the cross-section standard we can state that the accuracy of the presented data is about 20% for most nuclei in the energy range above 75 MeV and 30-50% below 75 MeV. As the neutron energy and the target atomic number are decreased, the uncertainty is increased.

Figure 3. **Experimental data on the $^{209}$Bi(n,f) cross-sections**

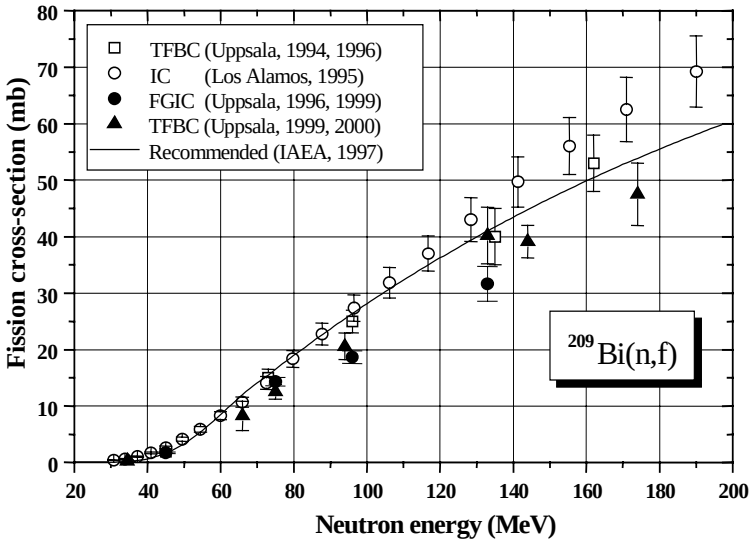


As it was mentioned above, the present status of the experimental data on the $^{209}$Bi(n,f) cross-section is of particular interest, because it is a new standard in the energy region above 50 MeV. All experimental data available in the energy range of interest are given in Figure 3 along with the $^{209}$Bi(n,f) cross-section parameterization from [4]. It is obvious that there is a discrepancy between the recommended parameterization and some experimental results published more recently [8,9]. Specifically, our data obtained at the neutron energies 96 MeV and 133 MeV (solid circles) are systematically lower than the recommended curve and do not fall into the confidence interval (10%) stated in [4]. To understand whether (or not) this discrepancy will eventually result in a recommendation to change the standard, a closer look at the quality of the experimental data must first be undertaken. The data under consideration have been obtained with the use of three fission fragment detectors: thin-film breakdown counters (TFBC), a conventional parallel plate ionization chamber (IC), and a Frisch-gridded ionization chamber (FGIC).

The TFBCs are insensitive to the background radiation and offer excellent timing characteristics [25]. Previous data obtained with the use of the TFBC [5,6] and the FGIC [7], together with earlier data [21,22] have been used as a basis for the parameterization, recommended as a standard [4]. However, recently it was found out that the decomposition procedures applied in [5,6,11] to the TOF spectra of fission events lacked accuracy at some neutron energy points. We suppose, that a more sophisticated background approximation (see e.g. [7]) has to be used to extract from TOF spectra a number of fission events induced by “peak” neutrons. Solid triangles in Figure 3 show our data from [9,11] corrected due to a more accurate decomposition procedure as well as data

obtained more recently. It is seen that these data deviate systematically from the parameterization [4] and become closer to our data obtained with the FGIC [8,9].

An ionization chamber (IC) is ideally suitable for (n,f) cross-section measurements at the currently available high-energy neutron beams, because this device offers nearly 100% detection efficiency with no limitations on the fissile target dimensions. It should be noted, however, that the energy spectrum of fission fragments is contaminated by light charged particles arising in upstream material from energetic neutrons. This background makes the determination of the fission fragment yield difficult. As the incident neutron energy increases, the situation becomes more complicated (particularly for sub-actinides) due to larger overlap between fission and background spectra. We suppose that data obtained with the simple ionization chamber [20] may be subject, especially at high neutron energies, to some systematic errors caused by the background problems.

The FGIC not only incorporates the main advantages of conventional parallel plate ionization chambers, but also offers some extra ones for (n,f) cross-section measurements. The key advantage is that FGIC allows discrimination against background charged particles [8]. The principle of so called angular discrimination lies in the fact that fission fragments and light charged particles give different combinations of anode and grid signals, and thus may be separated from each other by off-line processing. Taking also into account that an accurate decomposition procedure has been applied to the TOF spectra in [8,9], we consider the data obtained with the FGIC as the most reliable at present.

All aforesaid gives some grounds to expect changes of the standard in the future, but in the present work all data on (n,f) cross-sections for sub-actinides are given relative to the old standard.

## 3. Prospects for advancement of the existing experimental data base

Further development of the experimental techniques is needed to improve the quality of the data. This refers both to the characteristics of neutron beam and to the fission fragment detectors.

To increase the number of fissile targets to be irradiated simultaneously, the new FGIC has been designed and manufactured at the KRI within the framework of ISTC project #1309. The chamber consists of seven units. Each unit constitutes a twin Frisch-gridded ionization chamber with a common cathode. By this means 14 different targets may be irradiated simultaneously.

Due to the insensitivity of TFBCs to light ionizing particles it is possible to carry out the (p,f) and (n,f) cross-section measurements under comparable geometrical conditions. Experiments can be done with a broad proton beam passing through the target and the TFBC [26]. This makes it possible to reduce the uncertainty in the comparison analysis of data on the proton and neutron-induced fission cross-sections.

Combined analysis of (n,f) and (p,f) cross-sections is of special interest for studies of the fission process. The quantitative comparison of these cross-sections carried out in [13] revealed the following empirical dependence of the cross-section ratios on the $Z^2/A$ parameter of the target nucleus:

$$\sigma_{pf}/\sigma_{nf} = \exp [k(37- Z^2/A)] \quad (3)$$

where k is a function of energy ($k>0$ for $Z^2/A\leq37$, and $k = 0$ for $Z^2/A>37$). This dependence was explained in terms of the fissility of the nucleus ($P_f = \sigma_{pf}/\sigma_{in}$) which is defined by the fission and evaporation widths: $P_f = \Gamma_f/\Gamma_f + \Gamma_n + \ldots$

Since for sub-actinides $\Gamma_f/\Gamma_n << 1$, one can obtain that:

$$P_f \cong \exp(-(B_f\,(Z^2/A) - B_n)/\,T\,), \tag{4}$$

where $B_f$ and $B_n$ are the fission barrier and the neutron binding energy, respectively, and T is the nuclear temperature. For $P_{pf} = P_{nf}$ it is easy to verify that:

$$\sigma_{pf}\,(Z,A,E_p) = (\sigma_{in})_p/(\sigma_{in})_n\;\sigma_{nf}\,(Z+1,A,E_p), \tag{5}$$

provided that $E_p = E_n + B_n - B_p$ . This relation is clearly seen in Figure 4, where both cross-sections are given (at 150 MeV) as functions of the $Z^2/A$ parameter of the compound nucleus. One can see that all points follow a straight line giving added credence to the experimental data.

Figure 4. **The (p,f) and (n,f) cross-sections of sub-actinides nuclei vs $Z^2/A$ parameter of compound nucleus**

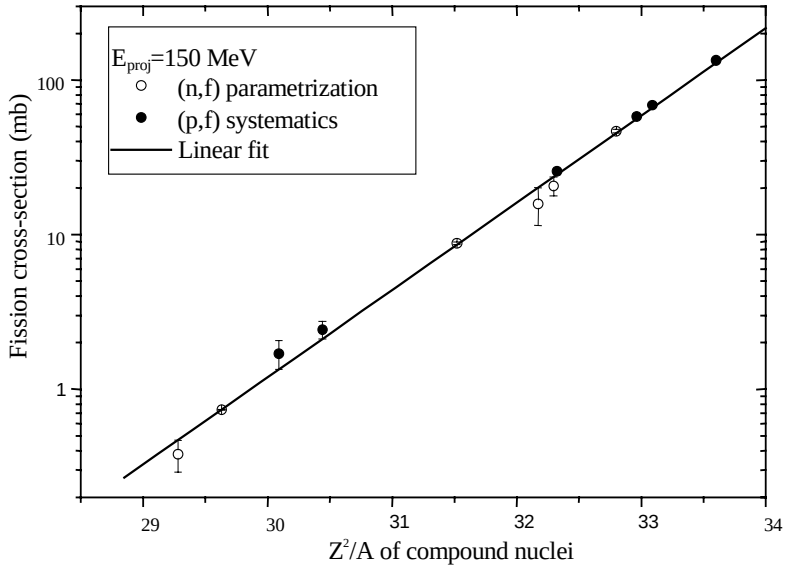

## REFERENCES


[1] C. Rubbia, *The Energy Amplifier: a Solid-phase, Accelerator Driven, Sub-critical Th/233U Breeder for Nuclear Energy Production with Minimal Actinide Waste*. Proc. Int. Conf. on Nuclear Data for Science and Technology, Gatlinburg, 1994, ed. J.K. Dickens, ORNL, USA, Vol. 2, pp. 1065-1071.

[2] Yu.N. Shubin, A.V. Ignatyuk, A.Yu. Konobeev, V.P. Lunev, and E.V. Kulikov, *The Analysis of Energy Release, Beam Attenuation, Radiation Damage, Gas Production and Accumulation of Long-lived Activity in Pb and Pb-Bi Targets*, Proc 2nd Conf. on ADTT, Kalmar, Sweden, June 3-7, 1996, ed. H. Condé: Uppsala University, 1997, Vol. 2, pp. 953-959.

[3] M.C. Duijvestijn, A.J. Koning, J.P.M. Beijers, A. Ferrari, M. Gastal, J. van Klinken, R.W. Ostendorf. *Proton-induced Fission at 190 MeV of $^{nat}W$, $^{197}Au$, $^{nat}Pb$, $^{208}Pb$, and $^{232}Th$.* Phys. Rev. C**59**, 776 (1999).

[4] A.D. Carlson, S. Chiba, F.-J. Hambsch, N. Olsson, A.N. Smirnov, *Update to Nuclear Data Standards for Nuclear Measurements*, IAEA Report INDC(NDS)-368, Vienna, 1997, Proc. Int. Conf. on Nuclear Data for Science and Technology, Trieste, Italy, May 19-24, 1997, Part II, p. 1223.

[5] V.P. Eismont, A.V. Prokofiev, A.N. Smirnov, K. Elmgren, J. Blomgren, H. Condé, J. Nilsson, N. Olsson, T. Rönnqvist, and E. Traneus, *Relative and Absolute Neutron-induced Fission Cross-sections of $^{208}Pb$, $^{209}Bi$ and $^{238}U$ in the Intermediate Energy Region*, Phys. Rev. C**53**, 2911 (1996).

[6] V.P. Eismont, A.V. Prokofiev, A.N. Smirnov, J. Blomgren, H. Condé, K. Elmgren, J. Nilsson, N. Olsson, and E. Ramström, *Measurements of Neutron-induced Fission Cross-sections of Heavy Nuclei in the Intermediate Energy Region*, Proc. 2nd Int. Conf. on ADTTA, Kalmar, Sweden, June 3-7, 1996, ed. H. Condé: Uppsala University, 1997, Vol. 2, pp. 606-612.

[7] V.P. Eismont, A.V. Kireev, I.V. Ryzhov, G.A. Tutin, H. Condé, K. Elmgren and S. Hultqvist, *Measurement of the Neutron-induced Fission Cross-sections of $^{209}Bi$ at 45 and 73 MeV*, Proc. 2nd Int. Conf. on ADTTA, June 3-7, 1996, Kalmar, Sweden, ed. Henri Condé: Uppsala University, 1997, Vol. 2, pp. 618-623.

[8] V.P. Eismont, A.V. Kireev, I.V. Ryzhov, S.M. Soloviev, G.A. Tutin, H. Condé, K. Elmgren, N. Olsson, and P.-U. Renberg, *Neutron-induced Fission Cross-section Ratios of $^{209}Bi$ to $^{238}U$ at 75 and 96 MeV*, The 3rd International Conference on Accelerator Driven Transmutation Technologies and Applications, Praha, Czech Republic, 1999, (available as CD-ROM, paper Mo-O-C7).

[9] V.P. Eismont, *Measurements of Neutron Induced Fission Cross-sections in Energy Region $15<E_n<160$ MeV for Basic and Applied Researches,* Final Project Technical Report of ISTC 540-97.

[10] V.P. Eismont, A.V. Prokofiev, A.N. Smirnov, S.M. Soloviev, H. Condé, K. Elmgren, and N. Olsson, *Neutron-induced Fission Cross-sections of $^{nat}$Pb and $^{197}$Au in the 35-180 MeV Energy Region,* Proc. 3rd International Conference on Accelerator Driven Transmutation Technologies and Applications, Praha (Pruhonice), Czech Republic, June 7-11, 1999 (available as CD-ROM, paper Mo-O-C8).

[11] V.P. Eismont, A.V. Prokofiev, A.N. Smirnov, H. Condé, K. Elmgren, N. Olsson, P.-U. Renberg, *Neutron-induced Fission Cross-sections of $^{181}$Ta, $^{nat}$W, $^{197}$Au, $^{nat}$Hg, $^{197}$Au, $^{208}$Pb, $^{nat}$Pb, and $^{209}$Bi Nuclei in the Energy Range 35-175 MeV,* TSL Progress Report 1998-1999, Ed. A. Ingemarsson, Uppsala University (2000), p. 38.

[12] A.J. Koning, J.-P. Delaroche, and O. Bersillon. *Nuclear Data for Accelerator Driven Systems: Nuclear Models, Experiments and Data Libraries,* Nucl. Instr. and Meth. in Phys. Res. **A414**, 49 (1998).

[13] V.P. Eismont, A.I. Obukhov, A.N. Smirnov, H. Condé, and K. Elmgren, *A Comparison of Proton and Neutron-induced Fission Cross-sections of Heavy Nuclei at Intermediate Energies,* Proc. of 2nd Int. Conf. on ADTT, Kalmar, Sweden, June 3-7, 1996, ed. H. Condé: Uppsala University, 1997, Vol. 2, pp. 599-605.

[14] V.P. Eismont, A.A. Rimski-Korsakov, and A.N. Smirnov. *Fission Cross-sections of Heavy Nuclei at Intermediate Energies for Hybrid Nuclear Technologies,* Proc. of Intern. Conf. on Future Nuclear Systems, Global'97, October 5-10 1997, Yokohama, Japan, p. 1365-1370.

[15] N. Nakao, Y. Uwamino, T. Nakamura, T. Shibata, N. Nakanishi, M. Takada, E. Kim, and T. Kurosawa, *Development of a Quasi-monoenergetic Neutron Field Using the $^{7}$Li(p,n)$^{7}$Be Reaction in the 70-210 MeV Energy Range at RIKEN,* Nucl. Instr. and Meth. in Phys. Res. A420 (1999) 218, N. Nakao, private communication, 1998.

[16] R.C. Byrd and W.C. Sailor, *Neutron Detection Efficiency for NE213 and BC501 Scintillators at Energies Between 25 and 200 MeV,* Nucl. Instr. and Meth. **A274** (1989) 494.

[17] S. Stamer, W. Scobel, and R.C. Byrd, *Measurement of Absolute (p,xn) Cross-sections with 80-800 MeV Projectiles.* Proc. Specialists' Meeting on Neutron Cross-section Standards for the Energy Region above 20 MeV, Uppsala, Sweden, May 21-23 (1991), OECD Nuclear Energy Agency report, NEANDC-305 'U', p. 154, Paris, France, 1991.

[18] H. Condé, S. Hultqvist, N. Olsson, T. Rönnqvist, R. Zorro, J. Blomgren, G. Tibell, A. Håkansson, O. Jonsson, A. Lindholm, L. Nilsson, P.-U. Renberg, A. Brockstedt, C. Ekström, M. Österlund, F.P. Brady, and Z. Szeflinski, *A Facility for Studies of Neutron-induced Reactions in the 50-200 MeV Rang,* Nucl. Instr. and Meth. in Phys. Res. A292 (1990) 121, T. Rönnqvist, private communication, 1993.

[19] M. Baba, Y. Nauchi, T. Iwasaki, T. Kiyosumi, M. Yoshioka, S. Matsuyama, N. Hirakawa, T. Nakamura, Su. Tanaka, S. Meigo, H. Nakashima, Sh. Tanaka, and N. Nakao. *Characterization of a 40-90 MeV $^{7}$Li(p,n) Neutron Source at TIARA Using a Proton Recoil Telescope and a TOF Method,* Nucl. Instr. and Meth. in Phys. Res. A428, 454 (1999).

[20] P. Staples, P.W. Lisowski, and N.W. Hill, Presented in APS/AAPT Conference, Washington, April 18-21, 1995, Bull. Am. Phys. Soc. 40, 962 (1995), P. Staples, private communication (1996) with an update of the data.

[21] V.I. Goldanskiy, V.S. Penkina, and E.Z. Tarumov, *Fission of Heavy Nuclei by High Energy Neutrons,* ZETP (Sov. J. of Experimental and Theoretical Physics) 29, 778 (1955).

[22] P.E. Vorotnikov and L.S. Larionov, *Neutron-induced Fission Cross-sections of Lead and Bismuth Nuclei*, Sov. J. Nucl. Phys. 40, 552 (1984).

[23] T. Fukahori and S. Pearlstein, *Evaluation at the Medium Energy Region for Pb-208 and Bi-209*, Proceedings of the advisory group meeting organised by IAEA, Vienna, October 9-12, 1990, Report INDC(NDS)-245, Vienna, 1991, pp. 93-128.

[24] V.P. Eismont, A.I. Obukhov, A.V. Prokofiev, and A.N. Smirnov, *An Experimental Database on Proton-induced Fission Cross-sections of Tantalum, Tungsten, Lead, Bismuth, Thorium and Uranium,* Proc. of 2nd Int. Conf. on Accelerator Driven Transmutation Technologies and Applications, Kalmar, Sweden, June 3-7, 1996, pp. 592-598, published by Uppsala University (1997).

[25] A.N. Smirnov and V.P. Eismont, *Thin Film Breakdown Counters*, Pribory i Tekhnika Eksperimenta [Instr. Exp. Techn. (USSR)], No. 6, p. 5 (1983).

[26] O. Jonsson, P.-U. Renberg, A. Prokofiev, and A. Smirnov. *A Broad-proton-beam Facility for Irradiation Purposes*, TSL Progress Report 1998-1999, ed. A. Ingemarsson, Uppsala University (2000), p. 43.

# NUCLEON-INDUCED FISSION CROSS-SECTIONS CALCULATIONS AND DEVELOPMENT OF TRANSMUTATION-ACTIVATION DATA LIBRARY FOR TRANSITIVE ENERGY REGION 20-200 MEV

**S. Yavshits, V. Ippolitov, S. Packhomov, G. Boykov**
V.G. Khlopin Radium Institute
28, Second Murinski street, St. Petersburg, Zip: 194021, Russian Federation

**O. Grudzevich**
Institute of Nuclear Power Engineering
Studgorodok, 1, Obninsk, Kalaga reg., Zip: 2492, Russian Federation

## Abstract

The results of a new approach for fission cross-sections at transitive energies are presented and it is shown that the calculations describe experimental data well for both neutron and proton induced fission. The development of the approach and corresponding code system for the calculations of independent and cumulative yields of residual nuclei and fission fragments are discussed and preliminary results are presented.

## 1. Introduction

Nuclear fission of heavy nuclei induced by nucleons at transitive energy region 20-200 MeV is one of the main reaction channels (the fission cross-sections for actinide region can reach value 0.8-0.9 of the reaction cross-section). The accurate knowledge of fission probability for different fission chances allows also defining yields of fission products (fission fragment yields and neutrons emitted from fragment). These data added by particle and isotope yields from other reaction channels (direct and pre-equilibrium emission of nucleons, evaporation of nucleons and light nuclei) give us the possibility to develop the nuclear data necessary for the evaluation of activation of the Pb-Bi target of the accelerator driven systems as well as the data on the fission of fuel and transmutation of actinide radioactive waste.

The energy region 20-200 MeV is the transitive region from the well-investigated low energy region to intermediate energy nucleon-induced reactions. It is well-known that for energies of incoming particles up to 10-20 MeV the mechanism of reaction is defined by the competition between fission and particle evaporation from compound nucleus and fission cross-sections and yields of reaction products are well-reproduced by the statistical models. For higher energies the contributions from the direct and pre-equilibrium reaction stages arise which is used to describe in the framework of intranuclear cascade and exciton models, correspondingly.

In the given work, the new model approach and computer code is developed where the main properties of nucleon-induced reactions on heavy nuclei at transitive energies are calculated in the unified scheme on the base of reliable and detailed description of all main stages of the reaction.

## 2. The model approach

The scheme of new code is shown in the Figure 1. We use for entrance model simulation the coupled channel method in Raynal's version (code ECIS [1]). The deformation of target nucleus in the ground state as well as the 3 lowest excited levels are taken into account in the calculations. The global optical model potential for all nuclei from Pb up to Cf for transitive nucleon energies has been developed by ours early [2]. For all these nuclei and beam energies the reaction cross-section data library has been developed which is further used in the cross-section calculation of secondary reactions.

The intranuclear cascade model in Dubna version [3] has been included in the code for the description of the direct stage of the reaction. The chains of primary and secondary cascades lead to the emission of fast nucleons and the population of residual nuclei in the different nuclear states characterised by mass and charge numbers, excitation energy and number of excitons (A,Z,E*,XpYh distribution) which serve as the input data for the pre-equilibrium processes. The decay of excited states on the pre-equilibrium reaction stage leads again to the particle emission and distribution of excited nuclei (A,Z,E* distribution). The hybrid exciton model with Monte Carlo simulation [4] has been used for the calculation of this reaction stage.

The last stage of statistical decay has been described in the framework of a detailed statistical model based on the well-known code STAPRE [5] for each of the nuclei formed in the previous stages of the reaction. The statistical part of reaction calculations contains a lot of parameters and special efforts have been made in order to reduce the number of fitted parameters and to raise the predictive ability of the code. The new data libraries for the level density parameters, fission barriers, nuclear masses have been developed and included in the calculation scheme [2].

Figure 1. **Scheme of the new code**

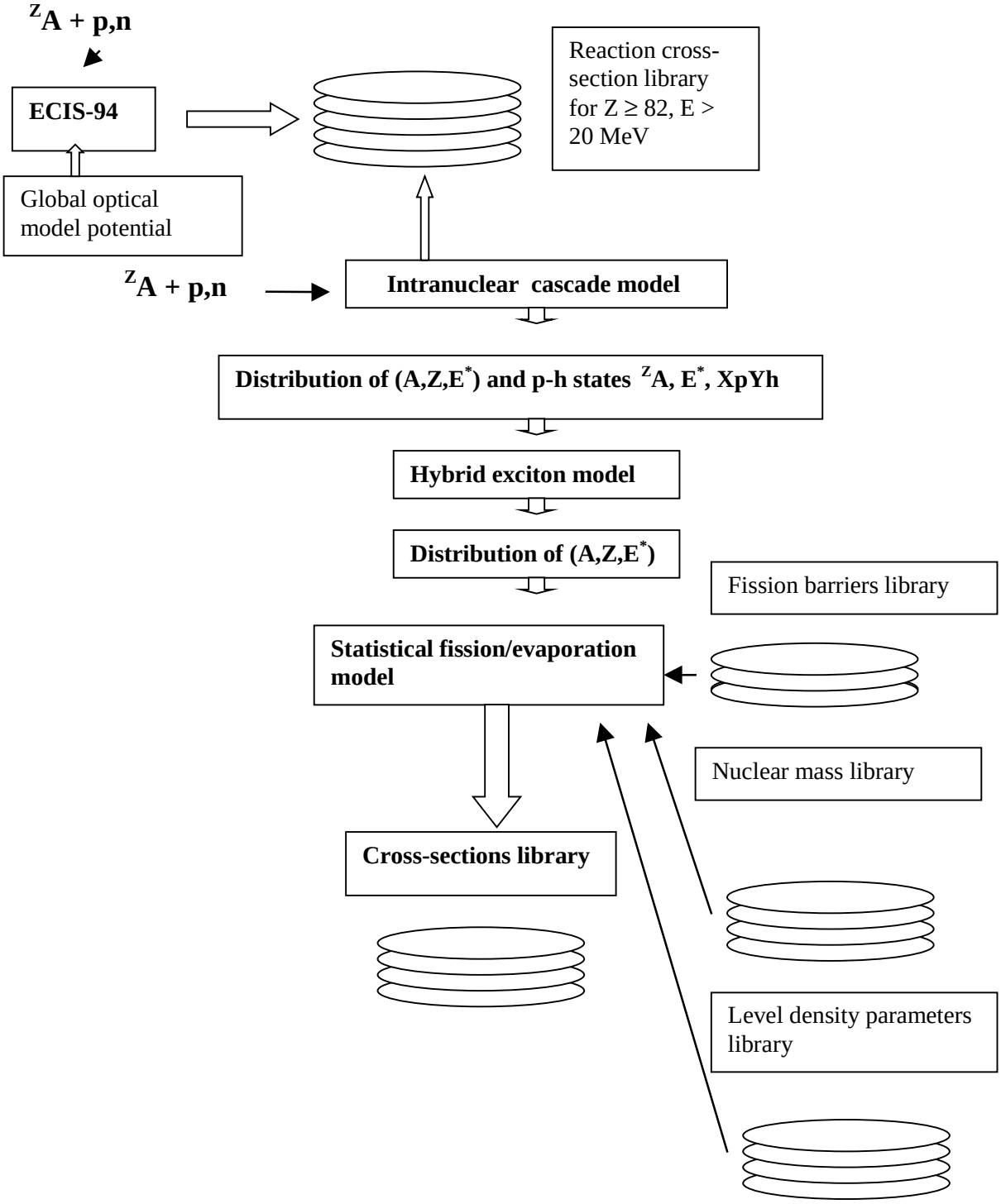

## 3. Results and perspectives

On the base of the developed code system, the systematic calculations of proton and fission cross-sections for the nuclei from Pb to Pu have been carried out for transitive energies of incoming particles. Some results of these calculations are presented in the Figures 2 and 3 in comparison with the experimental data. It can be seen from the figures that our calculations describe the experimental data rather well without any fitting of the model parameters. The preliminary results on the isotope and neutron production are shown in the Figures 4 and 5. The calculations have been done within the framework of the same approach. The agreement with the experimental data is quite satisfactory for these data, too.

It is necessary for the fission product yields calculation to include in the code the model of fission fragment production probability. Such a model should be used at each fission chance for each fissioning nuclei formed at direct+pre-equilibrium stages of the reaction. At present we are working out the statistical model of fission fragment yields in Fong's approximation [6].

Figure 2. **The proton-induced fission cross-section of $^{208}$Pb**

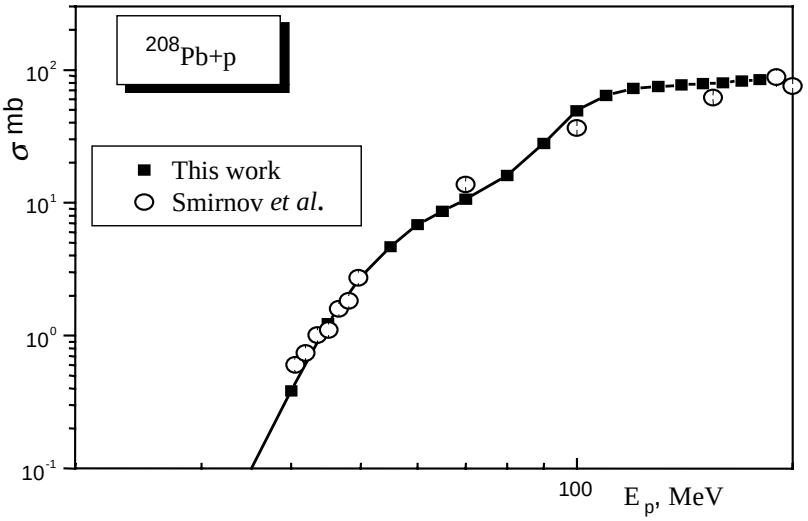

Figure 3. **Neutron-induced fission cross-sections of actinides in comparison with experimental data**

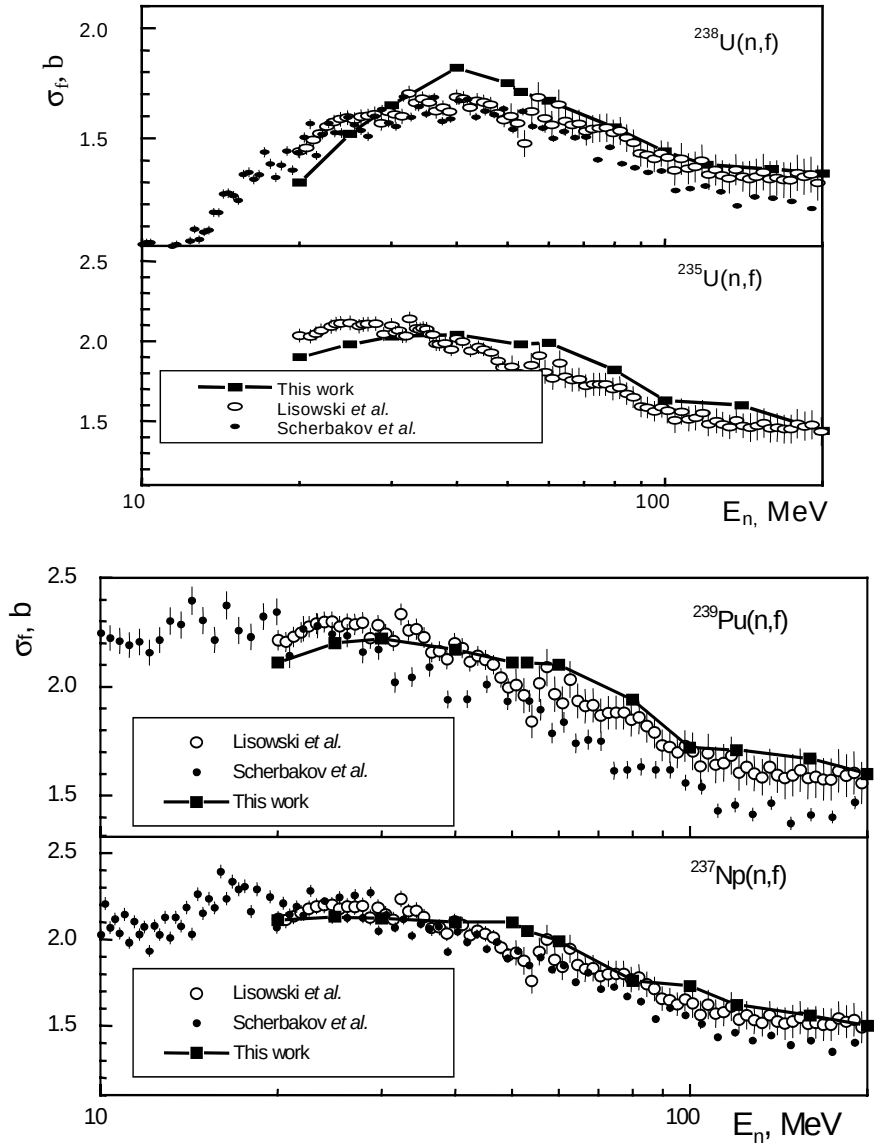

Figure 4. **Yields of U isotopes in the reaction $^{238}$U (1GeV) + p in comparison with the experimental data**

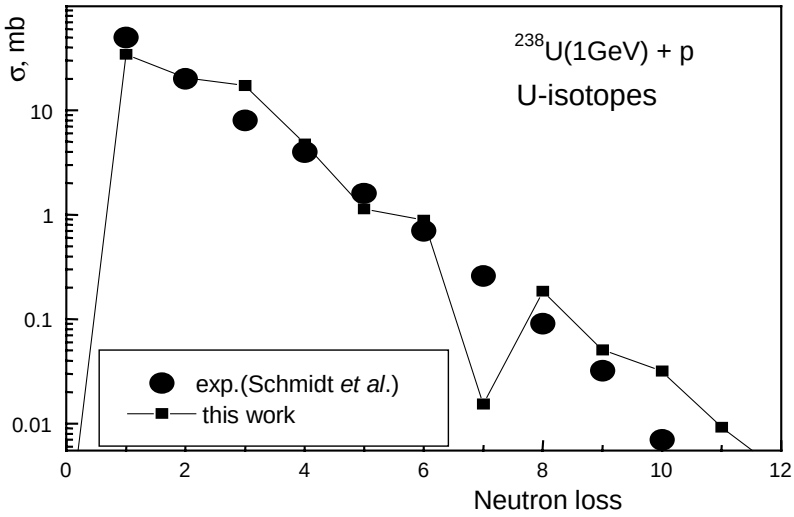


Figure 5. **Neutron spectra from reaction Pb + p**

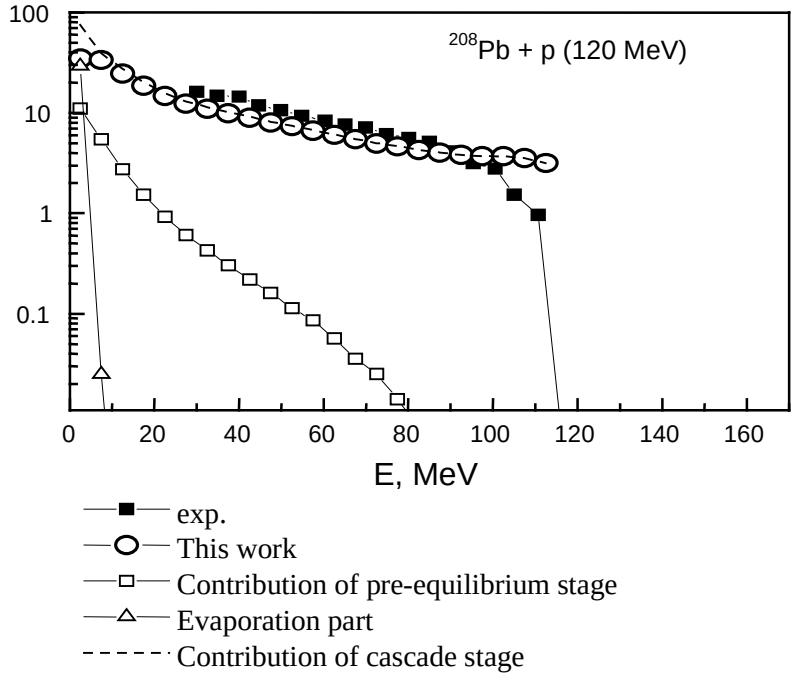

## REFERENCES


[1] J. Raynal, Proceedings of a Specialists Meeting, 13-15 November 1996, Bruyères-le-Chatel, France, p. 159.

[2] S. Yavshits *et al*, Proceedings of IX Int. Conf. On Nuclear Reaction Mechanism, 5-9 June, Varenna, Italy, p. 219.

[3] K.K. Gudima, S.G. Mashnik, V.D. Toneev, Nucl. Phys, 1983, Vol. A401, p. 329.

[4] M. Blann, Phys. Rev., 1996, Vol. C54(3), p. 1341.

[5] O.T. Grudzevich *et al.*, Proc. of Int. Conf. on Nuclear Data for Science and Technology, 1988, Mito, Japan, p. 1221.

[6] P. Fong, Phys. Rev., 1964, Vol. 135B, p. 1338.

# NEUTRON RADIATIVE CAPTURE CROSS-SECTION OF $^{232}$Th IN THE ENERGY RANGE FROM 0.06 TO 2 MeV

**D. Karamanis[1], M. Petit[1], S. Andriamonje[1], G. Barreau[1], M. Bercion[1], A. Billebaud[2],B. Blank[1], S. Czajkowski[1], R. Del Moral[1], J. Giovinazzo[1], V. Lacoste[3], C. Marchand[1],L. Perrot[2], M. Pravikoff[1], J.C. Thomas[1]**

[1]CEN/Bordeaux-Gradignan, France
[2]ISN, Grenoble, France
[3]CERN, Geneva, Switzerland

## Abstract

Neutron capture cross-section of $^{232}$Th have been measured relative to $\sigma(n,\gamma)$ for $^{197}$Au and $\sigma(n,f)$ for $^{235}$U in the energy range from 60 keV to 2 MeV. Neutrons were produced by the $^{7}$Li(p,n) and T(p,n) reactions at the 4 MV Van de Graaff Accelerator of CEN/Bordeaux. The activation technique was used and the cross-section was measured relative to the $^{197}$Au$(n,\gamma)$ standard cross-section up to 1 MeV. Above this energy, the reaction $^{235}$U(n,f) was also used as a second standard and the fission fragments were detected with a photovoltaic cell. The results after applying the appropriate corrections indicate that the cross-sections are close to the JENDL-3 database values up to 800 keV and over 1.4 MeV. For energies in the intermediate range, values are slightly lower to the ones from all the libraries.

## 1. Introduction

During the past few decades a growing concern for the continuous accumulation of large amounts of nuclear wastes and for the future of energy production systems has emerged. The green house effect, the foreseeable limits in fossil fuel resources and the pollution of the environment with combustion by-products, point to the need towards alternative, innovative and safer strategies. New challenges for the different fuel cycle options and nuclear waste management, have produced an impetus in the research for extension of the life span of presently operating reactors, the increase of the fuel burn-up and plutonium recycling (in particular the incineration of actinides and long-lived fission products). Furthermore, the $^{232}$Th-$^{233}$U fuel cycle is studied extensively for energy production and as a waste management option in the next generation of systems like the Energy Amplifier and ATW [1], thermal or fast reactors and the accelerator driven systems (ADS) [2]. Unfortunately, uncertainty in the parameters of systems employing the Th-U cycle, caused by discrepancies in the nuclear data available at present, appears to be higher than the uncertainty caused by different calculational schemes [3]. Hence, the need arises for bringing the quality of these nuclear data to the same level of accuracy as that of the U-Pu cycle [3, 4].

The most crucial reaction channel in the Th-U fuel cycle is the neutron capture on $^{232}$Th, which leads to $^{233}$U after two successive $\beta^-$ decays. Moreover, the above reaction cross-section is currently required with an accuracy of 1-2% in order to be used safely in simulated techniques for predicting the dynamical behaviour of complex arrangements in fast reactors or ADS [3]. As an example of its importance in ADS, a 10% change in the $^{232}$Th capture cross-section gives rise to a 30% change in the needed proton current of the accelerator if the system has to be operated at a sub-critical level of $K_{eff} \approx 0.97$ [5].

Since 1946, there have been a number of relative measurements of the $^{232}$Th(n,γ) reaction cross-section by employing prompt γ-ray detection or activation techniques. However, these are almost the half when compared to the measurements of $^{238}$U(n,γ) reaction cross-section that presents a number of common features. Furthermore, experiments for the exclusive measurement of the above reaction cross-section are even less. Since the measured values differ substantially in the energy range 0.05-1.5 MeV and due to the difficulty of re-normalisation, the current evaluations in the above energy range present discrepancies of the order of 10-30% [4]. Therefore, additional measurements are needed in order to satisfy the required accuracy.

In the present work, the neutron capture cross-section of $^{232}$Th was measured in the neutron energy range from 60 keV to 2.0 MeV. The activation technique was used and the cross-section was measured relative to the $^{197}$Au(n,γ) standard cross-section of ENDF/B-VI up to 1 MeV. The characteristic γ lines of the product nuclei $^{233}$Pa and $^{198}$Au were measured with a 40% HPGe detector. Above this energy, the reaction $^{235}$U(n,f) with values from ENDF/B-VI, was used as a second standard and the fission fragments were detected with a photovoltaic cell. Several experiments and simulations were also performed in order to check all the factors influencing the cross-section values, with special emphasis, to minimise the associated uncertainties and errors.

## 2. Experimental procedure

Neutrons were produced by either the Li(p,n) or the T(p,n) reaction on the 4 MV Van de Graaff Accelerator of the Centre d'Études Nucléaires de Bordeaux-Gradignan (CENBG). A deep (1.7 m depth) "neutron hole" was installed in the neutron beam line of the accelerator in order to eliminate scattered neutrons from the environment (floors, walls and ceiling). The beam was focused and collimated to a spot roughly 0.5 × 0.3 cm$^2$ at the target while beam currents were of the order of

15 μA. At the end of the proton beam line, the target holder was cooled with a continuous flow of a very thin film of water. This was used instead of compressed air cooling since it was experimentally checked that the mono-energetic neutron beam was better stabilised when the water flow was applied.

The threshold of the $^{7}Li(p,n)^{7}Be$ reaction was used for the energy calibration of the VdG accelerator. The selected proton energies with the corresponding neutron energies are presented in Table 1. In this table, the minimum (maximum) neutron energy corresponds to maximum (minimum) proton energy degradation in the LiF target and maximum (minimum) angular spread in the neutron beam at the position of the Th target. With Li as a neutron source and Ep ≥ 2.4 MeV, a second group of mono-energetic neutrons was produced due to the population of the first excited state of $^{7}Be$. The intensity of the second group was calculated with a Monte Carlo simulation.

Table 1. **Selected proton energies and corresponding reactions in the activation measurements**

| **Neutron source (mg cm$^{-2}$)** | **Irradiation** | **Ep (Min) (keV)** | **Ep (Max) (keV)** | **En (Min) (keV)** | **En (Max) (keV)** |
|---|---|---|---|---|---|
| LiF:0.260 | Au-Th-Au[1] | 1 881 | 1 907 | 0.875 | 100 |
| 0.515 | – | 1 928 | 1 991 | 130 | 220 |
| 0.540 | – | 1 928 | 1 995 | 135 | 225 |
| 0.515 | – | 2 008 | 2 070 | 236 | 320 |
| 0.500 | – | 2 017 | 2 077 | 247 | 324 |
| – | – | 2 108 | 2 166 | 354 | 425 |
| 0.540 | – | 2 195 | 2 256 | 452 | 525 |
| – | – | 2 253 | 2 313 | 516 | 588 |
| 0.515 | Au-Th-U[2] | 2268 | 2 325 | 522 | 600 |
| 0.500 | Au-Th-Au[1] | 2 270 | 2 325 | 534 | 600 |
| – | – | 2 294 | 2 349 | 560 | 626 |
| – | – | 2 346 | 2 340 | 616 | 680 |
| – | – | 2 422 | 2 475 | 697 | 760 |
| – | – | 2 499 | 2 551 | 778 | 840 |
| – | – | 2 577 | 2 627 | 860 | 920 |
| – | – | 2 654 | 2 704 | 940 | 1 000 |
| TiT: 1.0 | Au-Th-U[2] | 1 700 | 1 803 | 870 | 1 000 |
| – | Au-Th-Au[1] | 1 710 | 1 803 | 880 | 1 000 |
| – | Au-Th-U[2] | 1 953 | 2 047 | 1 126 | 1 250 |
| – | – | 2 205 | 2 292 | 1 379 | 1 500 |
| – | – | 2 458 | 2 539 | 1 632 | 1 750 |
| – | – | 2 458 | 2 539 | 1 632 | 1 750 |
| – | – | 2 710 | 2 786 | 1 882 | 2 000 |

[1]Al box.
[2]Fission chamber.

Thorium metal targets (Goodfellow SARL) were of high purity (99.5%), 1 mm thick and a surface of 1 × 1 cm$^{2}$. Two experimental devices were used for samples irradiation, a Cd box and a fission chamber. In the first one, the Th foils were packed together with two Au foils on each side

(same surface and 0.5 mm thickness) and were placed in a Cd box ($5 \times 5$ cm$^2$ and 1 mm of Cd thickness) in order to eliminate any contribution from the thermal neutron background. The box was tied with tiny nylon wires at the centre of a thin Fe ring and aligned with the proton beam; the assembly was placed at 5 cm from the Cu backing of the neutron source.

Figure 1. **Schematic representation of the neutron fission chamber**

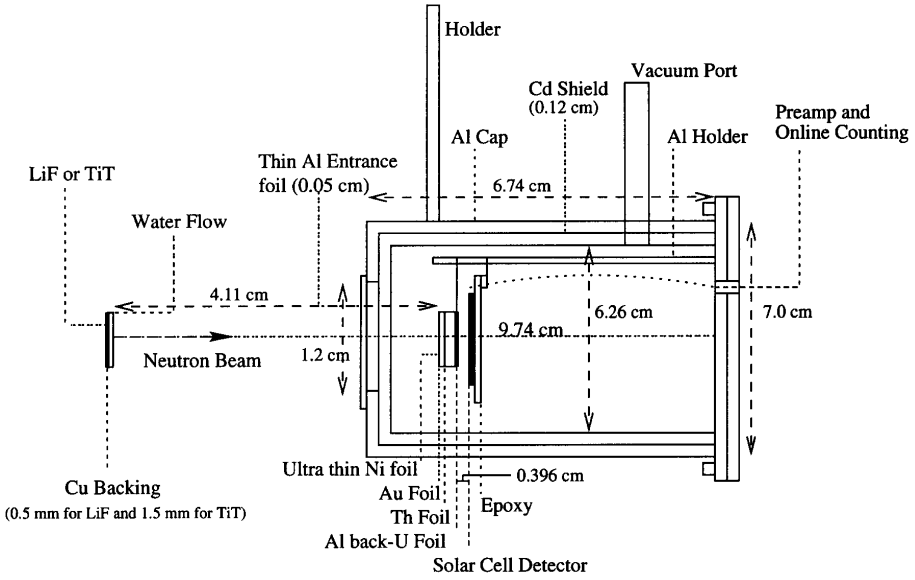


In the fission chamber, a $^{235}$U thin foil (0.04 mg cm$^{-2}$) on an Al backing (0.047 cm) was used as a second reference foil. The configuration used with the fission chamber is schematically depicted in Figure 1. Fission fragments were detected online with a photovoltaic (solar) cell. This device was used because of its minimal mass inside the neutron fission chamber. The cell was a monocrystalline $n^+p$ junction with 360.36 mm$^2$ surface. The dead zone of the photovoltaic cell was determined by direct micro-measurement of the thickness of the Al grids. The detection efficiency for fission fragments from $^{235}$U was considered twice that for alpha particles that were observed with a Si surface barrier. The later was collimated in order to suspend exactly the same solid angle as the cell during the irradiations.

The Cd box or the fission chamber were irradiated around 20 hours at 0° with respect to the proton beam. During the irradiation, the flux was monitored with a $He^3$ detector that was placed 2 meters from the neutron source. After each irradiation, the intensity of the $\gamma$ ray lines emitted by the de-excitation of the produced nuclei $^{233}$Pa ($E\gamma$ = 312 keV (38.6%)) and $^{198}$Au ($E\gamma$ = 412 keV (96%)), was measured with $\gamma$ spectroscopy with a 40% HPGe and for 5 cm source to detector distance. The acquisition time varied between 1-2 hours for Au and 1-2 days for Th. The pulser method was used for dead time correction. The photopeak areas were determined with the use of PAW program [6]. The efficiency of the Ge detector was determined with a $^{152}$Eu punctual source and the use of GEANT3.21 [7] and MCNP4B [8] simulation codes.

Two more experiments were performed for the estimation of the thermal and epithermal neutron background in the experimental hall. Prior to irradiations, the coincidence technique of the alpha and triton produced in the $^6$Li(n,$\alpha$)T reaction and detected with two Si junctions (J1-J2) in a "sandwich" arrangement, was used. Several combinations with different target support materials, with and without cadmium shielding and distances from the neutron production target were investigated. The optimal

conditions with the minimum thermal background were produced by placing the cadmium-shielded device in around 5 cm from the neutron production LiF target that was supported on copper. At the end of irradiations, the background was measured by irradiating simultaneously three Cd boxes with Au foils inside and at different distances from the neutron source.

## 3. Analysis and results

The neutron capture cross-section of $^{232}$Th relative to the cross-section $\sigma(n,\gamma)$ for $^{197}$Au and $\sigma(n,f)$ of $^{235}$U is given by the relation:

$$\frac{\sigma_{Th}(<En>)}{\sigma_{Rf}(<En>)} = \frac{\varepsilon(Rf)}{\varepsilon(312)} \cdot \frac{^{Th}I}{^{Rf}I} \cdot \frac{^{Rf}N}{^{Th}N} \cdot \frac{f(T^{Th},t)}{f(T^{Rf},t)} \quad (1)$$

where $<E_n>$ is the mean neutron energy in the sample, $I$ the photopeak or fission fragments area, $\varepsilon$ the efficiency for the $^{233}$Pa or $^{198}$Au $\gamma$ lines or the fission fragments, $N$ the number of atoms in the samples and $f$ a time factor relating the measured peak intensities to the end of irradiation. In the case that the $^{235}$U foil is used as a second reference, the time factor is simply the time of irradiation. In the present experiment, the neutron flux in the Th target was assumed to be the same as the mean value of the flux calculated from the two foils (Au-Au or Au-U) in each side of the Th target. Therefore, the above formula was modified to account for the time difference in measuring the two Au reference targets or the different cross-sections in the case of Au-U foils.

The efficiency of the HPGe detector for the activity measurements of thorium or gold samples was determined with the following way. The dependence of recording decay events by the HPGe as a function of photon energy was determined with a punctual $^{152}$Eu source that was placed at 5 cm or 10 cm. The detector's geometry was then simulated with MCNP4B and GEANT3.21 in order to reproduce the observed experimental values. Finally, the detector's efficiency was determined by replacing the punctual source in the simulation with the extended gold or thorium box. In this way, the values of (1.19 ± 0.03)% for the recorded 412 keV line of $^{198}$Au and (1.27 ± 0.03)% for the 312 keV line of $^{233}$Pa, were obtained. The above values were also confirmed experimentally.

Since the photovoltaic cell was calibrated by replacing it with a collimated and suspending the same solid angle Si surface barrier, the combined product $\varepsilon_U \cdot N_U$ was measured instead of each separate term in Equation 1 and a value of $2 \times (3.27 \pm 0.10) \times 10^{16}$ was determined. Furthermore, the dead zone of the photovoltaic cell was determined by direct measurement of the grids thickness and was found (4.45 ± 0.02)%.

### *3.1 Corrections*

One of the factors with primary importance in fast capture measurements with the activation method is the thermal-epithermal background present in the experimental hall. Its contribution and spoiling of experimental results can be non-negligible and have to be corrected. For this reason, two experiments were performed. In the first, the "room background" was evaluated with the coincidence technique of the reaction $^{6}$Li(n,$\alpha$)T. Since the alpha and triton particles from thermal or fast neutrons are emitted in opposite directions with different production rates (300:1) and with different energies, they can be separated. In this way the contribution of the "room background" was estimated to be insignificant. However and due to the increased apparatus mass seen by the neutron flux, a quantitative analysis of the experiment could be of less value.

Figure 2. **Dependence of the total activation on the target–sample distance. Solid curve represents linear fit of Equation 2 to the data after corrected the 2nd and 3rd Au foils for flux attenuation (A = 7 205, B = 0.7). Dashed curve represents linear fit to the data after corrected the foils with an MCNP simulation (A = 7 185, B = 2.3)**

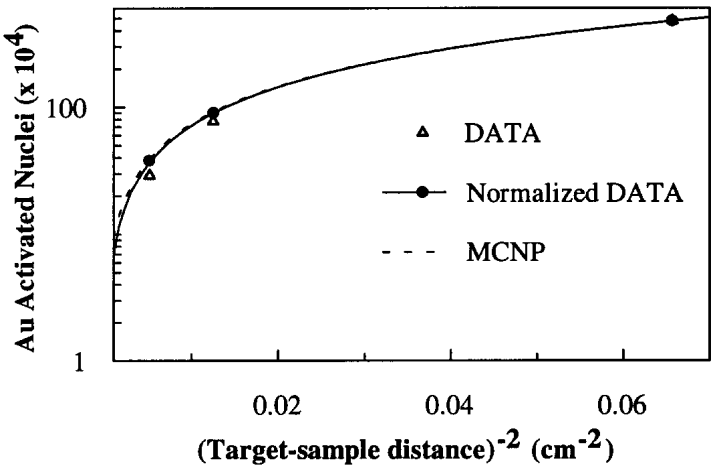


Therefore, a simple irradiation experiment was performed with an assembly of three Au foils at different distances from the neutron source. Since the room-scattered neutrons are uniformly distributed in the vicinity of the target, the produced $^{198}$Au activity should be constant with target-sample distance. The activity due to the primary neutron source should vary as $1/r^2$ whereas the in-scattering contribution from the structural materials near the target or the sample should also exhibit a distance dependence close to $1/r^2$. Hence, the total activation of any foil will be given by:

$$I(r) = A / r^2 + B \tag{2}$$

According to the results obtained and shown in Figure 2, the "room" neutron background contribution can be considered negligible.

However, the effect of other factors is not negligible and the observed activation of any foil had to be corrected due to:

- Neutron energy spread because of proton energy degradation in the source.
- Effects of finite dimensions of neutron source and targets on neutron energy spread.
- Second neutron energy group from the $^{7}$Li(p,n)$^{7}$Be* reaction for energies higher than 600 keV.
- Inelastic and elastic neutron scattering within the intermediate experimental environment
- Multiple elastic and inelastic scattering in the target foils

Therefore, a Monte Carlo code with all the above effects was developed for an IBM AIX 4.3.2 operating system. The code includes source angular and energy distribution, energy-dependent cross-sections and considers multiple scattering. All the cross-sections are entered as tables with linear interpolation. Neutrons are randomly produced inside the target and their angular distribution and different emission probability in the energy range of the proton degradation in the target is chosen according to evaluated cross-sections [9,10]. Their path is followed and their energy is monitored. The

only assumption of the code is that the angular distribution of the produced neutrons is constant in their energy spread interval.

Diagram 1. **Flow diagram of the analog Monte Carlo code for the determination of the correction factors in the neutron capture cross-section of $^{232}$Th**

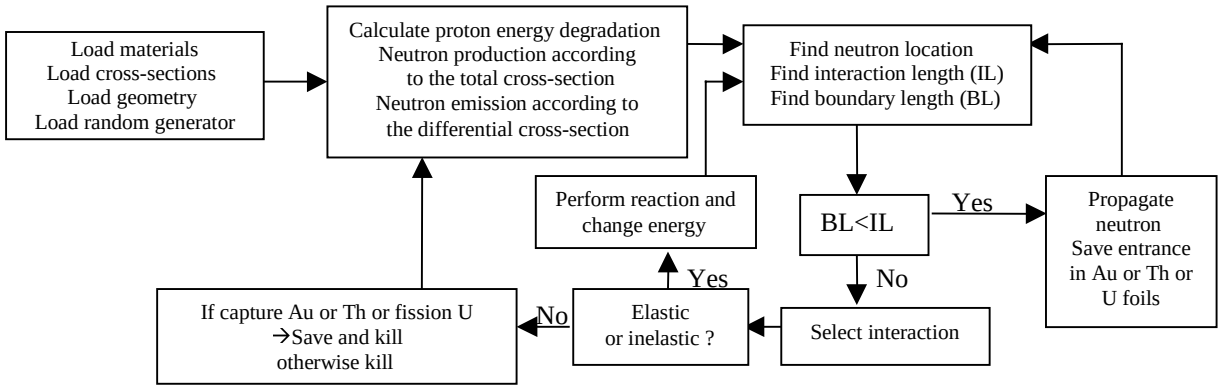


The architecture of the code is schematically depicted in Diagram 1. A best estimate of capture cross-section values that approximate the "true" cross-sections had to be used as an input data file for this calculation. The JENDL-3 evaluated nuclear data library was chosen as the source for the required neutron cross-sections for $^{232}$Th and ENDF/B-VI for $^{197}$Au or $^{235}$U.

The code was applied firstly to the experimental points obtained with the Cd box and the mean neutron capture energy produced from unscattered neutrons was determined. It was also observed that captures produced after scattering in the neutron source backing and water or the entrance foils and the foils themselves (in-scattering or self-scattering), were mainly inside the neutron energy spread and for some cases amount to as much as several percent of the total captures. A global activity multiplication correction factor defined as the ratio of captures produced by unscattered neutrons to the total captures, was determined. It should also be noted that since the neutron capture cross-section of $^{232}$Th was measured relatively and the correction for in- and self- scattering captures was almost the same for all the foils, it was partially compensated or even cancelled out.

In the case of the fission chamber, the statistics were rather poor and the required running time exceeded the one available. Therefore, an approximate treatment with MCNP4B was used instead after comparing its results to that of the developed code for the Cd box. An agreement better than 97% was observed. It was therefore applied afterwards in all the measurements with the fission chamber.

With the implication of the above correction, the values of neutron radiative cross-section of $^{232}$Th in the energy range from 60 keV to 2 MeV were determined and are given in Figure 3a. In the same figure, the evaluations of the different databases are also included. The overall error was found to vary between 3.4 to 7.8%. It is also worth noting the excellent agreement of the cross-section values around 600 keV and 1 000 MeV of neutron energy that were obtained with different neutron sources and different activation devices.

Figure 3. **Neutron radiative capture cross-section of $^{232}$Th of the present work in comparison with a) the existing evaluated data from the four major neutron data reference libraries and b) with experimental and normalised data**

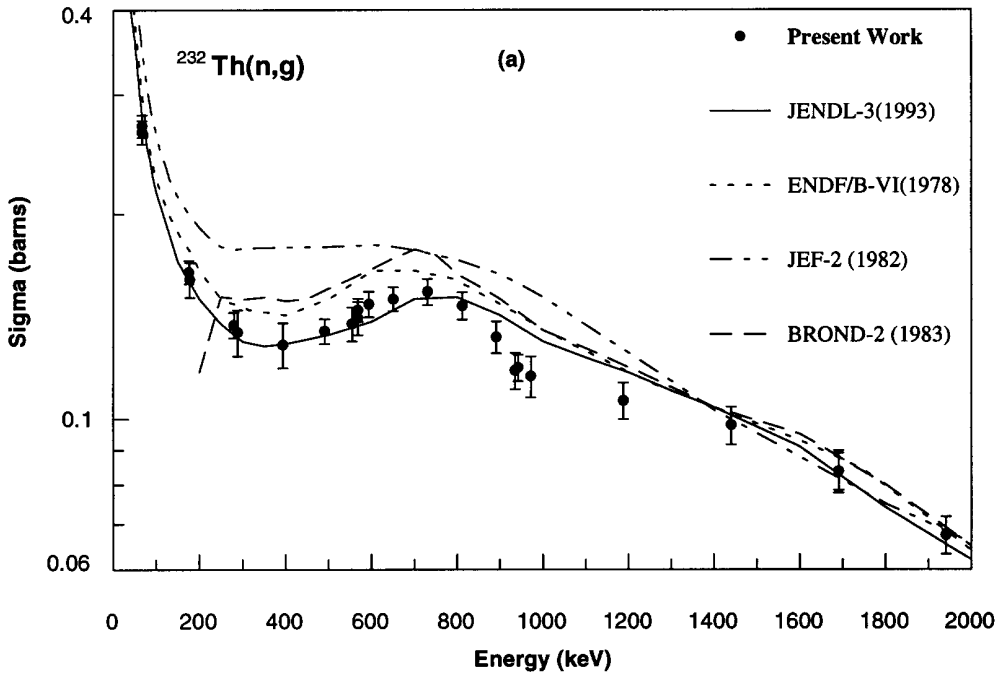


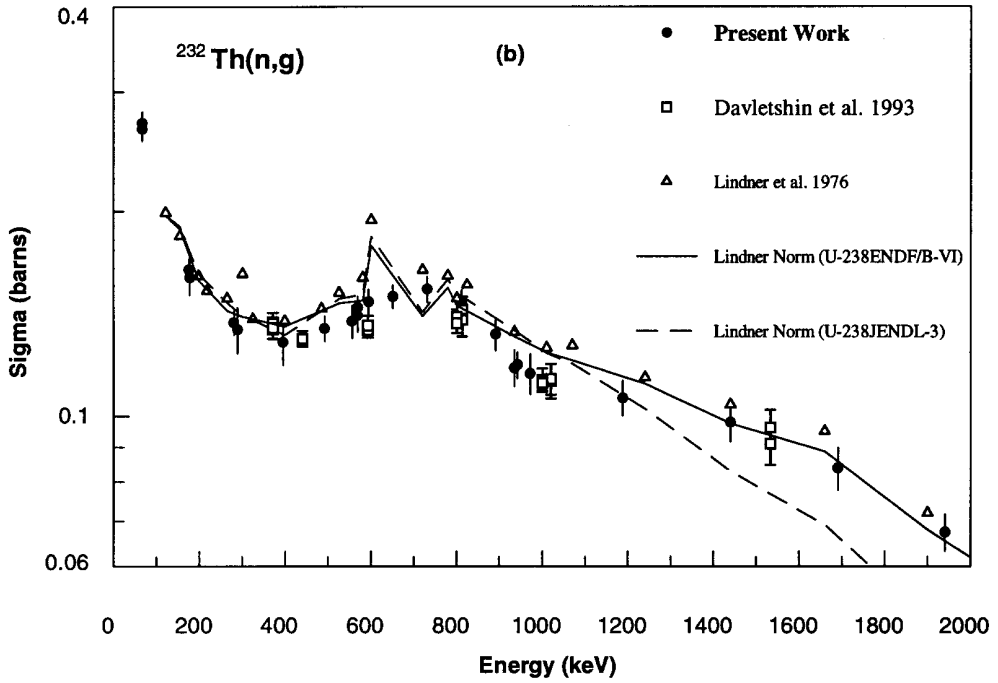

## 4. Conclusions

The values of the neutron capture cross-section of $^{232}$Th that were measured in the present work are in agreement with the JENDL database up to 800 keV and over 1.4 MeV. For energies in the intermediate range, values are slightly lower to all the databases but in agreement with the most recent values of Davletshin *et al*., [11]. Moreover, a re-normalisation of $^{232}$Th and $^{238}$U neutron capture data of Lindner *et al*., [12] (the most reliable considered data and the basis of many evaluations) with $^{238}$U from the current ENDF and JENDL databases was undertaken (Figure 3b). The later reveals that a very good agreement is reached with the data of the present work, data from a time of flight experiment that were the basis for the JENDL evaluation [13] and data that could be the basis of a new BROND or ENDF evaluation [11,12].

*Acknowledgements*

This work was partially supported by GEDEON-PACE Programme, Région Aquitaine and European Commission Nuclear Fission Safety Programme. The support in codes and references from the Nuclear Data Centres of NEA and IAEA, is kindly acknowledged. One of the authors (D.K.) would like to thank the European Commission Nuclear Fission Safety Programme for providing the Marie Curie Postdoctoral Research Fellowship (Contract No. FI4W-CT98-5004).

## REFERENCES

[1] C.D. Bowman *et al*., *Nuclear Energy Generation and Waste Transmutation Using an Accelerator-driven Intense Thermal Neutron Source*, NIMA 320 (1992) 336-367; C. Rubbia *et al*., *Conceptual Design of a Fast Neutron Operated High Power Energy Amplifier*, CERN/AT/95-44(ET) (1995).

[2] AIP Conference Proceedings No. 346 of the Int. Conf. on Accelerator-driven Transmutation Technologies and Applications, Las Vegas, NV, USA, July 1994.

[3] V.G. Pronyaev, *Summary Report of the Consultants' Meeting on Assessment of Nuclear Data Needs for Thorium and other Advanced Cycles*, INDC(NDS)-408, IAEA, August 1999.

[4] B.D. Kuzminov and V.N. Manokhin, *Status of Nuclear Data for the Thorium Fuel Cycle*, Nuclear Constants, No. 3-4 (1997), p. 41.

[5] M. Salvatores, *Nuclear Data for Science and Technology*, Conf. Proceedings Vol. 59, G. Reffo, A. Ventura and C. Grandi (Eds.), Bologna 1997.

[6] PAW, *Physics Analysis Workstation*, CERN Program Library Long Write-up Q121, CERN Geneva (1995).

[7] GEANT, *Detector Description and Simulation Tool*, CERN Program Library Long Write-up W5013, CERN, Geneva (1993).

[8] MCNP, *A General Monte Carlo Code for Neutron and Photon Transport*, J.F. Briesmester (Ed), (*LA-12625-M*, 1993).

[9] H. Liskien and A. Paulsen, *Neutron Production Cross-sections and Energies for the Reactions $^{7}$Li(p,n)$^{7}$Be and $^{7}$Li(p,n)$^{7}$Be**, Atomic Data and Nuclear Data Tables 15 (1975) 57-84.

[10] H. Liskien and A. Paulsen, *Neutron Production Cross-sections and Energies for the Reactions T(p,n)$^{3}$He, D(d,n)$^{3}$He and T(d,n)$^{4}$He*, Atomic Data and Nuclear Data Tables 11 (1973) 569-615.

[11] A.N. Davletshin *et al.*, *Neutron Radiative Capture Cross-sections for the $^{232}$Th and $^{197}$Au Nuclei in the 0.37-2.5 MeV Region*, INDC(CCP)-375 and INDC(CCP)-389 (1994).

[12] M. Lindner, R.J. Nagle and J.H. Landrum, *Neutron Capture Cross-sections from 0.1 to 3 MeV by Activation Measurements*, Nucl. Sci. & Engin. 59 (1976) 381-394.

[13] K. Kobayashi, Y. Fujita and N. Yamamuro, *Measurement of Neutron Capture Cross-section of Thorium-232 from 1 keV to 408 keV*, J. Nucl. Sci. Technol. 18 (1981) 823-834.

# DETERMINATION OF THE NEUTRON FISSION CROSS-SECTION FOR $^{233}$Pa FROM 0.5 TO 10 MeV USING THE TRANSFER REACTION $^{232}$Th($^{3}$He,pf)$^{234}$Pa

**M. Petit[1)], M. Aiche[1)], S. Andriamonje[1)], G. Barreau[1)], S. Boyer[1)], O. Busch[1)],S. Czajkowski[1)], D. Karamanis[1)], F. Saintamon[1)] , E. Bouchez[2)], F. Becker[2)], F. Gunsing[2)], A. Hurstel[2)], Y. Le Coz[2)], R. Lucas[2)], M. Rejmund[2)], C. Theisen[2)], A. Billebaud[3)], L. Perrot[3)]**

[1]CEN Bordeaux, BP 120, 33175 France

[2]CEN Saclay, DAPNIA, 91191 Gif-sur-Yvette, France

[3]ISN Grenoble, 53, Avenue des Martyrs, 38026 Grenoble, France

## Abstract

Neutron induced fission cross-section of $^{233}$Pa in the fast neutron energy range from 0.5 to 10 MeV was determined for the first time as a two term product of the fission probability of $^{234}$Pa nucleus and the same compound nucleus formation cross-section. The first term was measured with the transfer reaction $^{232}$Th($^{3}$He,p)$^{234}$Pa while the second one was calculated. The tendency of the resulting data to agree with the existing evaluated one, is a proof for the validity of the utilised method.

## 1. Introduction

New reactors using the uranium-thorium fuel cycle are under studies in order to provide safer and cleaner nuclear energy as highly radiotoxic actinide waste (Pu, Am and Cm isotopes) will be produced in lower quantities than the currently used uranium fuelled reactors. Moreover, further developments of this thorium based cycle rely on nuclear data libraries of the quality achieved for the uranium ones.

The primary reaction of importance using the thorium cycle is the one producing $^{233}$U from neutron capture on $^{232}$Th, the net production of $^{233}$U is controlled by the 27 days half-life of $^{233}$Pa: a fertile nucleus ($^{232}$Th) is transformed into a fissile nucleus ($^{233}$U) after neutron capture and 2 successive β decays.

$$^{232}\mathrm{Th} \xrightarrow{+n} {}^{233}\mathrm{Th} \xrightarrow[(22\ \mathrm{min})]{\beta} {}^{233}\mathrm{Pa} \xrightarrow[(27\ \mathrm{days})]{\beta} {}^{233}\mathrm{U}$$

$^{233}$Pa as a precursor of $^{233}$U may capture neutrons and could lead to a reactivity decrease of the reactor, conversely and after a shut down, the build up of $^{233}$U increases this reactivity; this so called Protactinium effect should add severe requests on the $^{233}$Pa and $^{233}$U inventories for reactivity control. There is no equivalent effect in the well studied $^{238}$U-$^{239}$Pu fuel cycle as the equivalent intermediate isotope $^{239}$Np has a relatively shorter half-life (2.35 days).

Furthermore, neither the neutron capture cross-section nor the neutron induced fission cross-section have been measured for $^{233}$Pa up to now. The reason of this absence is the short decay half life of the $^{233}$Pa nucleus (27 days) that leads to an extreme activity of $7.10^8$ bq $\mu g^{-1}$ s-1. Due to this high radioactivity, there is no technique presently available to measure directly the $^{233}$Pa(n,f) reaction cross-section.

The particular aim of this work is to provide data for the neutron induced fission of $^{233}$Pa in the fast neutron energy range from 0.5 to 10 MeV. To overcome the problem of the induced radioactive $^{233}$Pa, we have used the transfer reaction $^{232}$Th($^3$He,p)$^{234}$Pa that leads to the desired $^{234}$Pa nucleus as it should be observed in the $^{233}$Pa(n,f) reaction. Several years ago, this method has been used successfully to estimate the neutron-induced fission of short-lived targets like $^{231}$Th (25.6 h), $^{233}$Th (22.1 min) etc.

## 2. Theory

Transfer reaction measurements give access to **the fission probability Pf($E^*$)** as a function of excitation energy. The equation relating the two quantities can be written as:

$$Pf(E_{exc}) = \sum_{J\pi} \left( \alpha(E_{exc}, J, \pi) \frac{\Gamma_F(E^*, J, \pi)}{\sum_i \Gamma_i(E^*, J, \pi)} \right) \quad (1)$$

where $\alpha(E_{exc}, J, \pi)$ is the relative population of spin states $(J, \pi)$.

Neutron induced fission measurements give access to **the fission cross-section $\sigma_F$(En)** as a function of the incident neutron energy that is relating to the excitation energy as:

$$E_{exc} \approx Sn + En \quad (2)$$

Therefore, the neutron induced fission cross-section can be determined from the following equation:

$$\sigma_F(En) = \sigma_{NC}^{T}(En) \sum_{J,\pi} p_{n,f}^{J,\pi} \frac{N(J^{\pi}, En)}{\sum_{J} N(J^{\pi}, En)} \quad (3)$$

where $N(J^{\pi},En)$ is the relative final spin states $(J^{\pi})$ population and $Pn,f$ is the fission probability for the spin states $(J^{\pi})$ given from the relation:

$$p_{n,f} = \frac{\Gamma_f(En, J, \pi)}{\sum_i \Gamma_i(En, J, \pi)} \quad (4)$$

Concluding the neutron induced fission cross-section can be found as a two term product or:

$$\sigma_f(E) \approx \sigma_{NC} * P_f(E_{exc} \approx Sn + En) \quad (5)$$

The last relation is well verified if we assume that we have enough fission channels so that the total spin population differences between the two processes do not affect the output channel. This assumption should hold for the odd-odd fissionning system $^{234}$Pa.

## 3. Experimental procedure and data reduction

The $^{3}$He beam was provided by the IPN Orsay Tandem facility at three different energies (24, 27 and 30 MeV). The $^{232}$Th targets (100 µg/cm$^2$) were deposited onto 50 µg/cm$^2$ carbon backings. The ($^{3}$He,p) channel has been discriminated among the other competing channels (d, t and alpha outgoing light charged particles) with a ΔE-E counter telescope placed at 5 cm from the target and at 90° relative to the $^{3}$He beam axis. The ΔE detector was 300-µm thick fully depleted Si detector. The E counter was 5-mm thick Si detector.

The telescope energy calibration has been obtained with the reaction $^{208}$Pb($^{3}$He,d)$^{209}$Bi using ground state Q value and excited states in $^{209}$Bi, as it is indicated in Figure 1.

Figure 1. **Excited states of $^{209}$Bi that were used for the telescope energy calibration**

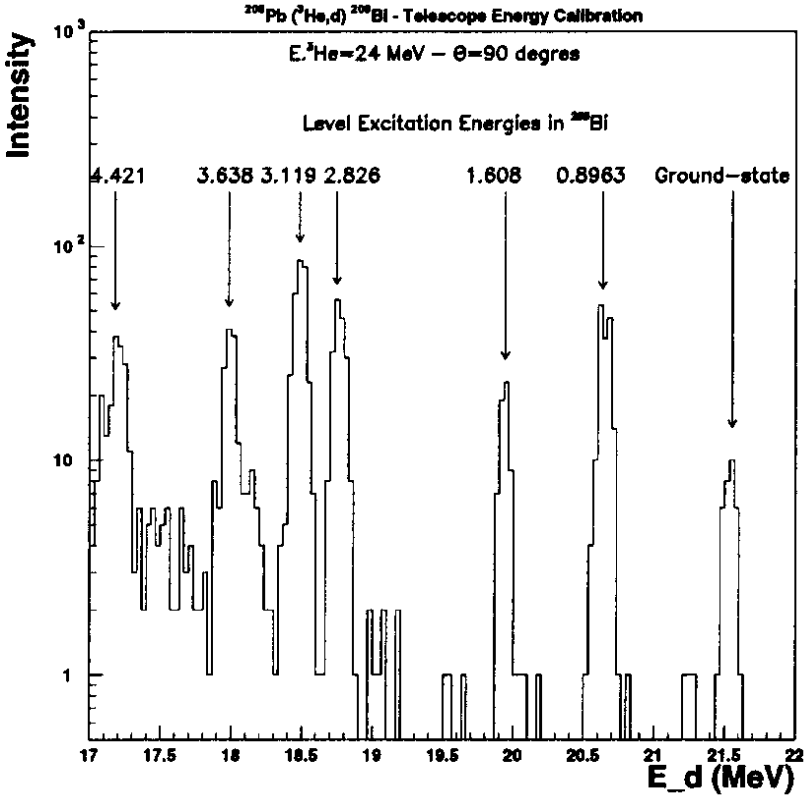


Fission fragments were detected with two multi-solar cell arrangements placed at 5 cm from the target and at 0° and 90° relative to the recoil direction of the $^{234}$Pa nucleus (~27°). The Saclay VXI acquisition system was used in this experiment, as it was designed and used for the Euroball and Saphir multi-detector arrays [1]. The master trigger was generated either by a triple coincidence of signals from the ΔE, E and fission counters (***coinc***.) or by the double coincidence from the ΔE and E detectors (***singles***). The ***singles*** spectra have been corrected for the contribution from the carbon backing by subtracting the spectrum from a separate carbon irradiation run. The two spectrums are shown in the Figure 2. The ***coinc***. spectra were corrected for random coincidence events by using the appropriated scaled ***singles*** spectra.

The fission probability of $^{234}$Pa was calculated from the number of fission events detected in coincidence with the outgoing light charged particles according to the relation:

$$P_f = \frac{2\pi}{\Omega_f} \frac{\text{Ncoinc}}{\text{Nsingles}} \tag{6}$$

Figure 2. **Singles protons and deuterons spectra from the transfer reactions a) $^{232}$Th($^{3}$He,p)$^{234}$Pa (solid line) and b) $^{12}$C($^{3}$He,p)$^{14}$N (dashed line)**

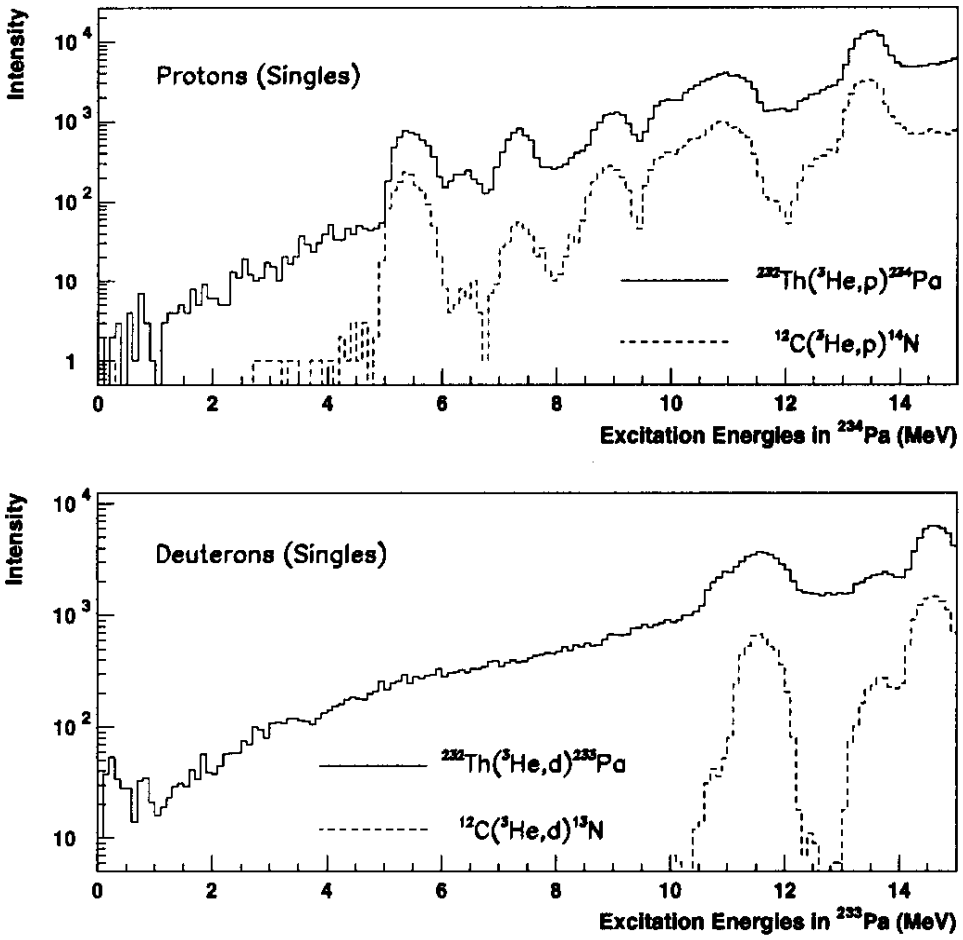


In the last relation $\Omega_f$ is the solid angle efficiency for fission fragment detection and it was determined from a calibrated $^{252}$Cf source, placed in the same geometry.

The consistency of the method and the reliability of our measurements were checked with the reaction $^{232}$Th($^{3}$He,df)$^{233}$Pa. Since this reaction had been studied in the past by Back *et al*. [2], their fission probability of $^{233}$Pa was compared with the one obtained in the present work and an excellent agreement was found (Figure 3).

Figure 3. **The fission probability of $^{233}$Pa as obtained in the present work (open cycles) and in the Los Alamos experiment by Back *et al* [2] (full cycles).**

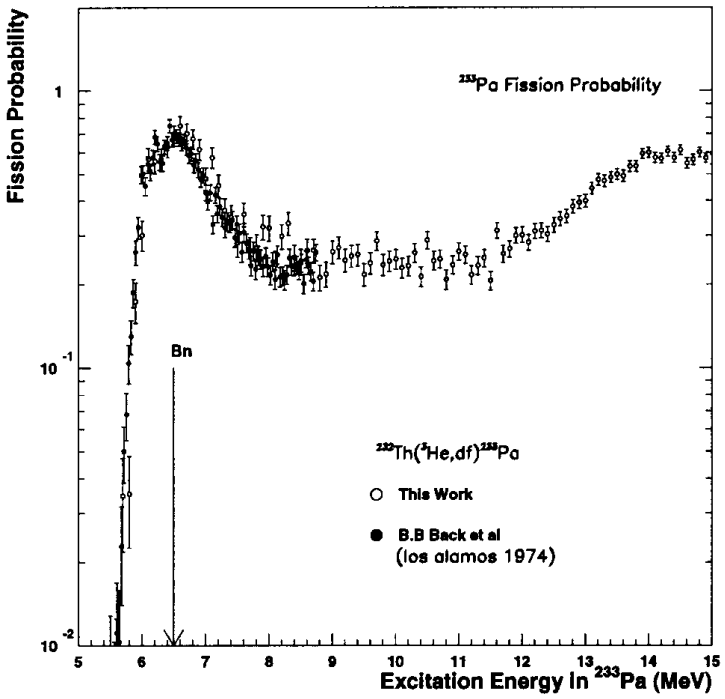


Figure 4. **Neutron induced fission cross-section of $^{233}$Pa and the existing evaluated data**

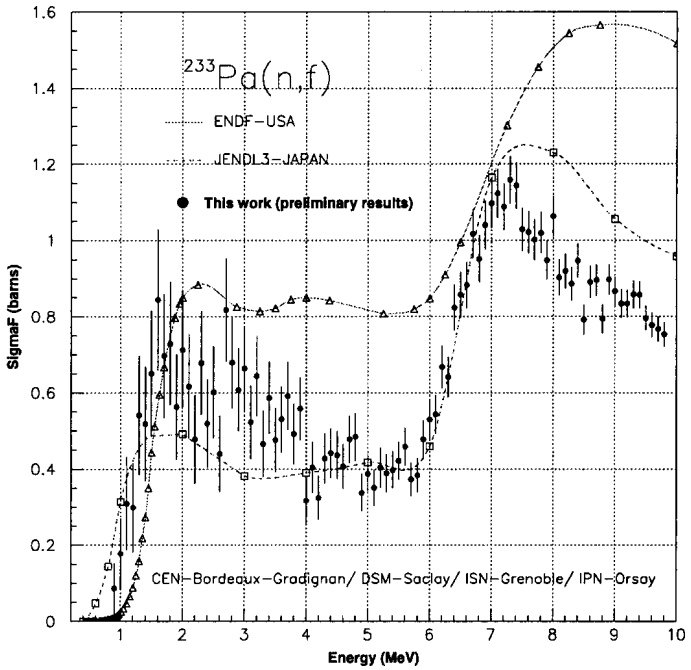

Following the procedure proposed by J.D. Cramer and H.C. Britt [3], the neutron induced fission cross-section $^{233}$Pa(n,f) was determined as the product of the $^{234}$Pa measured fission probability and the computed compound nucleus formation cross-section of $^{234}$Pa. In the later calculation, the transmission coefficients T($l$,s = ±1/2) of Perey and Buck [4] were used. The results obtained are shown in Figure 4 in comparison with the existing evaluated data from the ENDF/B-VI and JENDL-3 reference libraries.

## 4. Conclusion

Although the results should be viewed as preliminary, a tendency for following the JENDL evaluation can be observed, at least for neutron energies greater than 4 MeV. The high errors for lower neutron energies, do not permit a safe conclusion. Due to this, a new experiment is planned in the very near future which combined with updated transmission coefficients will provide a clear determination of the neutron induced fission cross-section of $^{233}$Pa. It is also planned that the present work will extend to the measurement of the $^{233}$Pa(n,γ) reaction in order to complete our knowledge on the $^{233}$Pa effect.

## REFERENCES


[1] C. Thiesen, C. Gautherin, M. Houry, W. Korten, Y. Lecoz, R. Lucas, G. Barreau, C. Badimon, T.P. Doan, *The SAPHIR Detector*, in Ancillary Detectors and Devices for Euroball, H. Grawe (Ed.) GSI 1997 p.47.

[2] B.B. Back, H.C. Britt, O. Hansen, B. Leroux, J.D. Garrett, *Fission of Odd-A and Doubly Odd Actinide Nuclei Induced by Direct Reactions*, Phys. Rev. C10 (1974) 1948-1965.

[3] J.D. Cramer and H.C. Britt, *Neutron Fission Cross-sections for $^{231}$Th, $^{232}$Th, $^{235}$U, $^{237}$U, $^{239}$U, $^{241}$Pu, and $^{243}$Pu from 0.5 to 2.25 MeV Using (t,pf) Reactions,* Nuclear Science and Engineering 41 (1970) 177-187.

[4] E.H. Auerbach and F.G.J. Perey, *Optical Model Neutron Transmission Coefficients, 0.1 to 5.0 MeV,* Brookhaven National Laboratory, BNL 765 (T-286) (1962).

# MEASUREMENT OF DOUBLE DIFFERENTIAL CROSS-SECTIONS FOR LIGHT CHARGED PARTICLES PRODUCTION IN NEUTRON INDUCED REACTIONS AT 62.7 MeV ON LEAD TARGET

**M. Kerveno, F. Haddad, P. Eudes, T. Kirchner, C. Lebrun**
SUBATECH, Nantes, France

**I. Slypen, J.P. Meulders**
Institut de Physique Nucléaire, Louvain-la-Neuve, Belgique

**V. Corcalciuc**
Institute of Atomic Physics, Bucharest, Roumania

**C. Le Brun, F.R. Lecolley, J.F. Lecolley, M. Louvel, F. Lefèbvres**
Laboratoire de Physique Corpusculaire de Caen, Caen, France

## Abstract

In the framework of nuclear waste transmutation, we have measured $d^2\sigma / d\Omega dE$ for protons, deuterons, tritons and alpha production in neutron induced reactions on a lead target. Due to the structure of the neutron beam, incident neutron energies between 30 and 62.7 MeV have been obtained at once. The analysis of 62.7 MeV neutron is now complete for hydrogen isotopes and a first set of comparisons has been done with calculations. On one hand, it is found that the GNASH-ICRU data do not give the correct cross-sections (neither absolute value nor shape). In the other hand, a comparison for protons using FLUKA is working reasonably well except an underestimation of the pre-equilibrium emission around 30 MeV at forward angles and an overestimation of thermal emission at backward angles. Further data on protons induced reactions at the same energy, obtained within an European concerted action, will be available soon allowing a stronger constraint on theoretical calculations.

## 1. Introduction

The renewal interests on intense neutron source have put forward the necessity of new sets of nuclear data. This is particularly true, in the intermediate energy range between 20 and 200 MeV, for the development of new options for nuclear waste management based on the concept of hybrid system which combines an intense high energy proton beam with a sub-critical fission reactor. One important point of these studies is to know precisely the characteristics of the nuclear reactions taking place in the spallation target that is intended to be in Pb-Bi or Hg. In particular, it's necessary to estimate, in reactions induced by neutrons, the production of light charged particles (lcp) which may have critical effects on materials.

At present, code calculations are used to simulate these phenomena. Below 20 MeV, the upper limit of the databases, codes provide results with a good level of confidence. Above 150 MeV, Intra Nuclear Cascade calculations provide also good results. On the contrary, in the intermediate energy region where the pre-equilibrium emission is important, new theoretical approaches seem to be necessary to ensure a good link between low and high-energy processes.

These new approaches based on pre-equilibrium models will allow increasing the upper limit energy value (from 20 to 150 MeV) of data bases providing that theoretical codes could have sufficient predictive power in this energy range. Thus it's necessary to measure new cross-sections to constrain these codes in order to improve their predictive power and to evaluate the quantity of hydrogen and helium isotopes that will be emitted from the lead target and eventually estimate their interactions with structure materials. A large concerted program of nuclear data measurements is now carrying out by several French and European laboratories to measure double differential cross-sections production for light charged particles in neutron induced reactions on different targets.

We report hereby double differential cross-sections for protons, deuterons and tritons production from a lead target at 62.7 MeV incident neutron energy.

## 2. Experimental set-up

The experiment has been done at the fast neutron facility existing at the cyclotron CYCLONE at Louvain-la-Neuve [1]. The neutron beam is obtained using the $^{7}Li(p,n)^{7}Be_{gs}$ (Q = -1.644 MeV) and $^{7}Li(p,n)^{7}Be^{*}$ (Q = 0.431MeV) reactions. The neutron facility is presented in Figure 1. The important features of this line are the presence of a beam peak off, BPO, upstream the lithium target to get the time at which the neutrons are created and a faraday cup which collect the non-interacting deflected protons. The scattering chamber is located 3.28 m after the neutron production point and is followed by a second chamber which contains a second beam monitor system.

Figure 1. **Global view of the experimental set-up**

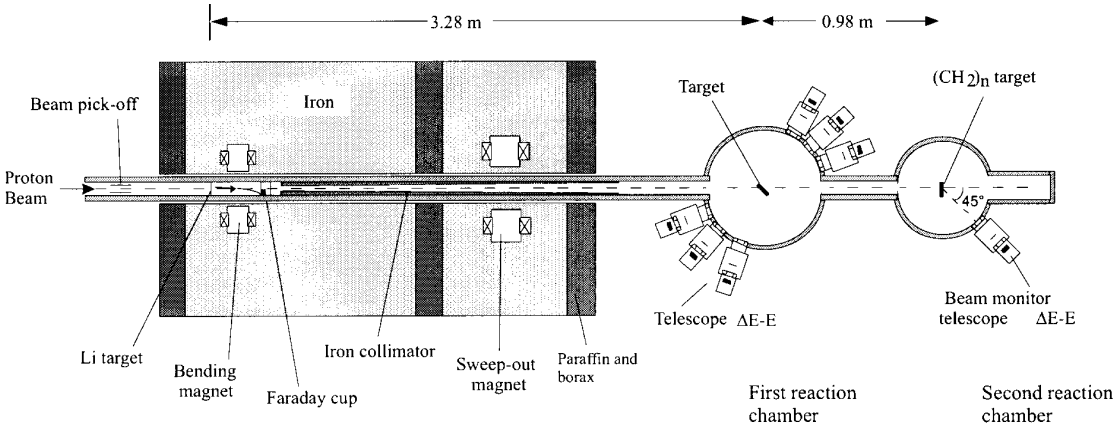


About $10^6$ n/s are available in the reaction chamber when a 10μ A proton beam interacts on a 3 mm thick natural lithium target [2]. The neutron spectrum is presented in Figure 2. It consists of a well-defined peak located at 62.7 MeV containing about 50% of the neutrons and a flat continuum at low neutron energy, which is 8 times lower than the peak maximum. The full width at half maximum of the peak is 4 MeV. The neutron beam spot is quite large at the reaction point as shown in the inset of Figure 2 that presents the radial neutron distribution normalised to the intensity on the centre.

Figure 2. **Neutron spectrum produced by a 65 MeV protons beam on a lithium target. The inset shows the beam profile, normalised to the centre intensity, 3 m downstream the lithium target.**

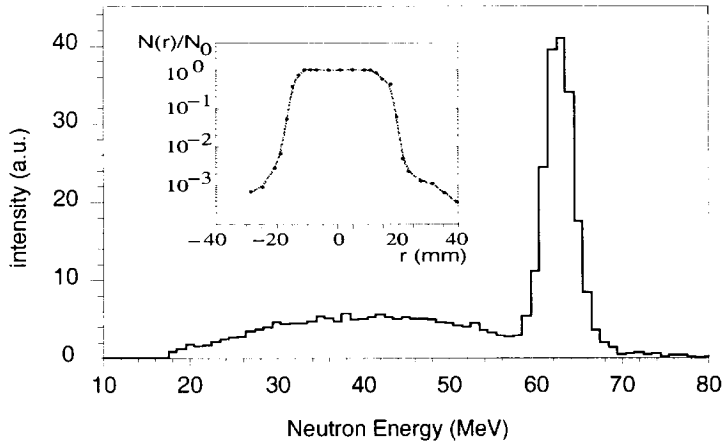


The experimental set-up is based on the one used by the group of J.P. Meulders [3,4]. The reaction chamber allows to use simultaneously six telescopes. Each telescope is composed of a ΔE detector (100 μm thick and 4 cm in diameter NE102 plastic scintillator) and an E detector (22 mm thick and 38.1 mm in diameter CsI crystal). A set of two collimators is inserted in the telescope as shown in Figure 3 to precisely define the detection solid angle. The ΔE detector gives a fast time signal, which allows time of flight measurement and ensures a good reconstruction of the incident neutron energy. The CsI thickness has been optimised to stop the light charged particles produced in our experiment and a pulse shape analysis of the signal is performed.

Figure 3. **Schematic view of a telescope**

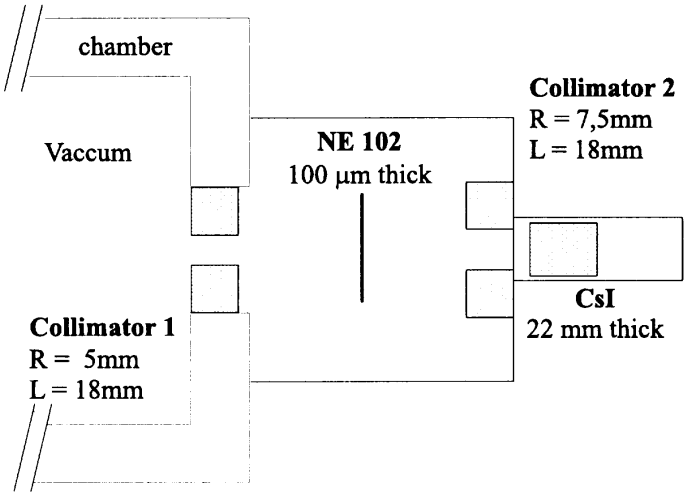


During the experiment, a quite complete angular distribution has been obtained from 20° to 70° by step of 10° in the forward hemisphere and at 110° and 160° in the backward hemisphere. Two different configurations have been used to allow two times longer recording data time at backward angles.

## 3. Data analysis

The particle identification is obtained by performing a pulse shape discrimination of the CsI detector signal. Plotting the slow (CsI_s) versus the fast (CsI_f) component of the CsI light output allows to separate the different hydrogen isotopes as well as the helium. As shown on Figure 4, the good quality of the discrimination added to the possibility to suppress most of the background (neutron and γ) using the ΔE-E correlation facilitates the particle identification.

Figure 4. **CsI slow versus fast component of the light output**

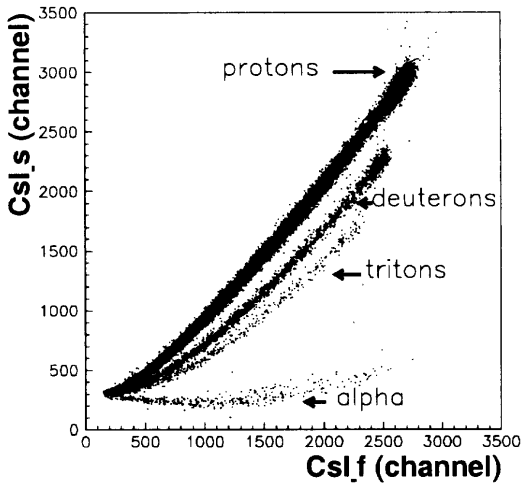

To get the proton (deuteron) energy calibration of our detectors we have used recoil protons (respectively deuterons) from elastic neutron scattering on $CH_2$ ($DH_2$) target at 6 different angles from $20^o$ to $70^o$. The time calibration is also extracted from these data.

Figure 5. **Total time of flight as a function of the measured energy for alpha particles in a lead run**

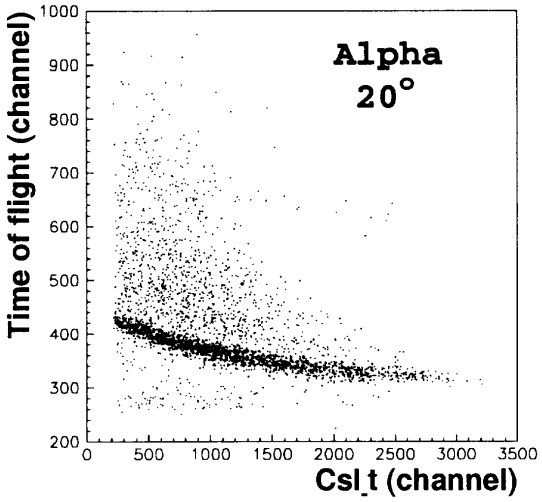


The triton and the alpha calibration have been performed using the time of flight information available for these particles, following the relation $T_{cp} = T_{tot} - T_n$ where $T_{tot}$, corresponds to the measured time between the BPO and the ΔE signals, $T_n$ to the time made by the neutron to go from the BPO to the target and $T_{cp}$ to the time of flight of the particle from the target to the ΔE detector. The special neutron beam energy distribution (see Figure 2) allows selecting only the neutrons from the peak. The bi-parametric plot shown on Figure 5 presents $T_{tot}$ versus the measured energy in channel for alpha particles in a lead run. A clear band appears corresponding to the 62.7 MeV incident neutrons for which $T_n$ is known. For several points on this band, it is then possible to extract the alpha particle energy from $T_{cp}$ and to determine the energy calibration curve. The same method applies also for the other kind of particles. In particular, the calibration obtained by this method for protons and deuterons gives similar results as the first method based on elastic scattering. In Figure 6, calibration curves used for telescope 1 are summarised for isotopes under study.

Figure 6. **Calibration curves used for telescope 1. Proton corresponds to the full black line, deuteron to the dashed line, triton to the dotted line and alpha to the dashed-dotted line.**

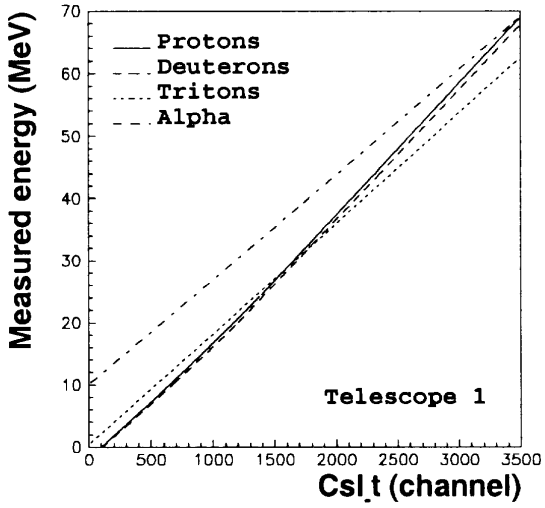


Using the calibration curves, it is possible, event by event, to determine the lcp energy and then $T_{cp}$ to deduce $T_n$ and the neutron energy. As an illustration, in Figure 7, the total deuteron spectrum is plotted as a function of energy. The inset of Figure 7 shows the reconstituted neutron incident energy distribution. By selecting a slice in the neutron spectrum, the deuteron spectrum can be obtained for the corresponding neutron incident energies. As examples, deuterons created by neutrons of 62.7 MeV (respectively 43 MeV) are represented as hashed histogram (squared histogram). It is then possible in one experiment using 65 MeV protons to measure cross-sections at neutron incident energy ranging from 30 MeV to 62.7 MeV.

Figure 7. **Deuteron spectrum obtained by selecting 62.7 MeV (respectively 43 MeV) incident neutron energy is presented as hashed (squared) histogram**

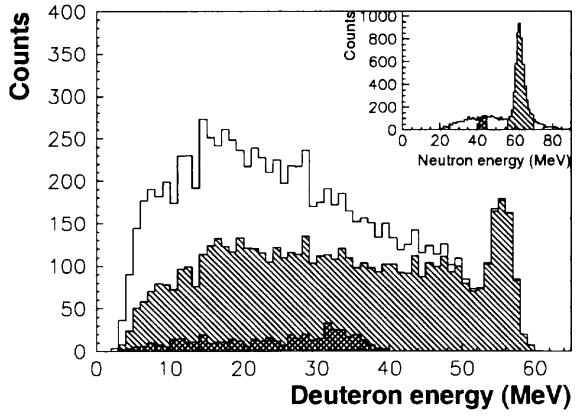


The absolute normalisation of the lead double differential cross-section is obtained by using the n-p scattering cross-section extracted from the $CH_2$ calibration runs [3].

### *3.1 Corrections*

Several corrections have to be made on our data. One concerns the particle scattering on the telescope collimators, the others are coming from the target thickness (0.3 mm). In order to quantify these corrections, we used the GEANT code [5] to simulate as closely as possible the experimental setup and the beam structure.

#### *3.1.1 Diffusion on the collimator set*

In Figure 8, the effect of the collimators on a well define energy beam, as shown on the inset of Figure 8, have been plotted. The diffusion leads to a long tail at low energy. The broadening of the peak is due to the energy losses in the target. Using the simulation, it is possible to estimate the pollution of the tail, normalised to the peak population, in each energy bin. Doing these calculations from 5 to 70 MeV allows us to have an estimation of the full diffusion contribution. The iterative correction procedure consists on removing the tail contribution from the spectrum starting from the highest bin: the population of the highest energy bin does not contain any pollution and the corresponding tail contribution can be estimated from the simulation and discarded for each bin of the spectrum.

Figure 8. **Simulation showing the effect of the proton scattering on the collimator set. The inset shows the particle energy before entering our telescope.**

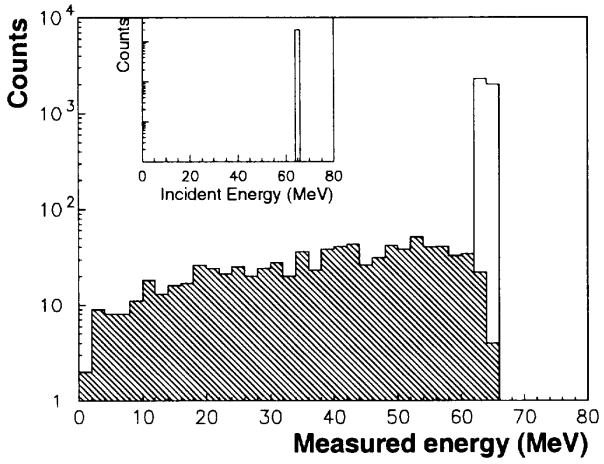


The result of such a procedure is shown on Figure 9 for protons at 20° in the laboratory. The highest spectrum corresponds to the non-corrected one and the lowest one to the corrected one. The effect of the correction is increasing with decreasing energy bin due to the accumulation of corrections coming from higher bins. Such correction corresponds to an overall effect of 13% for protons, 10% for deuterons, 5% for tritons and is negligible for alpha.

Figure 9. **Proton spectrum before and after scattering corrections at 20°.**

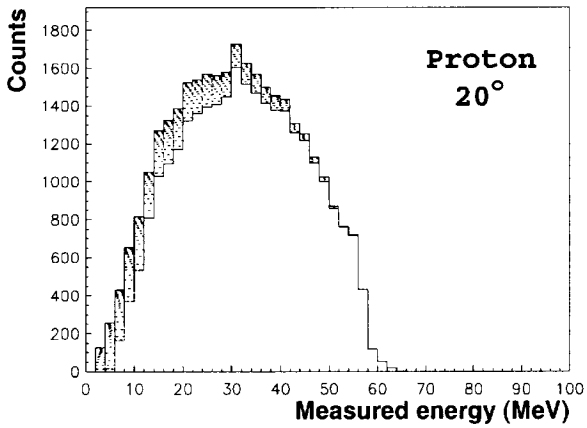


*3.1.2 Thick target corrections*

Another correction consists of taking into account the energy lost in the target in order to get the emitted energy from the measured energy. In Figure 10, the correlation between emitted energy and mean measured energy is presented for triton and alpha. In both pictures, the dashed line characterises the equality between both energies whereas dots show the effect of our thick lead target. For triton, and the other hydrogen isotopes, the difference is small and of the order of our energy binning. It implies that the correction is a simple shift in energy. On the contrary, the effect for alpha is important and a special method is being developed.

Figure 10. **Emitted energy versus measured energy for triton (left) and alpha (right) for the used target. The dashed line corresponds to no thickness effect.**

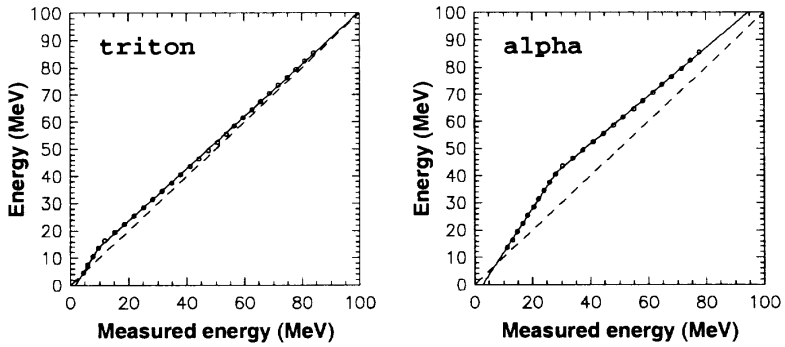


The last correction affects only the low energy particles, which are created without enough energy to cross the entire target and to be detected. This indicates that only the particles created in a fraction of the target, the part close to the output side, can be detected. It is then possible to determine a so-called active target fraction (ATF) which can varied between 0 (nothing can escape) and 1 (everything can escape). The correction depends on the emitted energy and on the type of the particle. Figure 11 shows the evolution of ATF as a function of the emitted energy for tritons and alpha. For hydrogen isotopes, the correction starts below the maximum of the coulomb barrier down to 0 and its effect is small due to the low population. For alpha, this effect goes up to 43 MeV implying a special treatment, which is still under study.

Figure 11. **Active target fraction (see text) as a function of emitted energy.**

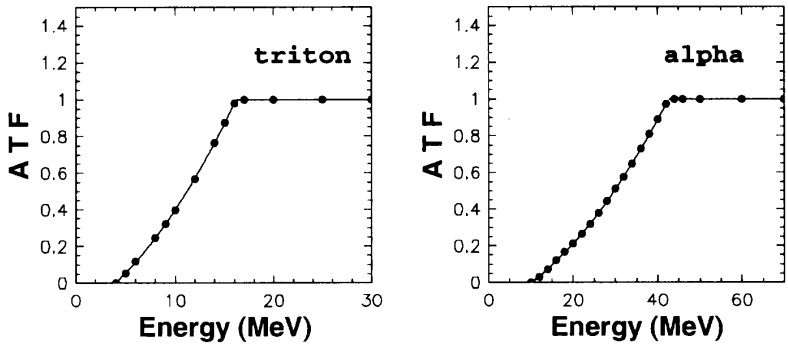


## 4. Results

Dealing with all these corrections, cross-sections can be extracted for proton, deuteron and triton. Using the Kalbach [6] systematic, it is possible to determine the differential cross-section in energy. Figure 12 presents the dσ/dE for the proton (dots), deuteron (triangles) and triton (square). Energy bins of 2 MeV have been used for proton and deuteron and of 3 MeV for triton. The proton spectrum shows a smooth behaviour with a maximum around 18 MeV. For the deuteron spectrum, the maximum is less pronounced and a small rise appears above 57 MeV due to direct processes. Since our most forward angle is 20°, we do not have enough information to fit properly this part of the spectrum and we decide not to determine the cross-sections above 57 MeV for deuterons. For tritons, the low statistic does not allow us to determine the cross-section above 47 MeV. The integration of these spectra gives a production cross-sections of 290 ± 22 mb for protons, 70 ± 5 mb for deuterons and 24 ± 2 mb for tritons.

Figure 12. **dσ/dE for proton (dots), deuteron (triangles) and triton (squares) in n + Pb at 62.7 MeV.**

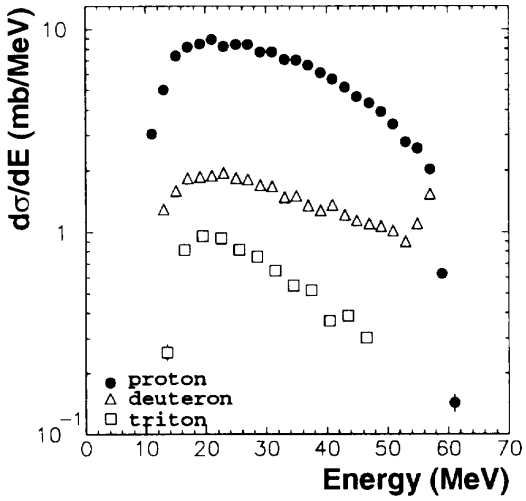


Before starting any comparison with theoretical calculations, it is interesting to compare our experimental results with those found in the literature. No data exists on neutron induced reactions at

this energy and the deuteron data of [7] obtained in proton induced reactions are the only data available to compare with. Since we are looking to deuteron production and that Bi and Pb are neighbours, the production cross-sections in proton and neutron have to be similar in the pre-equilibrium region. On Figure 13, double differential cross-sections are plotted for 20°, 60° and 160°. The black dots correspond to our data and the triangles to the Bertrand and Peelle one [7]. A good agreement is found on the overall angular distribution.

Figure 13. **Deuteron $\frac{d^2\sigma}{dEd\Omega}$ at 20°, 60° and 160°. The dots correspond to neutron induced reaction (this work) and triangles to proton induced reactions [7].**

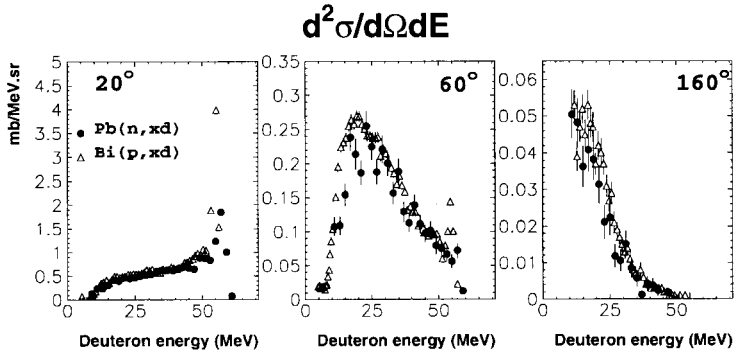


## 5. Comparison with theoretical calculations

As a first set of comparisons, we used two well-known code FLUKA and GNASH. The GNASH data are coming from a publication of ICRU [8] whereas FLUKA [9] results have been obtained locally. In Figure 14, the double differential cross-sections for protons are reported at 3 different angles. The left column shows ICRU data as dashed line whereas FLUKA data are plotted on the right column as dotted line. In all pictures, the black dots correspond to our data. The ICRU data overestimates, in all spectra, our experimental results. In addition, it presents, at forward angles, a double humped structure localised at low and high energy which is not present in our data that are maximum at medium energy. FLUKA is giving a good total cross-section (270 mb) thanks to the compensation of the underestimation of the medium energy part of the spectrum at forward angles and the overestimation of the low energy part at backward angles. Nevertheless, the shapes of the spectra are in close agreement with the data.

Figure 14. **Proton $\frac{d^2\sigma}{dEd\Omega}$ for n + Pb at 62.7 MeV. Dots are the experimental data whereas curves in the left (right) column correspond to ICRU [8] (FLUKA [9]) results.**

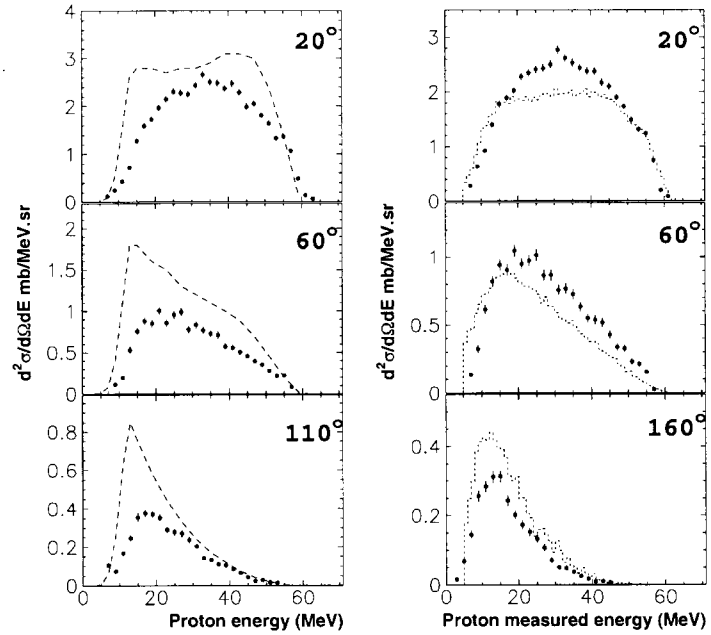


For composite particles such as deuterons, the discrepancy is greater as is shown on Figure 15 where the dashed line corresponds to ICRU data and black dots to our experimental data.

Figure 15. **Deuteron $\frac{d^2\sigma}{dEd\Omega}$ for n + Pb at 62.7 MeV. Dots are the experimental data whereas curves correspond to ICRU [8] results.**

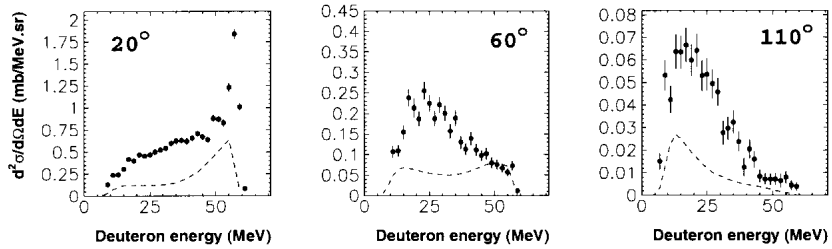


## 6. Conclusion

Proton, deuteron and triton double differential cross-sections have been measured in 62.7 MeV neutron-induced reactions on natural lead target. A special attention has been devoted to the correction procedures coming from our use of thick target and collimators. Measurements were done with a good statistic and are in good agreement with data of [7]. The comparison with some well-known theoretical data from GNASH-ICRU and FLUKA shows some disagreements. The largest differences are found for GNASH-ICRU that neither reproduces the shape of the spectra nor the

absolute values of proton spectra. The composite particles are also not correctly reproduced. FLUKA is giving a good total cross-section value thanks to differences cancelling each other at forward and backward angles. Further comparisons with theoretical approach are underway especially with model including pre-equilibrium emission such as MINGUS [10]. Other data on lead using proton-induced reactions at the same energy beam are under analysis and will be delivered soon to enrich the data tables.

This work has been supported by the European Commission under the concerted action N°FI4I-CT98-0017 and by the GDR GEDEON (research group CEA – CNRS – EdF – FRAMATOME).

## REFERENCES

[1] A. Bol, P. Leleux, P. Lipnik, P. Macq and A. Ninane, *A Novel Design for a Fast Neutron Beam*, NIM, 1983, 214, 169-173.

[2] I. Slypen, V. Corcalciuc and J.P. Meulders, *Geometry and Energy Loss Features of Charged Particle Production in Fast-neutron Induced Reactions*, NIMB, 1994, 88, 275-281.

[3] I. Slypen, V. Corcalciuc and J.P. Meulders, *Proton and Deuteron Production in Neutron-induced Reactions on Carbon at $E_n$ = 42.5, 62.7 and 72.8 MeV*, Phys. Rev. C, 1985, 51, 1303-1311.

[4] S. Benck, I. Slypen, V. Corcalciuc and J.P. Meulders, *Light Charged Particle Emission Induced by Neutrons with Energies Between 25 and 65 Mev on Oxygen I. Protons and Deuterons*, Eur. Phys. J. A., 1998, 3,149-157.

[5] *GEANT: Detector Description and Simulation Tool*, CERN program library long write-up W5013.

[6] C. Kalbach, *Systematic of Continuum Angular Distributions: Extensions to Higher Energies*, Phys. Rev. C, 1988, 37, 2350-2370.

[7] F.E. Bertrand and R.W. Peele, *Complete Hydrogen and Helium Particle Spectra from 30 to 60 Mev Proton Bombardment of Nuclei With A = 12 to 209 and Comparison with the Intranuclear Cascade Model*, Phys. Rev. C, 1973, 8, 1045-1064.

[8] **I**nternational **C**ommission on **R**adiation **U**nits and **M**easurements, *Nuclear Data for Neutron and Proton Radiotherapy and for Radiation Protection*, reports 63, 1999.

[9] A. Ferrari and P.R. Sala, *A New Model for Hadronic Interaction at Intermediate Energies for the FLUKA Code*, The MC93 international conference on Monte Carlo Simulation in High Energy and Nuclear Physics, Tallahassee, Florida, 1993, 277-288, World scientific, Singapore.

[10] A.J. Koning, M.B. Chadwick, *Microscopic Two-component Multistep Direct Theory for Continuum Nuclear Reactions*, Phys. Rev. C, 1997, 56, 970-99.

# HIGH AND INTERMEDIATE ENERGY NUCLEAR DATA FOR ACCELERATOR DRIVEN SYSTEMS – THE HINDAS PROJECT

**J.P. Meulders[1], H. Beijers[2], J. Benlliure[3], O. Bersillon[4], J. Cugnon[5], Ph. Eudes[6], D. Filges[7], A. Koning[8], J.F. Lecolley[9], S. Leray[10], R. Michel[11], N. Olsson[12], K.H. Schmidt[13], H. Schuhmacher[14], I. Slypen[1], H. Synal[15], R. Weinreich[16]**

[1]Institut de Physique Nucléaire, Université Catholique de Louvain, 1348 Louvain-la-Neuve, Belgium
[2]Kernfysich Versneller Instituut, Rijksuniversiteit Groningen, 9747 Groningen, The Netherlands
[3]University of Santiago de Compostela, 15706 Santiago de Compostela, Spain
[4]CEA-Bruyères-le-Châtel, Service de Physique Nucléaire, 91680 Bruyères-le-Châtel, France
[5]Institut de Physique B5, Université de Liège, 4000 Sart Tilman Liège 1, Belgium
[6]Subatech, Université de Nantes, Ecole des Mines de Nantes, IN2P3-CNRS, 44307 Nantes, France
[7]Forschungszentrum Jülich GmbH, Institut für Kernphysik, 52425 Jülich, Germany
[8]Nuclear Research and Consultancy Group, 1755 Petten, The Netherlands
[9]Laboratoire de Physique Corpusculaire de Caen,
IN2P3-CNRS/ISMRa et Université de Caen, 14050 Caen, France
[10]DAPNIA/SPhN CEA/Saclay, 91191 Gif-sur-Yvette, France
[11]Zentrum für Strahlenschutz und Radioökologie, Universität Hanover, 30167 Hanover, Germany
[12]Department of Neutron Research, Uppsala University, 75121 Uppsala, Sweden
[13]Gesellschaft für Schwerionenforschung mbH, 64291 Darmstadt, Germany
[14]Physikalisch Technische Bundensanstalt, 38116 Braunschweig, Germany
[15]Institute of Particle Physics, ETHZ, 8093 Zurich, Switzerland
[16]Paul Scherrer Institute, 5232 Villingen-PSI, Switzerland

## Abstract

The HINDAS project (High and Intermediate energy Nuclear Data for Accelerator driven Systems) is a three years project supported by the European Commission under the Fifth Framework Program. The gathering of 16 partners, both experimentalists as theoreticians, allows to measure the wealth of new nuclear reaction cross-sections in the energy range between 20 MeV and 2 GeV on 3 elements of crucial importance for ADS systems: Pb as a target element, U as an actinide and Fe as a shielding element. The new experimental data will help to benchmark the existing theoretical models or to improve them. The assembly of nuclear data tables on those elements will allow interpolating to other elements appearing to be important in the design and the construction of an European ADS demonstrator.

## 1. Introduction

The HINDAS project (High and Intermediate energy Nuclear Data for Accelerator driven Systems) is supported by the European Commission under the Fifth Framework Program (September 2000-August 2003) and involves 16 European laboratories. Its general objective is to obtain a complete understanding and modelling of nuclear reactions in the 20-2 000 MeV region, in order to build reliable and validated computational tools for the detailed design of the spallation module of an accelerator driven system. This essential goal can only be accomplished by means of a well-balanced combination of basic cross-section measurements, nuclear model simulations and data evaluations.

Therefore, three nuclides, Fe, Pb and U have been chosen which provide a sufficiently broad coverage of the periodic table and are representative of the target, structure and core materials of the ADS. Hence, not only a few of the top-priority materials are chosen but, more importantly, with detailed theoretical and experimental knowledge of these particular elements, the nuclear models present in the foreseen simulation codes of this project will be fine-tuned. These will be employed to generate nuclear codes and data libraries for the materials that are requested by the ADS community.

The measurements will be performed at six nuclear physics laboratories in Europe, where beams of proton, neutron and heavy ion (in conjunction with inverse kinematics) as well as relevant measurement are available.

There appear to be a transition region around 200 MeV for the theoretical models. In the 20-200 MeV region, the theoretical calculations include direct interaction, pre-equilibrium, fission and statistical models, all with many uncertainties. Above 200 MeV, the theoretical analysis includes the intra-nuclear cascade model together with fission and evaporation models. A similar transition appears at about the same energy in the experimental facilities and in the measuring techniques.

The HINDAS project is therefore divided in experimental as well as theoretical work packages, according to this energy limit. The detection techniques differ also substantially for neutrons, protons and residual nuclide production, which has motivated a further division of the work packages according to the detected nuclides. This paper presents these work packages with the different results that would be available at the end of the project.

## 2. Experimental work between 20 and 200 MeV

The experimental work in the intermediate energy range from 20 MeV to 200 MeV is condensed in 3 parts. The measurements of cross-sections of nuclear reactions induced by protons and neutrons on Fe, Pb and U targets cover 2 work packages and the measurement of residual nuclide production is the object of the third part. Those experiments will be performed at 4 European accelerators which allows to cover the entire energy range from 20 to 200 MeV for the proton beams and two of those facilities can produce monoenergetic neutron beams with time of flight facilities.

### *2.1 Light charged-particle production induced by neutrons or protons between 20 and 200 MeV (WP1)*

The measurement of double differential cross-sections of light charged-particles p, d, t, $^3$He and $\alpha$ induced by protons or neutrons on the different chosen targets will be obtained by measuring the energy spectra of each charged-particle over a large angular range from 15° to 160°. By integration over the angle, energy differential cross-sections are obtained at each angle, and by integration over the energy, angular differential cross-sections of the produced particle are deduced. The information contained in the double differential cross-sections is very stringent for theoretical models of nuclear

reactions, since the pre-equilibrium reactions have to be taken into account, in addition to the direct interaction contribution at the high energy part of the spectrum and the statistical evaporation component at the low energy side of the spectra.

The (p,*x*lcp) reactions on Pb and U will be measured by the partners of UCL, Subatech and LPC-Caen at 65 MeV at the CYCLONE cyclotron (UCL, Louvain-la-Neuve), and the same reactions on Fe, Pb and U at 135 MeV by the partners of Subatech, LPC-Caen and RuG at the KVI cyclotron (Groningen, The Netherlands) (see also N. Marie, this meeting). For these measurements, 8 triple telescopes (Si-Si-CsI) allow to measure the light charged-particles over their entire energy range (with low energy thresholds). Figure 1 shows a picture of the reaction chamber with the triple telescopes.

Figure 1. **The reaction chamber and the triple telescopes used in the (p,xlcp) reactions**

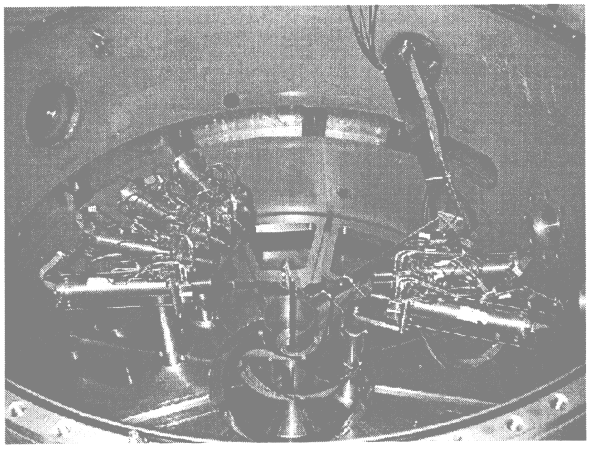

The (n,*x*lcp) reactions on Fe, Pb and U will be measured at 65 MeV at the CYCLONE cyclotron (UCL, Louvain-la-Neuve) (see also M. Kerveno, this meeting). Six ΔE-E telescopes (NE 102 plastic scintillator – CsI(Tl) detector) detect the charged particles produced by the neutrons on the target. The information from the telescopes coupled to the time of flight method with excellent time resolution (less than 1 ns) allows reconstructing, event by event, the energy spectra for each ejectile. Double differential cross-sections are obtained for the neutron mono-energetic peak (~63 MeV) and also for energies from the continuum of the neutron energy spectrum [1] (from 30 to 57 MeV).

The (n,*x*lcp) reactions on Fe and Pb at 100 MeV will be measured at The Svedberg cyclotron (UU, Uppsala) with a similar detection setup as for the proton induced-reactions. Partners of Subatech (Nantes), LPC-Caen and UU (Uppsala) are involved in these measurements ([2] and F.R. Lecolley, this meeting).

Finally, charged-particles multiplicities will be measured in proton-induced reactions on Fe, Pb and U in the energy range between 130 and 200 MeV by partners from RuG (Groningen).

### *2.2 Neutron production induced by neutrons and protons (WP2)*

Partners of UU and LPC-Caen study elastic neutron scattering (n,n), at 100 MeV for Fe and Pb [2]. Such data are important to determine the nuclear optical potential to high precision in an energy range where data are essentially lacking. With this model at hand, cross-sections for elastic scattering, which is the most important reaction channel in the moderation and transport of the source neutrons, can be

calculated. Moreover, the optical potential is a necessary component in the description of many other reaction channels, since it accounts for the behaviour of a neutron entering or emerging from a nucleus.

The measurements will be performed using a recently developed detector set-up, consisting of two identical detector sets, which can be arranged to cover, e.g., the 10-50 and 30-70 degree ranges. Each detector set consists of a front veto scintillator, a 1 cm thick plastic scintillator for conversion into recoil protons, two drift chambers with x-y position sensitivity for proton tracking, and an array of 12 large CsI detectors for proton energy measurement. Absolute cross-sections will be determined by comparison with the reasonably well-known neutron-proton scattering cross-section.

Furthermore it is proposed to study the feasibility of (n,*x*n) reactions on Pb at 100 MeV. Such experiments are difficult to perform, but information is of great importance to understand and improve quantum-mechanical multi-step direct and classical pre-equilibrium models, as well as statistical models built on multiple Hauser-Feshbach emission. The measurements will make use of part of the previously described set-up, together with an active target for conversion of the emitted neutrons into recoil protons. The active conversion target will be positioned outside the neutron beam, but close to the Pb target, to obtain a large solid angle for neutrons. The recoil protons will be traced by a couple of drift chambers, and finally the energy will be determined in the CsI detector array.

Finally, the measurement of double-differential spectra from (p,xn) reactions in Pb and U, using a 65 MeV proton beam will be performed by partners of LPC-Caen, Subatech and UCL. In these experiments the emitted neutrons will be detected by well-shielded NE213 neutron detectors, placed around the scattering centre to measure angular distributions. The neutron energy distribution will be determined using time-of-flight techniques. Neutrons will be distinguished from gamma-rays using the pulse shape discrimination properties of this kind of detectors.

### *2.3 Residual nuclide production induced by neutrons and protons and production of long-lived radionuclides (WP3)*

Reliable cross-sections for the production of residual nuclides by medium-energy proton- and neutron-induced reactions are essential for ADS to calculate the radioactive inventories of the spallation target, of structural materials and of ambient matter. Production of residual nuclides by GeV protons in thick or massive targets are a complex phenomenon the modelling of which needs to follow in detail the inter- and intra-nuclear cascades, the production and transport of primary and secondary particles. The spectra of primary and secondary particles strongly depend on the material irradiated as well as on geometry and depth inside the target. To calculate activation rates and radioactive inventories such calculated spectra have to be folded with the energy-dependent cross-sections of the underlying nuclear reactions for energies from thresholds up to the initial energy of the primary particles. Presently, there is no model or code available to predict the required cross-sections with an accuracy of better than a factor of two on the average. Therefore, one has to rely for the important nuclides on experimental cross-sections. Such experimental cross-sections are also needed if one tries to improve models and codes as a basis for validation.

Due to the importance of nuclear reactions of secondary particles, neutron-induced reactions will dominate the radionuclide inventory of the spallation target though the high-energy primary protons will significantly contribute. As a consequence, one needs cross-sections for both proton- and neutron-induced reactions for a reliable modelling of residual nuclide production over the entire energy range.

The data to be determined in this section will provide an experimental basis to calculate such inventories of the spallation target, of shielding and structural materials for an accelerator driven system a few minutes after shut-down as well as to validate theoretical work which is needed to

calculate the very short-lived radionuclides which make up an essential part of the spallation target during operation of a facility. With respect to the long-term behaviour and the final disposal of spallation targets and structural materials the precise modelling of long-lived radionuclides will be essential. Up to now, there are no inventory calculations which take into account long-lived radionuclides, mainly due to the lack of respective cross-sections.

For the modelling of radionuclide inventories it will be sufficient as a first approximation to have neutron-cross-sections up to 200 MeV. Measurements of residual nuclide production induced by neutrons between 30 and 180 MeV are foreseen. For proton-induced reactions one needs the complete excitation functions up to the energy of the primary beam. The latter do exist from recent work of our collaboration for most relevant target elements [3]. Measurement of production cross-sections of long-lived radionuclides via accelerator mass spectrometry (AMS) after chemical separation (partners ZSR and ETHZ) will be performed between 40 and 75 MeV.

## 3. Experimental work between 200 and 2 000 MeV

The aim of this work will be to collect high quality data and compare them with the state-of-the-art nuclear models. Data will be either measured in the framework of the project or have already been measured by the partners but not yet fully interpreted. In any case, they will be delivered as a ready-to-use file to be included in international data banks.

Particular attention will be paid to the impact of the new data for applications. Calculations of several quantities important in the design of ADS target or window will be performed using standard High Energy Transport Codes. In these codes the elementary cross-sections generated by the old nuclear models will be replaced either by the most recent version of models from J. Cugnon validated on data from our collaboration or, when possible and if models are not yet reliable enough, directly by the measured cross-section. Errors or uncertainties due to the use of the standard codes will be assessed.

### *3.1 Light charged-particle production (WP4)*

This part will be devoted to the collection of data concerning the production of light charged-particles. These data are important to probe the high-energy nuclear models in which the competition between neutrons and charged-particles, and the emission of composite nuclei (deuterons, alphas) are not yet treated satisfactorily. Moreover, the production yields of hydrogen and helium are essential for estimation of gas production in the window or structure materials of an ADS.

Production cross-sections for hydrogen and helium are being measured using a $4\pi$ silicon ball detector. So far, experiments have been performed at 0.8, 1.2, 1.8 and 2.5 GeV on several targets [4] and further experiments are foreseen. These measurements are also performed in coincidence with neutron multiplicity distributions. This allows studying the production rates of protons and alphas as a function of the excitation energy in the nucleus remaining at the end of the Intra-Nuclear Cascade stage. All these data will be analysed and compared to high-energy nuclear models.

Implications of the results from this experiment for gas production in some of the components of an ADS will be assessed, for instance on the lifetime of the window or on structure materials.

Moreover, a new magnetic spectrometer able to measure with a high resolution double-differential cross-sections for the production of light charged-particles (induced by protons) in coincidence with low energy neutrons will be designed.

Figure 2. **The Berlin ball detector system**

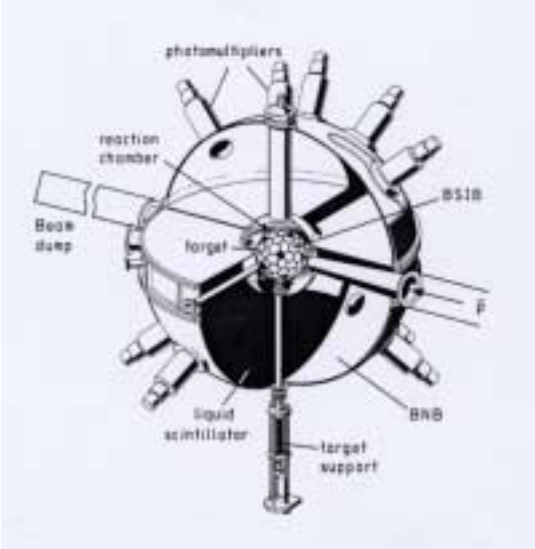


### *3.2 Neutron production induced by protons in thin and thick targets (WP5)*

In this work-package, different types of neutron production data measured recently by the partners in both thin and thick targets will be collected, cross compared and compared with models.

Up to recently, very little high-quality data concerning double-differential cross-sections of neutron production were existing above 800 MeV and below there were significant discrepancies between different sets of data. Partners of CEA-Saclay, CEA-Bruyères and LPC-Caen have measured neutron energy spectra and complete angular distributions using two complementary experimental techniques: time-of-flight for the low energy part of the neutron spectrum and neutron-proton scattering on a liquid hydrogen converter with a magnetic spectrometer measuring the momentum of the recoiling proton for high energy neutrons. This has allowed to obtain energy spectra of (p,xn) reactions with a high resolution from 2 MeV to the incident energy, on several targets at 800, 1 200 and 1 600 MeV [5]. The same apparatus was used to measure neutron energy spectra from thick targets with different length and diameters.

Partner from FZJ has participated to a collaboration using a $4\pi$ liquid scintillator detector able to measure event-wise the multiplicity of neutrons up to 150 MeV on both thin and thick targets of different length and diameter for incident proton energies of 0.4, 0.8, 1.2, 1.8 and 2.5 GeV over a wide range of structural and target materials for ADS applications [4]. The neutron multiplicity distribution in thin targets reflects the excitation energy distribution of the nucleus remaining at the end of the Intra-Nuclear Cascade stage and is therefore important to understand the reaction mechanism. The average value of the neutron multiplicity distribution in thick targets is directly interesting for applications.

The measurements performed by FZJ and CEA-Saclay, CEA-Bruyères, LPC-Caen are complementary both for technical (energy range of the measurements) and physics reasons (high-energy neutrons test the intra-nuclear cascade stage while low energy neutrons probe the evaporation stage). So far, no coherent simultaneous analysis of both experiments has been done. This will be the goal of this work-package in which, for example, the average multiplicity distributions measured with the neutron ball will be compared to those inferred from the integration of the double-differential

cross-sections; the secondary reactions induced in the neutron scintillator detector will be assessed using results of the high energy neutron spectrum measured by the double-differential cross-section experiment, etc.... Comparisons with the same high energy nuclear models for thin targets, the same high-energy transport codes for thick targets, taking into account the rather complex experimental acceptance of both experiments, will be performed. Results will be used to assess the remaining deficiencies in the codes to be improved in the theoretical section of the HINDAS project. Simulation of thick target results will also be realised. Direct applications of the thick target experiments such as average neutron multiplicities or high-energy neutron leakage for shielding estimation will be discussed.

### *3.3 Residual nuclide production in inverse kinematics (WP6)*

In spallation reactions of heavy nuclei induced by protons of about 1 GeV, mostly short-lived radioactive nuclei are produced. The spallation residues are stopped inside the target. They decay towards stable isobars predominantly by beta decay. After irradiation, long-lived radioactive residues are identified in mass and atomic number by gamma spectroscopy and by accelerator mass spectrometry. These experiments provide reliable and comprehensive data on cumulative yields, from which long-lived activities and final element yields can be deduced. In addition, these techniques allow for measurements over a large range of bombarding energies. A previous inter-comparison with available data has revealed that the calculations with nuclear-reaction models are not realistic enough, but it is difficult to pin down the deficiencies of the models on the basis of cumulative yields. For this purpose, a complete systematic of isotopic production cross-sections emerging from the nuclear reaction is urgently needed.

In particular for proton energies above 200 MeV, a substantially different technique, based on the use of inverse kinematics, has been developed recently which allows identifying all short-lived radioactive nuclides produced as spallation residues prior to beta decay. Heavy nuclei are provided as projectiles, impinging on a liquid-hydrogen target. The spallation residues are identified in-flight in a high-resolution magnetic spectrometer. These experiments allow a much more direct insight into the reaction mechanism than experiments in normal kinematics and therefore are best suited to improve nuclear-reaction models which are known to be unable to reproduce available data. In addition, this technique allows to determine the kinetic energies of the spallation residues [6], an information of highest importance for estimating radiation damages in structure material of an ADS. That means that these experiments provide unique and valuable information which complements the results obtained in normal kinematics. Due to electronic interactions in the spallation target, the primary protons loose energy and induce nuclear reactions in a wide energy range. However, the higher energies are particularly important for residual-nuclide productions, since more than 75% of the primary protons of 1 GeV undergo nuclear reactions in the spallation source in an energy range above 700 MeV. Additional measurements with a liquid deuterium target are aimed to provide information on spallation reactions induced by neutrons.

The experiments in inverse kinematics and the data analysis being rather complex, only few projectile species and energies can be investigated. Therefore, the measurements are restricted to $^{208}$Pb, $^{238}$U and $^{56}$Fe at 1 A GeV and partly at 500 A MeV. During the 3-year period of the project, final data on $^{208}$Pb and $^{238}$U will be available. It is expected that the full isotopic distributions and kinetic energies obtained in inverse kinematics in combination with detailed excitation functions of specific reaction products obtained in normal kinematics provide sufficient information to develop substantially improved nuclear-reaction models which can then be used in transport codes to predict realistic energy-integrated production yields in thick targets.

Finally, a new experimental technique will be developed to also measure neutrons and light charged-particles in inverse kinematics. This will allow establishing coincidences between these particles and the heavy residues, an information still more relevant for modelling the nuclear reaction correctly.

Calculations of the activities, radiotoxicities and element distributions in a realistic lead spallation target will be performed using transport and evolution codes. The elementary cross-sections generated by the old nuclear models will be replaced either by the most recent version of models from J. Cugnon, or directly by the measured production yields on Pb at 1 000 MeV, extrapolated at non-measured energies using the energy dependence of the excitation functions measured in WP3.

## 4. Theory and evaluation

For research on accelerator-driven systems, cross-sections for the important materials need to be known for ALL possible outgoing channels, outgoing channels, outgoing energies and angles. This total amount of required information is so large that experiments alone can never cover the nuclear data needs for ADS. To fill this gap, the data are simulated computationally, with the help of theoretical reaction models. The development of this simulation is done in close correspondence with the experiments: adjustable parameters of the theoretical models are adjusted in such a way that the latter reproduce the measurements as closely as possible. The critical assumption is then that the models can also be used in areas where no measurements exist. Hence, the actual provision of nuclear data in a form usable for ADS design will be done in two work-packages

- Nuclear data libraries, improved and extended up to 200 MeV, based on nuclear models.
- Intra-nuclear cascade models and codes for the higher energies.

### *4.1 Nuclear data libraries and related theory (WP7)*

This part concerns nuclear model calculations for a theoretical analysis of the between 20 and 200 MeV and predictions for the unmeasured channels for energies up to 200 MeV. In combination, this will be used to construct complete nuclear data libraries for $^{56}$Fe, $^{208}$Pb and $^{238}$U up to 200 MeV, which will show a clear improvement over all other existing nuclear data files and methods [7].

Theoretical calculations will be performed with a variety of nuclear models at NRG-Petten and at CEA-Bruyères-le-Châtel. The new model code system will be extended to include a proper treatment of all channels precisely. Coupled-channels optical models will be constructed for the simulation of the elastic and inelastic channels, not only for the total (angle-integrated) cross-sections, but also for the angular distributions. For the continuum reactions, complete outgoing energy and angular spectra will be included for all light particles. These will be predicted, and compared with the new measurements, using quantum-mechanical multi-step direct (MSD) and classical pre-equilibrium models that include novel models for microscopical particle-hole level densities and the optical models. Multiple pre-equilibrium emission beyond the second step will be included for the highest incident energies. Complete evaporation of the residual nuclides is accounted for by means of multiple Hauser-Feshbach emission that includes competition of all possible outgoing particle channels and fission, while conserving energy, angular momentum and parity. Simultaneously with the double-differential spectra, the calculated residual production cross-sections will be compared with the experiments as described in WP3. Both types of observables must be described by one and the same calculation. High-energy fission will also be included by means of an extension of the Brosa model.

All possible nuclear reactions will be evaluated simultaneously, in order to ensure flux conservation and energy balance. The results will be compared with the American GNASH code.

The calculated results will be processed automatically into the ENDF6-format. The results will be combined with the data below 20 MeV to come to one consistent final library. If the existing data file below 20 MeV turns out to be inadequate, the cross-sections will be improved in the low energy regime as well to ensure a smooth transition from low to high energies. All the nuclear data will be stored in the common ENDF-6 format and will be checked according to a standard QA-system. As basis for the new high-energy evaluations, the European JEFF library will be used.

### *4.2 High-energy models and codes (WP8)*

The high energy codes, although globally rather successful, suffer from some deficiencies. Both their inter-comparison and the comparison with existing experimental data reveal, in some identified regime, discrepancies which are beyond the accuracy required by the engineers working on projects of ADS or spallation sources. These observations call for improvements of the physics already included in the cascade codes (in-medium corrections, Pauli principle, mean field dynamics,...), of the evaporation codes (level densities) and of fission codes (viscosity, evaporation-fission competition at high excitation energy) [8]. These improvements are part of the specific theoretical task in this project. They will be realised in successive steps at Ulg-Liège.

The first step will consist of improving the existing codes by including physics aspects not included so far and by refining some of the physics which is already implemented. For the most recent intra-nuclear cascade (INC) code, this concerns a proper description of the nuclear surface, an improvement of Pauli blocking, which present too much fluctuations, and refinements of the in-medium corrections. For the evaporation codes, the first step will involve a careful examination of the input data and an advanced development of the fission model at high excitation energy, taking advantage of the forthcoming measurement of the fission component in reverse kinematics (see WP6). The improvements will be inspired by the most recent theoretical progress in nuclear dynamics far from equilibrium.

The second step aims at a validation of the improved codes (and other standard codes). An extensive comparison with the neutron differential cross-sections measured at SATURNE (800 to 1 600 MeV) and with the neutron multiplicities and light charged-particle spectra measured at Jülich (WP5) will be performed, for both thin and thick target data. In addition, an extensive comparison with the experimental residue production data to be provided by WP6 will be realised.

As a third step, a new improvement of the codes will be undertaken, if necessary. This work will involve an adjustment of the introduced parameters to describe less well known physics aspects, like the parameters regulating the coupling between the INC and evaporation codes and some parameters of the fission model, especially viscosity.

The final goal will consist in the elaboration of a version of a high-energy transport code including these new simulation tools. This version could be tested on the thick target data generated by this project.

*Acknowledgements*

All partners thank the European Commission for supporting the project HINDAS under contract number FIKW-CT-2000-00031.

## REFERENCES


[1] S. Benck, I. Slypen, J.P. Meulders, V. Corcalciuc, *Light Charged Particle Emission Induced by Neutrons With Energies Between 25 and 65 MeV On Oxygen*, Eur. Phys. J. A., 1998, 3, 149-164.

[2] S. Dangtip, A. Ataç, B. Bergenwall, J. Blomgren, K. Elmgren, C. Johansson, J. Klug, N. Olsson, G. Alm Carlsson, J. Södenberg, O. Jonsson, L. Nilsson, P.-U. Renberg, P. Nadel-Turonski, C. Le Brun, F.-R. Lecolley, J.-F. Lecolley, C. Varignon, Ph. Eudes, F. Haddad, M. Kerveno, T. Kirchner, C. Lebrun, *A Facility For Measurements Of Nuclear Cross-sections For Fast Neutron Cancer Therapy*, Nucl. Instrum. Meth. Phys. Res. A, 2000, 452, 484-504.

[3] M. Gloris, R. Michel, F. Sudbrock, U. Herpers, P. Malmborg, B. Holmqvist, *Proton-induced Production of Residual Nuclei in Lead at Intermediate Energies*, Nucl. Instrum. Meth. Phys. Res. A, 2001, in press.

[4] A. Letourneau, J. Galin, F. Goldenbaum, B. Lott, A. Péghaire, M. Enke, D. Hilscher, U. Jahnke, K. Nünighoff, D. Filges, R.-D. Neef, N. Paul, H. Schaal, G. Sterzenbach, A. Tietze, *Neutron Production in Bombardments of Thin and Thick W, Hg, Pb Targets by 0.4, 0.8, 1.2, 1.8 and 2.5 GeV protons*, Nucl. Intrum. Meth. Phys. Res. B, 2000, 170, 299-322.

[5] X. Ledoux, F. Borne, A. Boudard, F. Brochard, S. Crespin, D. Drake, J.C. Duchazeaubeneix, D. Durand, J.M. Durand, J. Fréhaut, F. Hanappe, L. Kowalski, F.R. Lecolley, F. Lefebvres, R. Legrain, S. Leray, M. Louvel, E. Martinez, S.I. Meigo, S. Ménard, G. Milleret, Y. Patin, E. Petitbon, F. Plouin, P. Bras, L. Stuttge, Y. Terrien, J. Thun, M. Uematsu, C. Varignon, D.M. Whittal, W. Wlazlo, *Spallation Neutron Production by 0.8, 1.2 and 1.6 GeV Protons on Pb Targets*, Phys. Rev. Lett., 1999, 82, 4412-4416.

[6] W. Wlazlo, T. Enqvist, J. Benlliure, K.-H. Schmidt, P. Armbruster, M. Bernas, A. Boudard, S. Czajkowski, R. Legrain, B. Mustapha, M. Pravikoff, C. Stephan, J. Taieb, L. Tassan-Got, C. Volant, *Cross-sections of Spallation Residues Produced in 1 A GeV $^{208}$Pb On Protons Reactions*, Phys. Rev. Lett., 2000, 84, 5736-5740.

[7] A.J. Koning, J.-P. Delaroche, O. Bersillon, *Nuclear Data For Accelerator Driven Systems: Nuclear Models, Experiments and Data Libraries*, Nucl. Instrum Meth. Phys. Res. A, 1998, 414, 49- 67.

[8] J. Cugnon, C. Volant, S. Vuillier, *Improved Intranuclear Cascade Model For Nucleon-nucleus Interactions*, Nucl. Phys. A, 1997, 620, 475-509.

# A STUDY ON BURNABLE ABSORBER FOR A FAST SUB-CRITICAL REACTOR HYPER

**Yong Hee Kim, Won Seok Park**
Korea Atomic Energy Research Institute
P.O. Box 105, Yusong, Taejon, 305-600, Korea

**Jong Seong Jeong**
Department of Nuclear Engineering, Seoul National University
Shinrim-dong Kwanak-ku Seoul 151-742, Korea

## Abstract

This paper is concerned with development of burnable absorber technologies for an accelerator driven system (ADS) with fast neutron spectrum, HYPER (Hybrid Power Extraction Reactor). Concerning the ADS loaded with TRUs (Transuranic Elements), one of the major problems is a large burn-up reactivity swing and the consequent unfavourable slanting of the radial power distribution over a depletion period. In order to reduce the reactivity drop during core burn-up, $B_4C$ is introduced as a burnable absorber and its efficacy is evaluated for the HYPER system. Taking into account the radioactive TRU fuel, the inner surface of the fuel clad is coated with a thin $B_4C$ layer. Two concepts of the burnable absorber application are considered, homogeneous and heterogeneous loading of $B_4C$. In the homogeneous application, $B_4C$ is used in all fuel rods, while the burnable absorber is utilised only in the outer zone of the core in the heterogeneous loading. The burn-up characteristics of the HYPER cores with and without the $B_4C$ burnable absorber are analysed with a Monte Carlo code, called MCNAP.

## 1. Introduction

In Korea, an accelerator driven system (ADS), which is called HYPER (Hybrid Power Extraction Reactor) is currently under development for transmutation of TRUs (Transuranic Elements) [1]. Concerning the uranium-free fast reactors like HYPER, one of the big problems is a very large reactivity swing, regardless of the sub-criticality of the core. In an ADS, a large burn-up reactivity swing means a large reservation of the proton beam current. This large reserved proton current may result in several unfavourable safety features as well as adverse impacts on the economics of the system. Also, another concern associated with the large reactivity change is a one-way change of the radial power distribution during depletion of the core. To resolve this problem, an on-power refuelling concept, as in CANDU, was studied previously for HYPER [1]. However, the on-power refuelling makes the system fairly complex and may cause serious engineering concerns.

Several types of burnable absorbers such as boron, gadolinium, and erbium are successfully used to suppress the initial excess reactivity and to control the power distribution in thermal reactors like PWRs [2]. Regarding the critical fast reactors such as LMR (Liquid Metal Reactor), poisoning the core with a burnable absorber is not used to control the reactivity. This is mainly because the excess reactivity in conventional LMRs is fairly small due to self-generation of fissile elements and thus the burn-up reactivity swing can be easily controlled by control rods. Of course, it is well recognised that there is no effective burnable absorber for fast neutron systems due to small neutron capture cross-sections. When it comes to the fast-neutron ADS loaded with TRUs, however, the situation is quite different from those of the conventional critical thermal and fast reactors. Basically, any excess reactivity, which should be suppressed by external control mechanisms, should not be allowed in ADS in order to guarantee its surmised advantages. Consequently, control rods or absorber-containing coolant cannot be used to control the reactivity of an ADS. Thus, fixed burnable absorbers, if any, could only be utilised as the reactivity control mechanism for ADS.

Previously, Stone *et al.* [3] studied a dual spectrum core to reduce the reactivity swing of the ATW core, where a thermal spectrum zone is placed in the periphery of the core and $^{237}$Np and $^{241}$Am are loaded in the thermal region. They showed that the reactivity swing could be reduced by a factor of 2 in the dual spectrum ATW. However, the smaller reactivity change in the modified ATW is mainly due to the reduced power density. In addition, the dual spectrum core may lead to a large power peaking in the interface region between hard and soft spectrum regions.

The simplest way to reduce the reactivity swing is to adopt a low power density core. However, a low power density needs a large core volume, thus it is not favourable from the economics point of view. Recently, Hejzlar *et al.* [4] studied burnable absorbers for a critical Pb-Bi-cooled transmutation reactor. They evaluated various candidate materials such as B, Re, Hf, Gd, Er, etc. They showed that $^{10}$B has the largest neutron capture cross-sections and can reduce the reactivity swing a little. Finally, they discarded the burnable poison option, in favour of excess reactivity compensation through control rods.

In this paper, we have re-evaluated the potential of $^{10}$B as a burnable absorber for the sub-critical HYPER core to reduce the burn-up reactivity swing and also to control the radial power distribution. All calculations are performed with a Monte Carlo code, MCNAP [5], which was developed at Seoul National University, Korea. It is worthwhile to note that MCNAP has its own built-in depletion routine

## 2. Burnable absorber for HYPER

### *2.1 The HYPER core*

HYPER is a Pb-Bi-cooled ADS under development at KAERI with the aim of transmuting both TRUs and LLFPs such as $^{99}$Tc and $^{129}$I. The HYPER system is rated at 1 000 $MW_{th}$ thermal power and the minimum required sub-criticality is $k_{eff}$ = 0.97. Figure 1 shows a schematic configuration of the evolving HYPER core. In HYPER, a linear accelerator produces the proton beam of 1 GeV and the proton impinges on the Pb-Bi target in the core central region, generating about 28.84 spallation neutrons a proton. The proton beam is delivered to inside of the core through a beam tube to maximise the source neutron importance and also to obtain favourable axial power distribution. For emergency, 3 locations are reserved for safety zones. The fuel blanket region is divided into 3 TRU enrichment zones (low, medium, high) to obtain acceptable radial power distribution. The low and high TRU fuels are loaded in the innermost and outermost zones, respectively.

A unique feature of the HYPER core is transmutation of $^{99}$Tc and $^{129}$I in a localised thermal neutron zone. Inner region of the FP (Fission Product) assembly is composed of I and moderator ($CaH_2$) rods to produce thermal neutron and $^{99}$Tc-is placed in the peripheral region to block the thermal neutron leakage into the neighbouring fuel assemblies [6]. Currently, two fuel types are considered for HYPER, one is the TRU-Zr metal and the other one is the TRU-Zr dispersion fuel, where TRU-Zr particles are dispersed in Zr matrix. In this work, the dispersion fuel is assumed. Spent fuels from PWRs of 33 GWD/MTU burn-up, after 30-year cooling time, are reprocessed with a pyrochemical processing and then recycled into the HYPER core. In the present work, a uranium removal rate of 99.9% is assumed. Consequently, the HYPER core is not completely free from uranium elements, instead, uranium occupies about 9 w/o in the fuel as shown in Table 1.

Table 1. **Feed fuel composition in weight percent (33 GWD/MTU, 30-year cooling)**

| Isotopes | Weight percent (w/o) |
|---|---|
| $^{234}$U | 0.2000E-2 |
| $^{235}$U | 0.7894E-1 |
| $^{236}$U | 0.3840E-1 |
| $^{238}$U | 0.8920E+1 |
| $^{237}$Np | 0.4449E+1 |
| $^{238}$Pu | 0.9909E+0 |
| $^{239}$Pu | 0.4756E+2 |
| $^{240}$Pu | 0.2168E+2 |
| $^{241}$Pu | 0.2689E+1 |
| $^{242}$Pu | 0.4101E+1 |
| $^{241}$Am | 0.8649E+1 |
| $^{242m}$Am | 0.3868E-2 |
| $^{243}$Am | 0.7591E+0 |
| $^{243}$Cm | 0.1207E-2 |
| $^{244}$Cm | 0.6604E-1 |
| $^{245}$Cm | 0.7321E-1 |
| $^{246}$Cm | 0.8515E-3 |

Figure 1. **Configuration of the Pb-Bi-cooled HYPER core (183 fuel assemblies)**

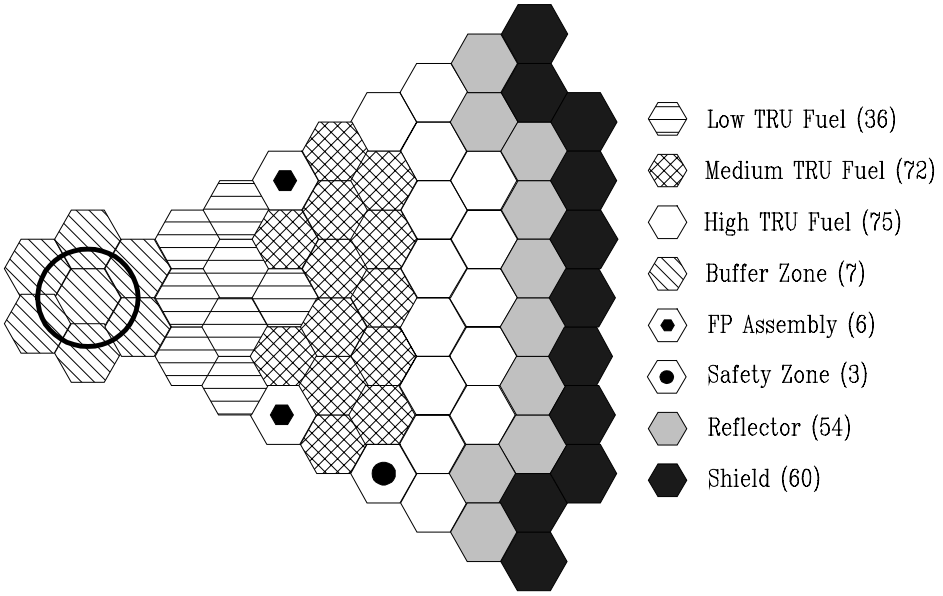


### *2.2 $B_4C$-coated cladding*

In order for a material to be an effective burnable absorber, its neutron capture cross-section should be much larger than those of fuel elements. Also a neutron capture of a burnable absorber should not generate nuclides with large capture cross-sections and at the same time daughter nuclides should be naive in terms of radiotoxicity. Taking into account the above constrains on burnable absorbers, $^{10}$B seems to be the best candidate for the burnable absorbing material of the HYPER core.

$^{10}$B absorbs a neutron through $(n,\gamma)$ or $(n,\alpha)$ reaction. The $(n,\alpha)$ reaction, i.e. helium production reaction, is an exothermic process:

$$B_5^{10} + n_0^1 \rightarrow Li_3^7 + He_2^4 + Q,$$

where Q is about 2.79 Mev for thermal neutrons and is a little larger in fast neutron systems. Table II compares one-group effective cross-sections of boron and plutonium isotopes in the HYPER fuel assembly. As shown in Table 2, the capture cross-section of $^{10}$B is a little larger than the fission cross-section of $^{239}$Pu, the major fissile isotopes of the TRU fuel. Neutron absorptions of $^{11}$B and Li-7 are negligibly small. Table 2 shows that the depletion rate of $^{10}$B is a little faster than that of $^{239}$Pu even in very hard neutron spectrum.

Table 2. **One-group effective cross-sections of boron and plutonium isotopes in the HYPER core**

| | $\sigma(n,\gamma)$ **, barn** | $\sigma(n,\alpha)$ **, barn** | $\sigma_f$ **, barn** |
|---|---|---|---|
| $^{10}$B | 2.978E-4 | 2.307 | – |
| $^{11}$B | 4.468E-5 | – | – |
| $^{7}$Li | 3.097E-5 | – | – |
| $^{238}$Pu | 0.631 | – | 1.089 |
| $^{239}$Pu | 0.397 | – | 1.693 |
| $^{240}$Pu | 0.427 | – | 0.358 |
| $^{241}$Pu- | 0.375 | – | 2.296 |

The $(n,\alpha)$ reaction of $^{10}$B is exothermic and produces helium gas as well as Li-7. Therefore, care must be taken, when using $^{10}$B as a burnable absorber in nuclear reactors. It is well known that direct mixing $^{10}$B with fuel impairs the fuel integrity since the fuel swelling is enhanced due to helium gas and liquid-phase Li-7. To overcome this limitation, Westinghouse has developed a burnable absorber technology for PWRs, where the fuel rod is coated with $ZrB_2$ [2], and achieved successful performance. Thickness of the $ZrB_2$ layer is about 0.002 cm.

Unfortunately, it is not easy to use the Westinghouse approach directly for HYPER, since the TRU fuel of HYPER is very radioactive. Therefore, we have used a slightly different option, i.e. $B_4C$-coated cladding, where the inner surface of cladding is coated with $B_4C$. In the present work, $B_4C$ is used, instead of $ZrB_2$, since it is easily available and has more boron elements than $ZrB_2$. Thickness of the $B_4C$ layer is 0.0009 cm or 0.0012 cm. In the natural boron, abundances of $^{10}$B and $^{11}$B are 19.8% and 80.2%, respectively. In order to maximise the $^{10}$B loading, it is assumed that $^{10}$B is enriched up to 90% atomic percent in this paper. Figure 2 shows the burnable absorber rod for the HYPER core. It should be noted that two cutback regions, where the absorber is not applied, are adopted to flatten the axial power distribution.

Figure 2. **Fuel rod with B4C-coated cladding in HYPER**

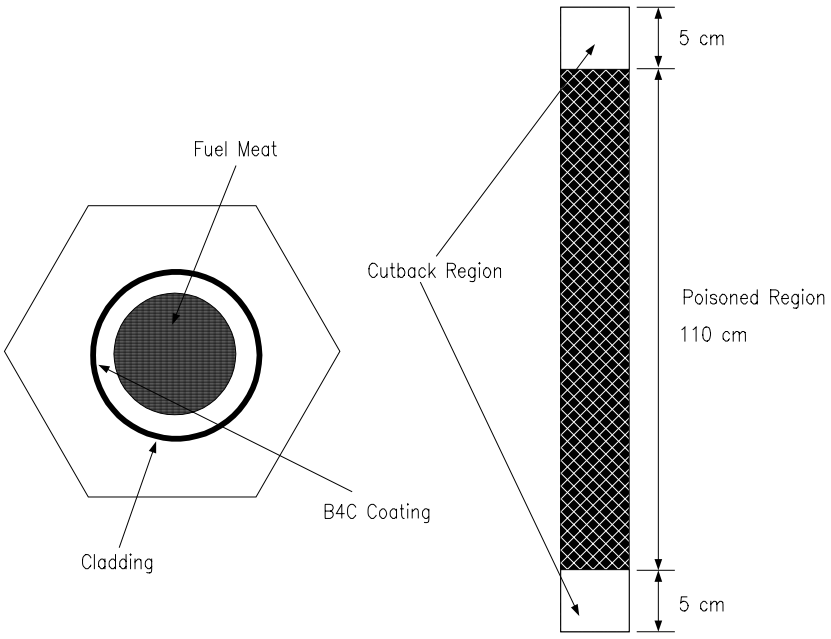

## 3. Numerical results

The performance of the burnable absorber in Section 2.2 is evaluated in terms of spallation neutron multiplication and radial power distribution. Two types of burnable absorber applications are compared with the unpoisoned reference HYPER core, one is a homogeneous loading of $B_4C$ (HYPER-HBA) and the other one is a heterogeneous loading (HYPER-OBA). All fuel rods have the $B_4C$ coating in the homogeneous application, while the burnable absorber is used only in middle and outer zones of the core in the heterogeneous loading of $B_4C$. In HYPER-HBA, a $B_4C$ layer of 0.0012 cm thickness is used and a little thinner layer, 0.0009 cm, is utilised in HYPER-OBA to enhance the $^{10}B$ depletion rate. Numerical tests are conducted for the initial core, which has the largest burn-up reactivity swing.

All calculations were done with the MCNAP code for a 3-dimensional model of the HYPER core, where each assembly was homogenised by using the volume-weighting method and treated as an independent cell and the active core was divided into 6 segments in the axial direction. The zone-wise TRU enrichments were adjusted such that the initial $k_{eff}$ should equals 0.97 at the beginning of cycle (BOC) and also the radial power distribution should be acceptable. The radial power distribution is not optimised since the objective of this work is to evaluate the potential of the $B_4C$ burnable absorber. Table 3 shows TRU enrichments of the three cores, $k_{eff}$ values, and corresponding multiplication factors at BOC. TRU inventory of HYPER-HBA is about 24% larger than that of the reference core and it is increased by about 13.4% in HYPER-OBA. Initial sub-criticality was determined by a critical mode calculation and the depletion calculations were based on the fixed-source mode with a 30-day time step. In the fixed-source calculations, a generic source distribution was assumed.

Table 3. **Zoning of TRU enrichment and initial $k_{eff}$**
**(L = Low, M = Medium, H = High)**

| Core type | TRU enrichment (w/o) | $^{10}B$ (kg) | $k_{eff}$ | Multiplication ($M_s$) |
|---|---|---|---|---|
| Reference | L (19.18), M (24.70), H (30.60)<br>TRU Loading: 2774.58 kg | – | 0.96975<br>(0.0010)[a)] | 25.281<br>(0.043)[a)] |
| HYPER-HBA | L (22.63), M (29.07), H (36.18)<br>TRU Loading: 3436.46 kg | 21.858 | 0.96940<br>(0.0010) | 21.547<br>(0.050) |
| HYPER-OBA | L (19.22), M (28.15), H (34.05)<br>TRU Loading: 3146.11 kg | 13.176 | 0.97021<br>(0.0011) | 21.946<br>(0.043) |

[a)] Standard deviation.

The burn-up reactivity drop was evaluated for each core. Currently, the MCNAP code cannot do both critical and fixed-source calculations for a burn-up point. Therefore, the reactivity change over a 180-day depletion was indirectly evaluated in terms of a spallation neutron multiplication factor ($M_s$). In this paper, $M_s$ is defined as 1 plus the number of fission neutrons produced by a spallation neutron in the fuel blanket. In a critical reactor, the multiplication of a fission source neutron can be represented by $1/(1-k_{eff})$. However, the spallation neutron multiplication, in sub-critical reactors, is quite different from the multiplication of a fission source in a critical reactor. Readers who are interested in the multiplication of a spallation neutron in ADS are referred to our work [7]. Although the source neutron multiplication cannot exactly represent the reactivity, it can be generally said that the larger k-eff value, the larger $M_s$. As far as the accelerator power is concerend, $M_s$ has more practical meaning than k-eff for a sub-critical reactor, since a large $k_{eff}$ does not always mean a high multiplication of the spallation neutron. Table 3 confirms this argument; $k_{eff}$ is almost 0.97 in all the three cores, even though the multiplication factor varies fairly significantly. It should be noted that the proton beam current, required for a constant power

of the core, is directly determined by the $M_s$ value, not by $k_{eff}$.

Figure 3 shows the evolution of the spallation neutron multiplication during a 180-day burn-up period for the reference core, HYPER-HBA, and HYPER-OBA. Figure 4 compares the proton beam currents required for 1 000 $MW_{th}$ fission power. It is observed that multiplication of source neutrons at BOC is quite different from each other, despite that the $k_{eff}$ values are almost the same. Specifically, $M_s$ of HYPER-HBA is significantly smaller that that of the reference core, while HYPER-OBA has a little larger $M_s$ than HYPER-HBA. The small multiplication factor of HYPER-HBA is due to the fact that a significant fraction of the spallation neutrons, which are generated in the central target zone, is absorbed by $B_4C$ before they give birth to their descendants. Meanwhile, the relatively high multiplication factor of HYPER-OBA is because the inner zone is poisoned with burnable absorbers, thus the probability for a source neutron to be parasitically absorbed is lower than in HYPER-HBA.

One can see a rapid decrease of the $M_s$ values, in Figure 3, at the early period of depletion. This is due to the fact that $M_s$ is proportional to $1/(1-k_{eff})$ and partly because fission products are accumulated in the core. In Figure 3, it is clearly observed that HYPER-HBA has the smallest burn-up reactivity swing among the three cases. However, if the cycle length is short, e.g. 120 days, this smaller reactivity swing has little advantage since larger proton beam current is required, as shown in Figure 4. On the contrary, for a 180-day operation, it is worthwhile to note that total accelerator power is almost comparable to the reference case and the peak beam current is smaller than that of the unpoisoned core. This advantage is attributed to the smaller reactivity swing of the HYPER-HBA core.

For HYPER-OBA, one can note that change in $M_s$ is a little smaller than that of the reference due to reduced reactivity swing. In addition, the $M_s$ value of HYPER-OBA is a little larger except in the vicinity of BOC, compared with the reference case. From Figure 4, it is clear that HYPER-OBA needs smaller integrated accelerator power and also smaller peak beam current than the reference HYPER core, if the depletion period is greater than 60 days. Figures 3 and 4 indicate that HYPER-OBA has slightly larger reactivity swing than HYPER-HBA. This is mainly because the amount of $B_4C$ in HYPER-OBA is about a half of that of HYPER-HBA. If thickness of the $B_4C$ layer is increased, the reactivity swing of HYPER-OBA would be reduced further.

Figures 5 to 7 show the normalised radial power distributions at three burn-up points, 0-day, 120-day, and 180-day. In the reference core (see Figure 5), it is seen that slanting of the radial power distribution is very significant; the inner zone power increased considerably during the burn-up periods, while the outer zone power decreased. Especially, power density in the innermost fuel assembly increased by a factor of 1.256 (120-day operation) or 1.394 (180-day operation). Currently, the maximum allowable radial peaking factor is set to 1.50 for the HYPER core. Consequently, for a relatively long cycle length, e.g. 180-day, the initial powers of the innermost fuel assemblies should be much lower than the current values. Of course, the inner zone powers should also be lowered even for a 120-day operation, since the peaking factor of the inner zone fuel assemblies might be fairly large. This result confirms that radial power distribution control is a big concern in a sub-critical core with large reactivity swing. In addition, too large change in the radial power distribution is not favourable from the discharge burn-up distribution.

For HYPER-HBA in Figure 6, a similar behaviour can be observed as in Figure 5. On the other hand, one can see quite different trend in the HYPER-OBA core. As shown in Figure 7, the HYPER-OBA core has also a one-way change in the radial power distribution, i.e. monotonic increase in the inner zone and decrease in the outer zone. However, the power increasing rate of the innermost assembly is significantly suppressed, compared with the reference core. In HYPER-OBA, the power of the innermost assembly is increased by a factor of 1.229 (120-day operation), or 1.300 (180-day

operation), respectively. This is because the $^{10}B$ burnable absorbers burn in the middle and outer zones. This advantage of HYPER-OBA can be used for a longer fuel cycle. If the radial power distributions are the same at BOC for HYPER-OBA and the reference core, the peak power of the reference core would reach the criterion earlier than in HYPER-OBA. Based on the current results, it is conjectured that the fuel cycle length of HYPER-OBA would be at least a month longer than that of the reference design. Previously, we have seen that the initial source neutron multiplication of HYPER-OBA is smaller that that of the reference. This is partly because of the lower power density of the inner zone in HYPER-OBA, as shown in Figures 5 and 7. If the inner zone power were increased in HYPER-OBA, the initial multiplication of source neutrons would also increase.

In Figure 8, the depletion behaviours of $^{10}B$ in HYPER-HBA and HYPER-OBA are given. In HYPER-HBA, $^{10}B$ burns on the average at a rate of 2.22%/month and $^{10}B$ depletion rate of HYPER-OBA is 2.11%/month. HYPER-OBA has a slower depletion rate of $^{10}B$ since the burnable absorbers are loaded in relatively low-flux region, i.e. middle and outer zones. Assuming a 3-batch fuel management in an equilibrium cycle, it is expected that only about 50% of $^{10}B$ would burn out in the HYPER-OBA design. Therefore, the residual negative reactivity of $^{10}B$ is large in HYPER-OBA. However, as stated previously, the advantages of the HYPER-OBA design such as smaller proton beam current and longer cycle length would compensate for the negative impacts of $^{10}B$.

Figure 3. **Multiplication of spallation neutrons over a 180-day depletion in the HYPER cores**

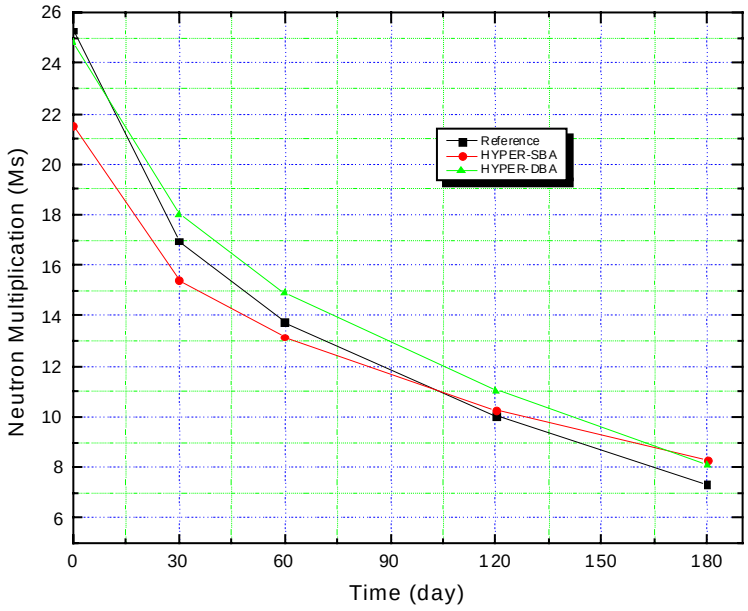

Figure 4. **Required proton beam currents for the reference and poisoned cores**

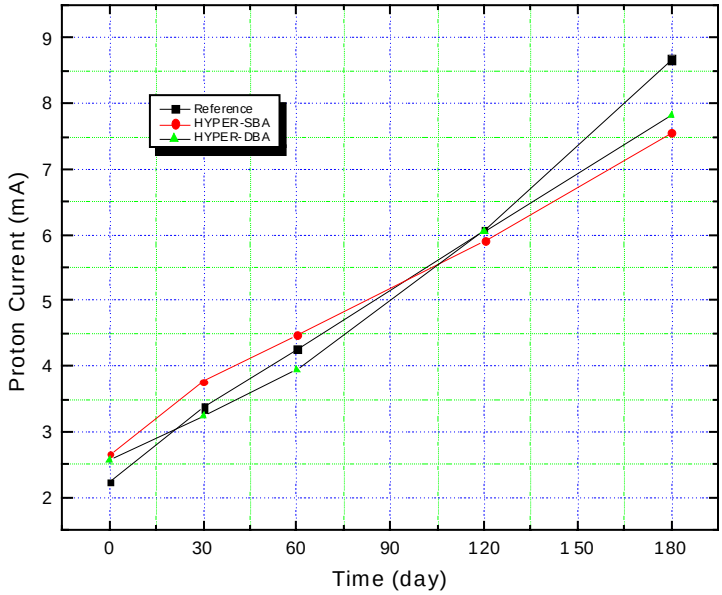


Figure 5. **Normalised radial power distributions of the reference HYPER core**

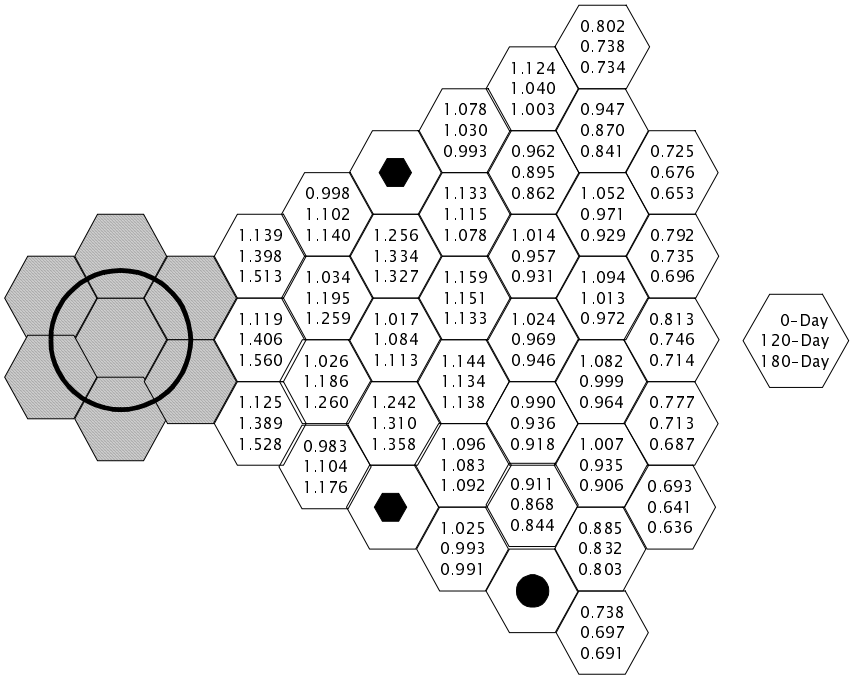

Figure 6. **Normalised radial power distributions in HYPER-HBA**

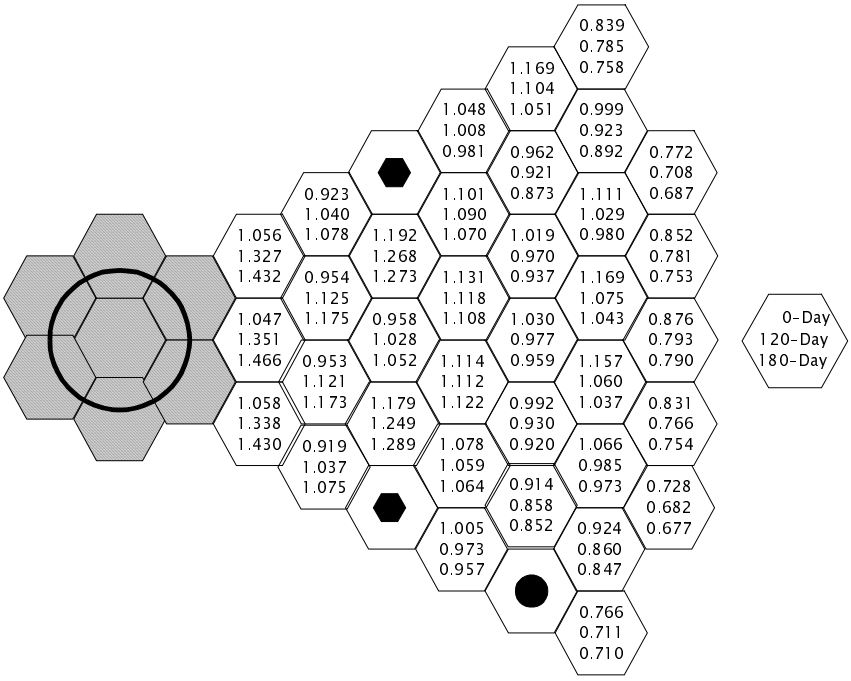


Figure 7. **Normalised radial power distributions in HYPER-OBA**

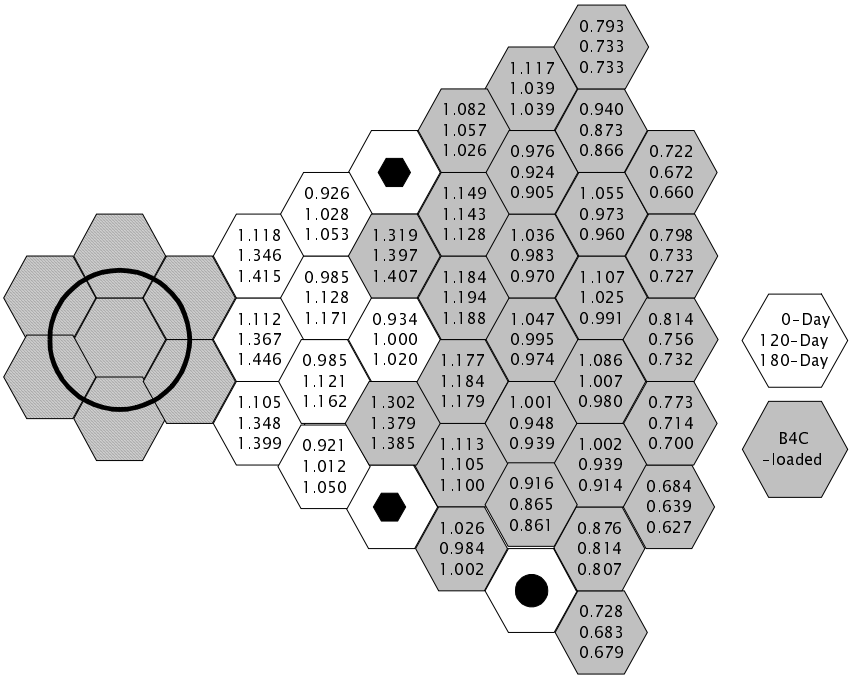

Figure 8. **$^{10}$B depletion in HYPER-HBA and HYPER-OBA**

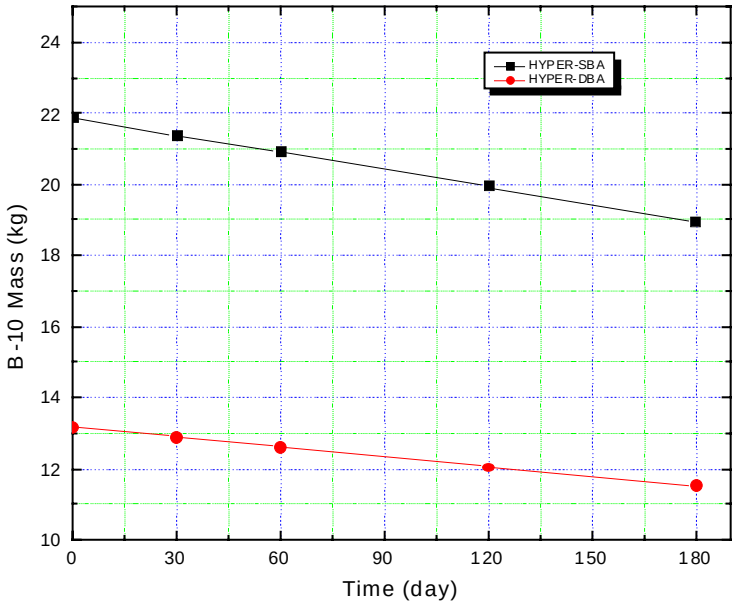


## 4. Conclusions

A homogeneous application of the $B_4C$ burnable absorber can be effectively used in reducing the burn-up reactivity swing. However, it is not favourable in terms of source neutron multiplication, since a significant fraction of spallation neutrons are parasitically absorbed by $B_4C$ before they are multiplied. In sub-critical reactor, absorbing materials should not be placed in the neighbourhood of the target zone.

Loading of $^{10}$B burnable absorbers in the outer zones is required in order to minimise the parasitic neutron absorption by $^{10}$B. In this application of $^{10}$B burnable absorber, the integrated and peak proton beam powers are lower than those of the reference design. In addition, this kind use of $^{10}$B can considerably mitigate the slanting phenomenon of the radial power distribution, which is a critical problem in TRU-loaded sub-critical reactors. Consequently, outer zone loading of $B_4C$ can lead to a longer cycle length, compared with the unpoisoned reference core.

Finally, it is concluded that $^{10}$B has a relatively high potential as a burnable absorbing material for fast sub-critical reactors and introduction of a burnable absorber would open a new research field to optimise the core design of ADS.

## REFERENCES


[1] W.S. Part *et al.*, *HYPER (Hybrid Power Extraction Reactor): A System for Clean Nuclear Energy*, Nuclear Engineering and Design, 199, p. 155, 2000.

[2] A. Jonsson, *Comparison of Economic Performance of Burnable Absorbers for 17 × 17 Fuel*, Proceedings of ANS Topical Meeting, March 1999.

[3] N. Stone *et al.*, *A Dual Spectrum Core for the ATW-Preliminary Feasibility Study*, PHYSOR 2000.

[4] P. Hejzlar *et al.*, *Conceptual Reactor Physics Design of a Lead-bismuth-cooled Critical Actinide Burner*, MIT-ANP-TR-069, 2000.

[5] H.J. Shim *et al.*, *Monte Carlo Depletion Analysis of a PWR with the MCNAP*, M&C 99 Int. Conf. on Mathematics and Computation, reactor physics and Environmental Analysis in Nuclear Applications, Sep. 1999, Madrid, Spain, Vol. 2, 1026-1035, 1999.

[6] W.S. Park *et al.*, *Fission Product Target Design for HYPER System*, to be presented at the 6th Information Exchange Meeting on Actinide and Fission Product Partitioning and Transmutation, Madrid, Spain, 11-13 Dec. 2000, OECD/NEA (Nuclear Energy Agency), Paris, France, 2001.

[7] Y.H. Kim, W.S. Park, and T.Y. Song, *Source Neutron Multiplication in Sub-critical Reactors*, to be presented at the IAEA Technical Committee Meeting on ADS to be held at Argonne, 2000.